UNIVERSTIY OF CALIFORNIA SAN DIEGO

Fracture Mechanics of Polymers and Polymer Composites

A dissertation submitted in partial satisfaction of the requirements for the degree Doctor of Philosophy

in

Engineering Sciences (Mechanical Engineering)

by

Zhaoqiang Song

Committee in charge:

Professor Shengqiang Cai, Chair
Professor Nicholas S. Boechler
Professor Veronica Eliasson
Professor Michael Frazier
Professor Xanthippi Markenscoff
Professor Kesong Yang

2021

The Dissertation of Zhaoqiang Song is approved, and it is acceptable in quality and form for publication on microfilm and electronically.

University of California, San Diego

2021

Table of Contents

List of Figures

List of Tables

Acknowledgements

I get plenty of help and support from many people, and I would like to express my gratitude to all of them.

First, I would like to express my deepest appreciation to Prof. Shengqiang Cai for his professional, excellent and considerate mentoring during my Ph.D. study. His extraordinary insight, deep understanding and great passion has largely expanded and deepened my understanding of mechanics. With those inspirational meetings and discussions, I've learned how to propose valuable scientific problems and find reasonable solutions. I can't wait to explore further in the field of mechanics.

Second, I would like to thank the other committee members my dissertation: Prof. Nicholas S. Boechler, Prof. Veronica Eliasson, Prof. Michael Frazier, Prof. Xanthippi Markenscoff and Prof. Kesong Yang for their invaluable suggestions, comments and kind assistances to my research projects.

I am very grateful to my previous and current group members. Thank you for helping on my researches and creating excellent academic atmosphere. They are Dr. Zhijian Wang, Dr. Chihyung Ahn, Dr. Xudong Liang, Dr. Somaye Jafari, Dr. Yue Zheng, Dr. Qiguang He, Yang Wang, Zijun Wang, Gaoweiang Dong, Chenghai Li, Raja Annapooranan, Nada F. Qari, Wei Fan.

Finally, I would like to give my gratitude to my parents, my wife and my friends for taking good care of me and giving me all the unconditional love and understanding.

Chapter 2, in full, is a reprint of the material as it appears in "Mechanics of vitrimer with hybrid networks", *Mechanics of Materials* 153 (2021), by Zhaoqiang Song, Zhijian Wang, and Shengqiang Cai. The dissertation author was the primary investigator and first author of this paper.

Chapter 3, in full, is currently being under review, "Force-dependent bond dissociation explains the rate-dependent fracture of vitrimers", by Zhaoqiang Song, Tong Shen, Franck Vernerey and Shengqiang Cai. The dissertation author was the primary investigator and first author of this paper.

Chapter 4, in full, is currently being under review, "Non-steady fracture of transient networks: the case of vitrimer", by Tong Shen, Zhaoqiang Song, Shengqiang Cai and Franck Vernerey. The dissertation author was the primary investigator and co-first author of this paper.

Chapter 5, in full, is a reprint of the material as it appears in "Fracture modes and hybrid toughening mechanisms in oscillated/twisted plywood structure", *Acta biomaterialia* 91, 284-293 (2019), by Zhaoqiang Song, Yong Ni, and Shengqiang Cai. The dissertation author was the primary investigator and first author of this paper.

Vita

2012	Bachelor of Science, University of Science and Technology of China
2015	Master of Engineering, University of Science and Technology of China
2021	Doctor of Philosophy, University of California San Diego

Publications

1. **Song, Z**., & Cai, S.* (2021). Cavitation dynamics in Vitrimer. *Acta Mechanica Sinica,* 1.

2. **Song, Z.**, Wang, Z., & Cai, S.*(2021). Mechanics of vitrimer with hybrid networks. *Mechanics of Materials*, 103687.

3. Zhou, H.#, **Song, Z.**#, & Cai, S.* (2020). Toughening of poly (lactide acid) with low crystallinity through biaxial poststretching. *Journal of Polymer Science*. 58 (24), 3488-3495.

4. He, Q., Wang, Z., Wang, Y., **Song, Z.**, & Cai, S.* (2020). Recyclable and self-repairable fluid-driven liquid crystal elastomer actuator. *ACS Applied Materials & Interfaces*, *12*(31), 35464-35474.

5. Wu, K., **Song, Z.,** Zhang, S., Ni*, Y., Cai, S., Gong, X., ... & Yu, S. H. (2020). Discontinuous fibrous Bouligand architecture enabling formidable fracture resistance with crack orientation insensitivity. *Proceedings of the National Academy of Sciences of the United States of America*, *117*(27), 15465-15472.

6. **Song, Z.**, Liang, X., Li, K. *, & Cai, S. *(2020). Surface Mechanics of a Stretched Elastomer Layer Bonded on a Rigid Substrate. *International Journal of Solids and Structures*. 200, 1-12.

7. Wang, P., Berry, D. B., **Song, Z.,** Kiratitanaporn, W., Schimelman, J., Moran, A., ... & Chen, S.* (2020). 3D Printing of a Biocompatible Double Network Elastomer with Digital Control of Mechanical Properties. *Advanced Functional Materials*, *30*(14), 1910391.

8. **Song, Z**., Ni, Y., & Cai, S.* (2019). Fracture modes and hybrid toughening mechanisms in oscillated/twisted plywood structure. *Acta biomaterialia*, *91*, 284-293.

9. Lu, Z.*, Cao, J., **Song, Z**., Li, D., & Lu, B.* (2019). Research progress of ceramic matrix composite parts based on additive manufacturing technology. *Virtual and Physical Prototyping*, *14*(4), 333-348. (Review paper)

10. He, Q., Wang, Z., **Song, Z**., & Cai, S.* (2019). Bioinspired design of vascular artificial muscle. *Advanced Materials Technologies*, 4(1), 1800244.

11. **Song, Z.**#, Shen, T.#, Vernerey. F.J. *, & Cai, S.* Force-dependent bond dissociation explains the rate-dependent fracture of vitrimers. *Under review*

12. Shen, T.#, **Song, Z.**#, Cai, S.*, & Vernerey. F.J. * Non-steady fracture of transient networks: the case of vitrimer. *Under review*

Abstract of the Dissertation

Fracture Mechanics of Polymers and Polymer Composites

by

Zhaoqiang Song

Doctor of Philosophy in Engineering Sciences (Mechanical Engineering)

University of California San Diego, 2021

Professor Shengqiang Cai, Chair

Vitrimers have recently emerged as a class of polymers combining great processability, self-healing capability and high-temperature mechanical properties. Most of those salient features of vitrimers originate from the existence of dynamic covalent bonds in the polymer network. Although intensive research has been conducted for understanding the constitutive properties of these new materials, their fracture behaviors have been largely unexplored. Moreover, improving the creep resistance and fracture toughness of vitrimers are critical for the commercial applications, which need to be addressed.

In this dissertation, we first experimentally show that, if the network with only regular covalent bonds and the network with dynamic covalent bonds are immiscible with each other, hybrid network can be synthesized with a low molar ratio of dynamic covalent bonds (less than 20 mol%), which still maintains its reprocessing and self-healing capabilities. Our discoveries will enable much greater tunability of the thermo-mechanical properties of vitrimers such as stress relaxation, creep resistance and fracture toughness, which can be important in many of their applications. Additionally, we investigate the rate-dependent fracture of vitrimers, and we, for the first time, obtain the intrinsic fracture energy and bulk dissipation of vitrimers during crack extension. Then, we find that the transient nature of a vitrimer network yields peculiar fracture characteristics that cannot be understood from existing fracture theories. Crack propagation is a non-equilibrium process whose velocity depends on the interplay between external load, bond dynamics and network damage. To explain the transient life of a crack in the vitrimer, we extend the linear elastic fracture theory to a dynamic model that predicts the time-dependent evolution of a crack during loading. Finally, we propose that a combination of crack tilting and crack bridging determines the effective fracture toughness of the fiber-reinforced composite with the plywood structure. Based on our quantitative analysis, it is found that the effective fracture toughness of the composite can be maximized for a certain pitch angle of the oscillated/twisted plywood structure, which agrees well with experiments.

Chapter 1 Introduction

1.1 Background

While thermoplastics exhibit high commercial values for distinct advantages of processability and recyclability over thermosets, other applications such as coatings, implanted materials, additive manufacturing, and adhesives require covalently crosslinked networks, i.e., thermosets because of increased stiffness, on demand formation, and permanent network architecture that leads to chemical and solvent resistance, creep resistance, and thermal stability [1]. Despite of its benefits, the permanent network also prevents more pervasive use of thermosets because of the intractable product which prevents self-healing, recycling, reprocessing, and postpolymerization manipulation. Therefore, there is a gap between the promising advantages of thermosets and the processability of thermoplastics. Recently, a new class of polymers called "vitrimers" which are composed of covalent adaptable networks (CANs) bridge this gap while enabling new features such as wider control over the stimuli-responsive dynamic properties [2-4]. The mechanical properties, especially the fracture property, can be the essentials for the application of the vitrimers [5, 6].

Vitrimers behaves like viscoelastic fluid if the bond exchanging reactions are activated. From a theoretical aspect, the key to predict the fracture of viscoelastic fluid lies in an accurate

calculation of the energy release rate G, defined as the decrease of total potential energy per increase in fracture surface area. The onset of crack propagation is set when G is greater than a critical value defined as the intrinsic fracture toughness G_0. Due to the thermally activated nature of bond dynamics, G dependents on both the rate of external load and the rate of crack propagation [7]. Previous theoretical efforts on the viscoelastic fracture, including the initial work of Williams [8], Knauss [9, 10] and Schapery [11, 12] and more recently de Gennes [13], Hui [14] Persson [15] and Nguyen [16], have mostly focused on the mode I steady-state fracture. At the steady state, G becomes a constant and has been successfully calculated by extracting the bulk viscous dissipation from external work. While these theories have been successful for linear viscoelastic materials (i.e., the relaxation rate does not depend on the load), their accuracy may fall short for transient networks, where several systems have shown a strong non-linear viscoelasticity (including the vitrimer). In this situation, the steady propagation is difficult to obtain since G becomes nonconstant during propagation. Since a non-linear viscoelastic material model is not available until the very recent work of Guo et al., [17], a generally valid measurement technique accompanied with calculation for the rate-dependent energy release rate of transient networks is not yet available.

The limitation of most polymers (including vitrimers) for the applications on the engineering structures is the low stiffness, strength and toughness, compared with the metals and alloys. Thanks to the unique microstructures, a lot of structural biomaterials have extraordinary

mechanical properties, i.e., a combination of the high strength and toughness. For example, the oysters and abalones develop a hard shell to protect themselves from their predators. Nacreous materials in such hard shell achieve outstanding mechanical properties [18, 19], including high stiffness, strength and toughness by the regular arrangement of their microstructures called 'brick-and-mortar' structure [20-23]. Mantis shrimps as predators use their dactyl clubs as weapons to break the shell of oysters and abalones in a high-speed impact [24]. The dactyl clubs should have excellent mechanical properties [25, 26] in order to smash the hard shells of the prey. The high fracture toughness of dactyl clubs is attributed to the unique microstructure, called Bouligand structure [25, 27-30].

1.2 Vitrimer overview

Vitrimer network with dynamic covalent bonds has emerged, which combines the advantages of both thermoplastics and thermosets. It has been shown that vitrimer exhibits excellent high-temperature properties, solvent resistance, processability, self-healing capability and recyclability [31, 32]. Different from regular covalent bonds, dynamic covalent bonds possess dormant ability to be activated by one or more forms of stimuli. Upon application of a stimulus, the covalent adaptable network (CAN) responds by transforming to a state of temporal plasticity. Vitrimers are widely studied as reversible CANs. They are a class of thermally activated associative CANs that exhibit Arrhenius-like dependence on viscosity and are characterized by a specific, chemistry-dependent, "topology freezing temperature" (T_v). Vitrimers have steady state

chemical composition and network connection, i.e., crosslink density. Upon the thermal stimulus, vitrimers exhibit the solid-to-fluid transition. The stimuli-responsive solid-to-fluid transition of vitrimers provide the opportunity for additive manufacturing. The understanding of fracture of vitrimers is important for such applications. The additive manufacturing of vitrimers is highly dependent on their fracture properties, for instant, the limitations of printing speeds and temperatures of vitrimers without fracturing the printed fibrils rely on the fracture behavior of vitrimers. However, the understanding of the fracture of vitrimers is still lacking.

1.3 Dissertation structure

The main objective of my dissertation is to understand fracture behaviors of vitrimers and the biological polymer composites. To achieve this goal, we synthesis the vitrimers and vitirmer composites, and characterize their mechanical properties. For biological polymer composites, we propose the hybrid toughening mechanisms to explain their strong and tough performances. This dissertation is organized as follows:

Chapter 1 introduces the background of the fracture of viscoelastic polymers and composites, and the overview of vitrimer. Chapter 2 describes the synthesis and characterizations of vitrimers with the hybrid networks. The vitrimers with the hybrid networks can be synthesized with a low molar ratio of dynamic covalent bonds (less than 20 mol%), which still maintains its reprocessing and self-healing capabilities. In Chapter 3, we investigate the rate-dependent fracture of vitrimers, and we, for the first time, obtain the intrinsic fracture energy and bulk dissipation of

vitrimers during crack extension. In Chapter 4, we find that the transient nature of a vitrimer network yields peculiar fracture characteristics that cannot be understood from existing fracture theories. Crack propagation is a non-equilibrium process whose velocity depends on the interplay between external load, bond dynamics and network damage. To explain the transient life of a crack in the vitrimer, we extend the linear elastic fracture theory to a dynamic model that predicts the time-dependent evolution of a crack during loading. In Chapter 5, we propose that a combination of crack tilting and crack bridging determines the effective fracture toughness of the fiber-reinforced composite with the plywood structure. Based on our quantitative analysis, it is found that the effective fracture toughness of the composite can be maximized for a certain pitch angle of the oscillated/twisted plywood structure, which agrees well with experiments. In Chapter 6, we summary the dissertation and provide outlooks for the future works.

Chapter 2 Mechanics of Vitrimer with Hybrid Networks.

2.1 Introduction

Compared to thermoplastic polymers, thermosets have better performance at high temperature and higher resistance to solvent penetration; however, thermosets are much less processable and most of them are not recyclable [33]. Recently, vitrimer network with dynamic covalent bonds has emerged, which combines the advantages of both thermoplastics and thermosets. It has been shown that vitrimer exhibits excellent high-temperature properties, solvent resistance, processability, self-healing capability and recyclability [32, 34].

Different from regular covalent bonds, dynamic covalent bonds can undergo bond exchanging reaction in certain conditions. Dynamic exchanging reactions are often realized through either associative mechanism or dissociative mechanism [2, 3, 35-37]. A crosslinked polymer network with dissociative dynamic covalent bonds shows an abrupt degradation of its mechanical properties when reaction is activated, whereas a polymer network with associative dynamic covalent bonds, also named as vitrimers, can maintain its crosslinking density unchanged during the exchanging reaction [38]. Consequently, most mechanical and chemical properties of vitrimers degrade slowly with the increase of temperature, and they can be easily reshaped and recycled at elevated temperature through dynamic exchanging reactions, similar to most thermoplastics. Examples of the dynamic exchanging reactions include transesterification [31, 38],

imine exchange [39], transcarbamoylation [40, 41], and silyl-ether exchange reaction [42], which have all been introduced into synthesizing vitrimer networks.

Mechanical properties of vitrimers highly depend on the type of dynamic covalent bonds. The viscoelastic properties of vitrimers or so called transient network polymers have been intensively studied in recent years [43-46]. Quite a few of rheological models [46-50] have also been proposed to predict the viscoelastic behaviors of these materials.

To further tailor the mechanical properties, polymers with hybrid networks of dynamic and regular covalent bonds have been synthesized [51-54]. It has been shown that the presence of monomers only with regular covalent bonds in vitrimers increases their resistance to creep [53, 54]. However, in order to maintain the great reprocessability of vitrimers with hybrid networks, the molar concentration of dynamic covalent bonds has to be high enough [53].

In previous experiments, the monomers only containing regular covalent bonds and the monomers with dynamic covalent bonds are often miscible with each other and the two types of monomers are mixed homogenously in a crosslinked polymer network [53, 54]. Based on Flory-Stockmayer theory [55, 56], it can be estimated that to maintain the reprocessability of the polymer network, the molar ratio between the monomers containing dynamic covalent bonds and the monomers with only regular covalent bonds has to satisfy the following inequality:

$$\frac{k}{k+1} < \frac{1}{f-1}, \tag{2.1}$$

where k is the molar ratio of bifunctional monomers with only regular covalent bonds to the bifunctional monomers with dynamic covalent bonds, and f is the functionality of crosslinkers. For instance, if we use tetrafunctional crosslinkers (f=4), vitrimers with hybrid networks would be fully reprocessable if the bifunctional monomers with dynamic covalent bonds is higher than 66.7 mol%. The above theoretical prediction has shown to be consistent with experiments [53].

In the current study, we mix two immiscible monomers with crosslinkers to synthesize a hybrid polymer network. One of the monomers contains dynamic covalent bonds while the other is only composed of regular covalent bonds as shown in Figure 2.1. We find that with as little as less than 20 mol% of monomers with dynamic covalent bonds, the hybrid polymer network behaves like a vitrimer. The hybrid polymer network can be easily reprocessed and self-healed, and its temperature-dependent rheological properties are Arrhenius-like. The minimal concentration of monomers with dynamic covalent bonds (less than 20 mol%) is significantly less than the value predicted by Flory-Stockmayer theory as shown in Eq. (2.1) (67 mol%). To explain the experiment results, we hypothesize that, due to the high contrast of the viscosity of the two monomers in liquid state during the mixing, after polymerization, the polymer chains containing dynamic covalent bonds form continuous phases in the network even when their concentration is less than 20 mol%. Based on the hypothesis, we further develop a theoretical model to predict stress relaxation and creep of the vitrimers with hybrid networks at different temperatures and with different molar ratios between the two monomers. Without a single fitting parameter, the

theoretical predictions agree well with experimental measurements. We further show that the fracture toughness of the polymer network reaches a maximum for a certain molar ratio of the two monomers.

2.2 Results and discussion

2.2.1 Synthesis of vitrimer with hybrid networks

EPS25 (epoxy equivalent = 777 g/equiv) was kindly provided by Akzo Nobel Chemicals; DER732 (Dow Chemicals, epoxy equivalent = 303 g/equiv, Sigma Aldrich), pentaerythritol tetrakis(3-mercaptopropionate) (PETMP, Sigma Aldrich), 4-(dimethylamino)pyridine (DMAP, Sigma Aldrich), and Dithiothreitol (DTT, Sigma Aldrich) were used as received.

We synthesized hybrid network with two monomers, EPS25 and DER732, by following the previous work [57]. For the synthesis of vitrimer containing 20 mol% of EPS25 (the molar ratio of EPS25 in the DER732 and EPS25 mixture), we added 8 mmol DER732 and 5 mmol PETMP into 2 mmol EPS25, and manually stirred the mixture until homogeneous. Then, we added 1 wt% of DMAP as catalyst into the mixture. We stirred the mixture for 10 more minutes and degassed under vacuum. After that, we poured the mixture into a glass mold and heated at 60°C for 2 hours. Finally, we obtained the vitrimer with hybrid networks. The epoxy group in EPS25 and DER732 shown in Figure 2.1a reacted with the thiol group in PETMP under the catalyst DMAP, as shown in Figure 2.1b. This thiol-epoxy reaction is often categorized as a click reaction [58]. After polymerization, the hybrid network was formed as shown in Figure 2.1c. We

synthesized the samples with molar concentrations of 0 mol%, 5 mol%, 10 mol%, 50 mol% and 100 mol% of EPS25 through the same procedure described above. We calculated the volumetric fraction of EPS25 for each sample based on its molar ratio and the density of EPS25 (1.2 g/cm3) and that of DER732 (1.06 g/cm3).

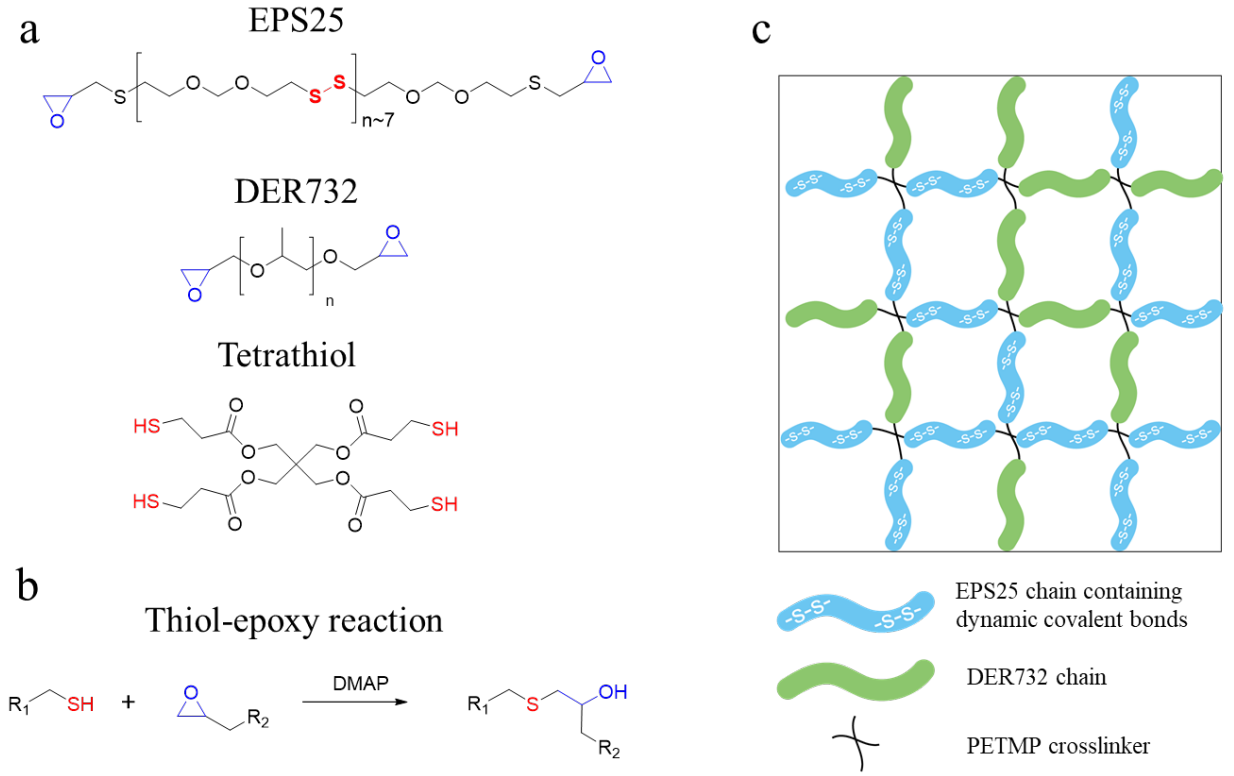

Figure 2.1: Chemical component and synthesis of vitrimer with hybrid networks. a Chemical structure of the two monomers used in the study: EPS25 and DER732, and the crosslinker: tetrathiol. EPS25 contains disulfide bonds which are dynamic covalent bonds while DER732 only has regular covalent bonds. **b** Thiol-epoxy reaction for crosslinking (with DMAP (4-Dimethylaminopyridine) as the catalyst). **c** Schematic of the polymer network with mixed monomers.

2.2.2 Dissolution of vitrimers with hybrid networks

We selected vitrimers containing 20 mol% of EPS25 and vitrimers containing 5 mol% of EPS25 to conduct dissolution tests. We immersed the samples (typically, with an initial mass, 20

mg) in methylene chloride (typically, 2 mL) at room temperature. After 24 hours, we rinsed the samples with methylene chloride three times. We put the samples into oven at 60℃ for 6 hours, and weighted them.

We also immersed the samples in 0.1M DTT solution with the solvent of methylene chloride at room temperature. After 24 hours, if the sample was not completely dissolved, we immersed the sample in methylene chloride for 5 mins and then rinsed it with methylene chloride for three times. We finally dried and weighted the sample if it still existed.

2.2.3 Mechanical characterization

We prepared the samples of the vitrimer with hybrid networks with different molar ratios of EPS25 (molar ratios of EPS25 in the DER732 and EPS25 mixture): 0 mol%, 5 mol%, 10 mol%, 20 mol%, 30 mol%, 50 mol% and 100 mol%. We conducted the stress relaxation and creep experiments using the dynamic mechanical analysis equipment RSA-G2 (TA instruments, New Castle). In the stress relaxation experiments, we applied a constant strain of 2% for pure DER732 samples and 5% for all other samples and measured the stress as a function of time. In the creep experiments, we applied a constant stress of 500 Pa onto all samples and measured the strain as a function of time. We performed each test three times.

We characterized the self-healing abilities of the vitrimers by measuring the strengths of the samples after self-healing. In the experiment, we introduced a precut into a sample by using a sharp blazer and then put the sample into an oven at 60℃ for different periods of time. The self-

healing time for 20 mol% EPS25 samples in the oven was set to be 1 hour, 3 hours, 6 hours, and 12 hours, and the time for 5 mol% EPS25 samples in the oven was 15 hours, 24 hours and 48 hours. We conducted the tensile tests of both pristine and self-healed specimens at nominal strain rate of 0.005/s at room temperature (23.5℃) by using Instron 5965 (Instron, Norwood).

To test the reprocessing capabilities of the hybrid network, we cut the sample into small pieces of submillimeter size. We then used heat press machine (Carver, Wabash) to compress the vitrimer pieces into a thin film. We conducted heat press experiment with 5 tons compression force (about 2 MPa pressure) at 70℃ for 4 hours. We measured the stress-strain curve of reprocessed sample at nominal strain rate of 0.005/s at room temperature by using Instron 5965 and compared it with the stress-strain curve of pristine sample.

We measured the fracture toughness of the samples at room temperature through pure shear test by using Instron 5965. We first cut the samples to a rectangular shape with the dimension 50 mm X 10 mm X 2 mm. We introduced a pre-crack into some of the samples with the length of 15 mm by using a sharp blazer. We glued the samples onto two rigid acrylate plates which were then clamped by the tensile grips of the machine. We set the nominal strain rate be 0.01/s. The stress-stretch curve of samples with and without pre-cracks were recorded. We also recorded the fracture process by using a digital camera (Cannon EOS 80D).

2.2.4 Stress relaxation and creep of the vitrimer with hybrid networks

Figure 2.2a shows the stress relaxation of the vitrimer with only EPS25 at several different temperatures (20℃, 40℃, 60℃ and 80℃). The stress relaxation of the vitrimer $\sigma(t)$ can be described by the simple form:

$$\frac{\sigma}{\sigma_0} = \exp\left(-\frac{t}{\tau}\right), \tag{2.2}$$

where σ_0 is the instantly applied stress and τ is the characteristic relaxation time. We further found that the dependence of the relaxation time on the temperature closely follows the Arrhenius law as

$$\tau = \frac{1}{k_0}\exp\left(\frac{E_a}{RT}\right), \tag{2.3}$$

which is shown in Figure 2.2(b). The universal gas constant *R* in Eq. (2.3) is 8.314 J/(K·mol); the pre-exponential factor is $k_0 = 2.17\times10^6\ \mathrm{s}^{-1}$ (according to collision theory, k_0 is the frequency of collisions in correct orientation) [44]; and the activation energy is $E_a = 45.44\ \mathrm{kJ/mol}$. It is noted that activation energy is comparable to the bond energy of disulfide bond (~51 kJ/mol) [59, 60], which is consistent with pervious experiments on vitrimer [61, 62]. The stress relaxation of EPS25 given by Eq. (2.2) indicates that its rheological behavior can be described by a simple Maxwell model for viscoelasticity [44].

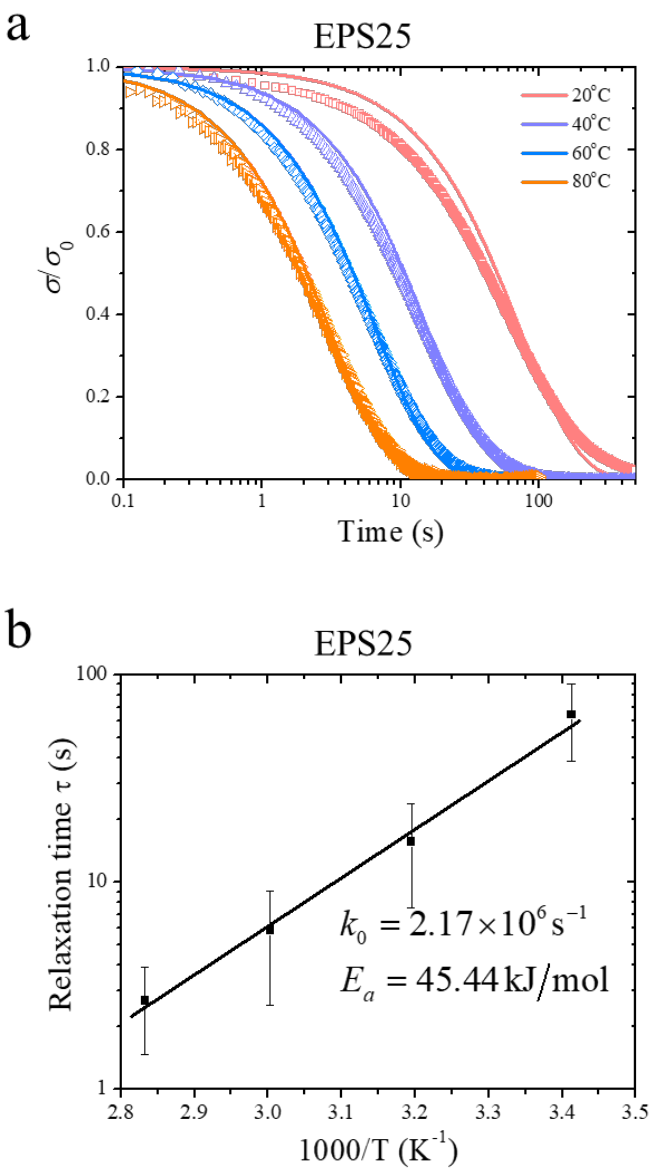

Figure 2.2: Stress relaxation of EPS25 vitrimer. a Stress relaxation of crosslinked EPS25 at different temperatures. **b** The dependence of the relaxation time on temperature.

As a comparison, for the same temperature range, DER732 network shows purely elastic response and little stress relaxation can be observed when the applied strain is fixed as a constant as shown in Figure 2.3.

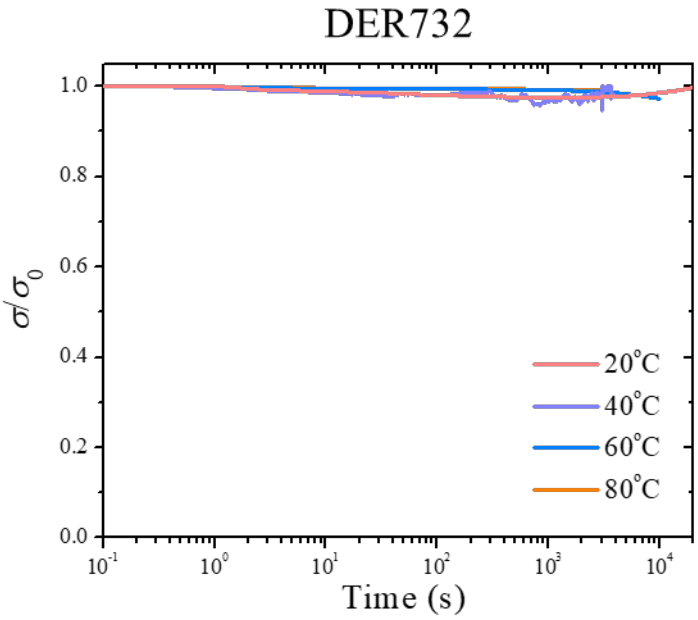

Figure 2.3: Stress relaxation of DER732 elastomer.

Figure 2.4 shows the stress relaxation of the vitrimer network with different molar ratios of EPS25 at different temperatures. For the vitrimers with 20 mol% EPS25, 30 mol% EPS25 and 50 mol% EPS25, the external stress finally relaxed to zero after certain periods of time. However, for the vitrimers with 5 mol% EPS25 and 10 mol% EPS25, their stress cannot relax to zero even after very long time. The stress relaxation of vitrimers with hybrid networks can be well fitted to a stretched exponential decay [63, 64]:

$$\frac{\sigma(t)}{\sigma_0} = \left(\frac{\sigma_{\text{inf}}}{\sigma_0}\right) + \left(1 - \frac{\sigma_{\text{inf}}}{\sigma_0}\right) \exp\left(-\left(\frac{t}{\tau_0}\right)^{\beta}\right), \tag{2.4}$$

where $\sigma(t)/\sigma_0$ is the normalized stress at time t, τ_0 is a characteristic time, β $(0 < \beta \leq 1)$ determines the shape of the stretched exponential decay and reflects the breadth of the relaxation time distribution, with $\beta = 1$ indicating a single relaxation time, and σ_{inf} is the stress in the

polymer when time approaches infinite. The vitrimers with more than 20 mol% EPS25 can fully relax the stress to zero after long enough time, which we refer as fluid-like behavior. For the vitrimers with 5 mol% EPS25 and 10 mol% EPS25, its stress cannot relax to zero even after long time, which we refer as solid-like behavior. Such definitions of solid-like and liquid-like behavior are consistent with most of previous works [65]. The characteristic relaxation time of a stretched exponential decay is defined as $\tau_R = \tau_0 \Gamma\left(1/\beta\right)/\beta$ [53], where Γ is gamma function. The fitting parameters for the measured stress relaxation curves in Figure 2.4 are summarized in Table 2.1. We can further calculate relaxation time of the vitrimers with 20 mol% EPS25, 30 mol% EPS25 and 50 mol% EPS25, τ_R, by fitting the stress relaxation curve at different temperatures using Eq. (2.4), as shown in Figure 2.5. The dependence of relaxation time τ_R on the temperature also follows Arrhenius law with the same activation energy E_a of pure EPS25 in Eq. (2.2).

In addition, fast stress relaxation can be found in the vitrimer with a high molar fraction of the EPS25 as shown in Figure 2.4. For example, the relaxation time of the vitrimer with 50 mol% EPS25 is about 4.1 s at 80℃, while the relaxation time of the vitrimer with 5 mol% EPS25 is about 103 s at 80℃ as shown in Figure 2.4a and Table 2.1. For a fixed temperature, the vitrimers with the low molar concentration of EPS25 (e.g. 5 mol% EPS25) always have a longer relaxation time.

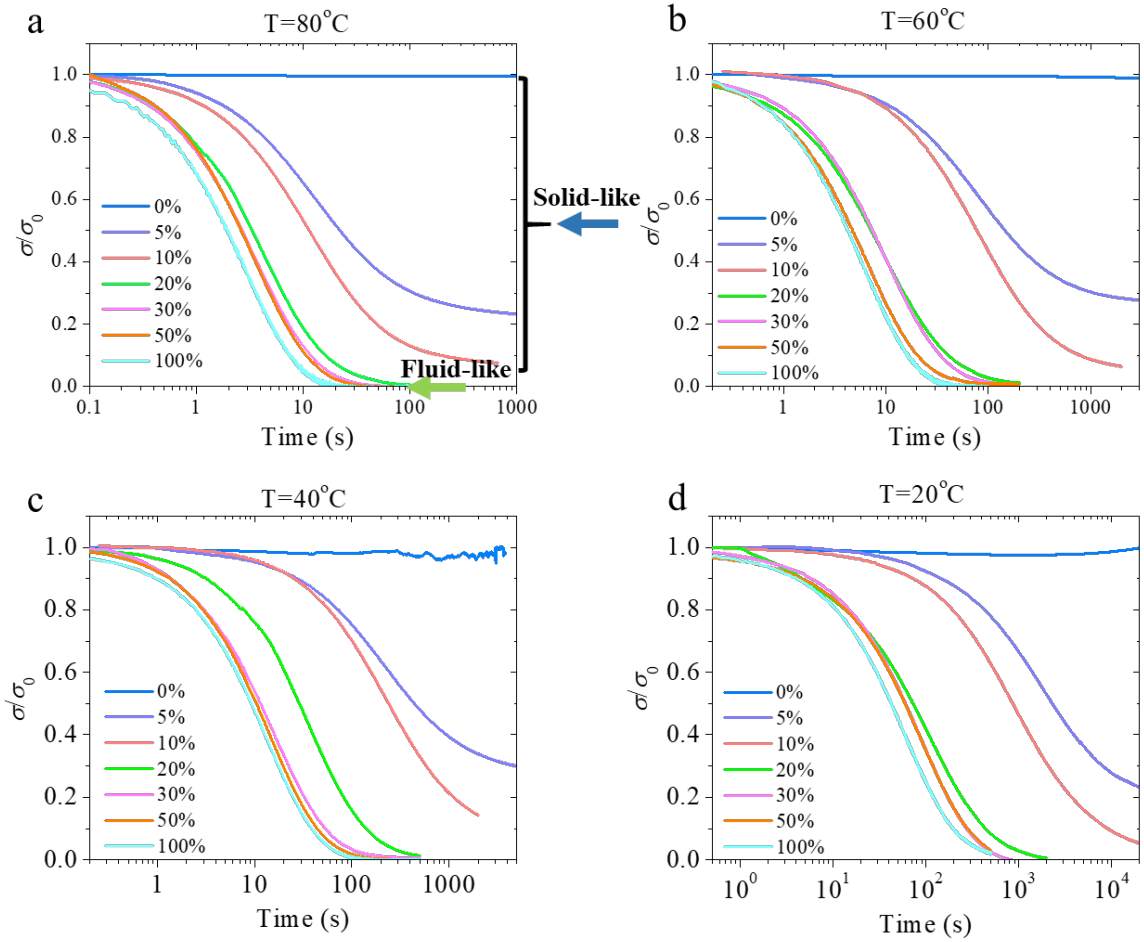

Figure 2.4: The stress relaxation of the vitrimer with different molar ratios of the two monomers (0 mol% EPS25, 5 mol% EPS25, 10 mol% EPS25, 20 mol% EPS25, 30 mol% EPS25, 50 mol% EPS25 and 100 mol% EPS25) at different temperatures. a 80℃, **b** 60℃, **c** 40℃ and **d** 20℃. When the molar ratio of EPS25 is higher than 20%, the stress in the polymer can relax to zero in a finite time, behaving like fluid. When the molar ratio of EPS25 is 0 mol%, 5 mol% and 10 mol%, the stress in the polymer cannot relax to zero even after long time, behaving like a solid.

Table 2.1: Parameters for fitting the measured stress relaxation curves (Figure 2.4) to the stretched exponential decay in Eq. (2.4).

Percentage of EPS25 (mol%)	$\sigma_{\inf}/\sigma_0$	τ_0 (s)	β	τ_R (s)	Adjusted R^2
T=80°C					
5	0.2474	80.94	0.6930	103.3	0.997
10	0.0694	62.29	0.6323	87.83	0.994
20	0.0144	5.203	0.8289	5.753	0.999
30	0.0048	4.194	0.8686	4.503	0.999
50	0.0020	3.949	0.9276	4.089	0.999
T=60°C					
5	0.2831	119.1	0.6432	164.7	0.996
10	0.0733	114.1	0.7033	143.8	0.996
20	0.01675	11.56	0.7271	14.13	0.998
30	0.0097	11.49	0.8124	12.88	0.999
50	0.0081	7.198	0.8423	7.876	0.999
T=40°C					
5	0.2919	342.6	0.5895	527.7	0.994
10	0.1410	296.4	0.7670	346.6	0.999
20	0.0185	44.35	0.8098	49.82	0.999
30	0.0082	18.04	0.7939	20.55	0.999
50	0.0022	16.15	0.8328	17.81	0.999
T=20°C					
5	0.2316	2206	0.6967	2805	0.999
10	0.0584	1369	0.6313	1934	0.997
20	0.0096	120.3	0.6753	157.8	0.999
30	0	95.88	0.8013	108.5	0.999
50	0.005	92.32	0.7909	105.5	0.999

Similar to pure EPS25, temperature also plays an important role in the rheology of vitrimers with hybrid networks. For instance, the average relaxation time of vitrimers with 20 mol% EPS25 is 5.65 s at 80°C, 12.88 s at 60°C, 47.82 s at 40°C, and 123.64 s at 20°C, as shown in Figure 2.5.

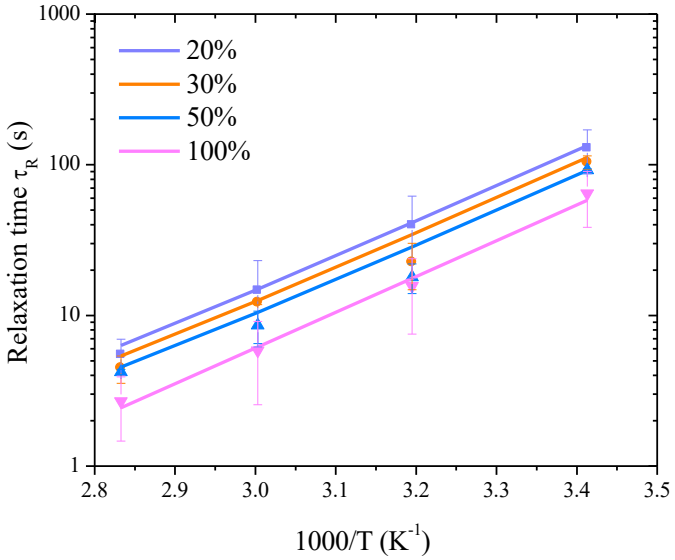

Figure 2.5: The relaxation time of the vitrimers with 20 mol% EPS25, 30 mol% EPS25, 50 mol% EPS25 and 100 mol% EPS25 as a function of temperature. The dots are experimental data, and solid lines are fitting results based on Arrhenius law (error bars represent the standard deviation).

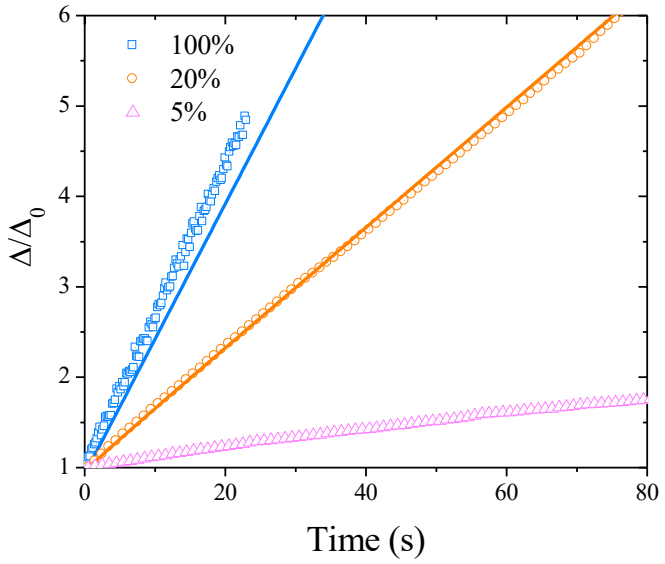

Figure 2.6: Creep of EPS25, the polymer network with 20 mol% EPS25 and the polymer with 5 mol% EPS25 at 40℃. The open dots are experimental data and the solid lines are theoretical predictions.

In addition to stress relaxation, we also measured the creep of pure EPS25, and the vitrimers with 20 mol% EPS25 and with 5 mol% EPS25 at 40℃, as shown in Figure 2.6. The presence of DER732 only containing regular covalent bonds can improve the creep resistance of the vitrimer. The improvement of creep resistance increases with the increase of the concentration of DER732.

2.2.5 Phase separation in the vitrimer with hybrid networks

As mentioned in the introduction, if the two monomers (EPS25 and DER732) were homogenously mixed with each other, based on Flory-Stockmayer theory [53], the vitrimer with hybrid networks could fully relax its stress only when the molar ratio of EPS25 which contains disulfide dynamic bonds is above 67 mol%. However, as shown in Figure 2.4, with as small as 20 mol% of EPS25, the polymer network with a fixed strain can relax its stress to zero after a certain period of time. It will be further shown that the polymer network can be fully reprocessed as well as self-healed with such low molar concentration of EPS25.

To explain the phenomena, we assume that in the hybrid polymer network, EPS25 and DER732 form two separated phases, and EPS25 is the continuous one and DER732 is dispersed as shown in Figure 2.7d. The underlying reason for the stable phase separation is that the viscosity of EPS25 (2.2 Pa·s) is significantly higher than that of DER732 (0.1 Pa·s). During the mixing, the highly viscous EPS25 does not break into small droplets (if its molar fraction is higher than 20%) and maintains its topological continuity, while the much less viscous DER732 breaks into small

droplets and embedded in the EPS25 matrix. Similar phenomenon has been reported in the experiments of blending two polymer melts [66]. Emulsion stabilized by high viscous liquid has also been widely known [67]. We have also shown in the experiments, the EPS25 and DER732 can maintain as two separated layers for more than several weeks if we do not mechanically mix them together as shown in Figure 2.8.

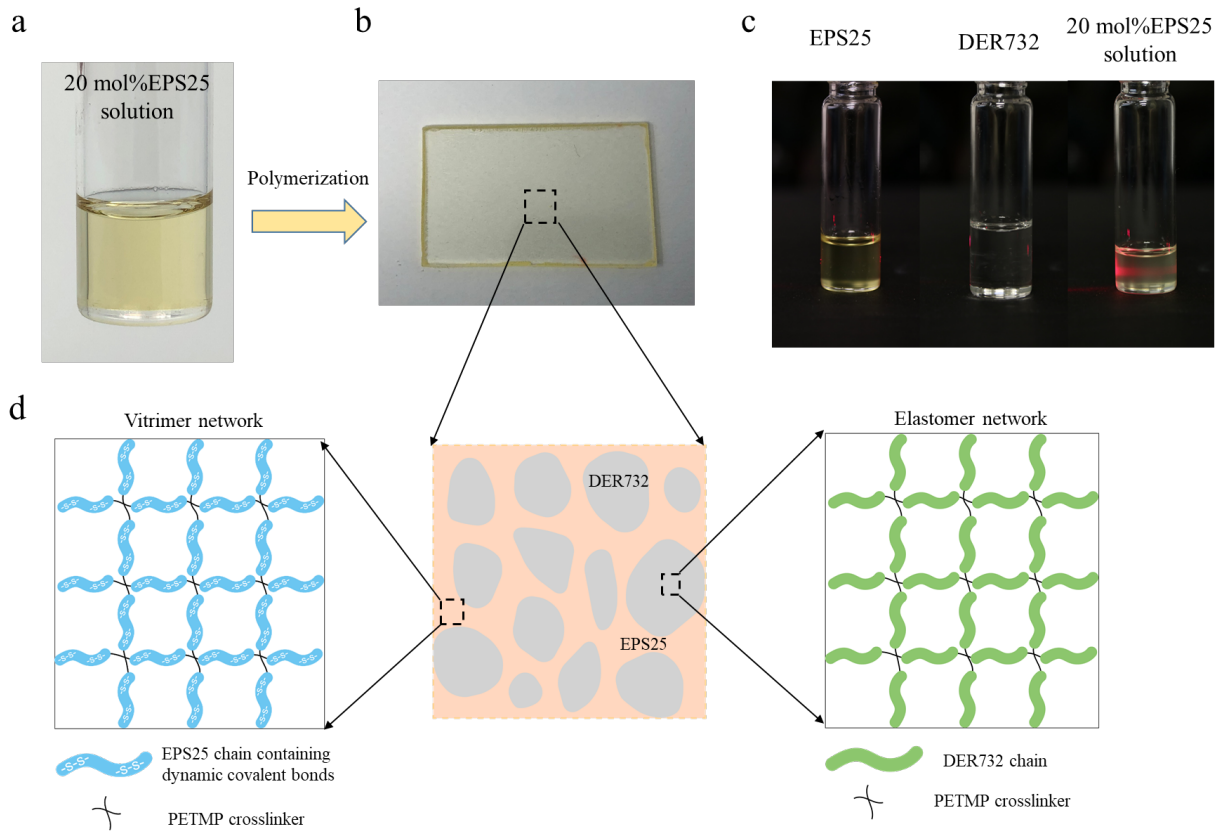

Figure 2.7: Phase separation in the vitrimer. a Liquid mixture of EPS25 and DER732. **b** Polymerized thin film of the liquid mixture. **c** Negligible light scattering in pure EPS25 and pure DER732 vs. strong light scattering in the mixture of EPS25 and DER732 (20 mol% EPS25 and 80 mol% DER732). **d** Schematics of the phase separation in the 20 mol% EPS25 polymer network.

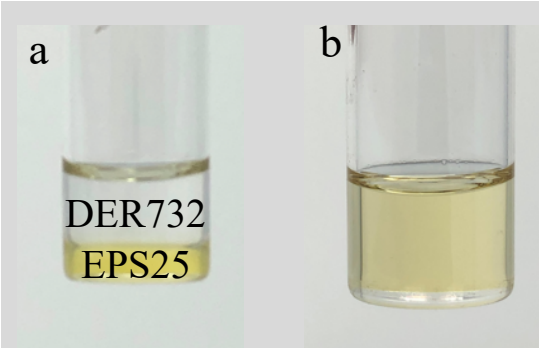

Figure 2.8: Aging effect on phase separation in the vitrimer. The liquid containing 20 mol% EPS25 and 80 mol% DER732 after resting for two weeks: **a** without mixing; **b** with mixing.

To testify the phase separation assumption, we conducted the light scattering experiments of pure EPS25 liquid, pure DER732 liquid and the mixture with 20 mol% EPS25 and 80 mol% DER732 after stirring 10 minutes. As shown in Figure 2.7c, strong light scattering was observed in the mixture, while negligible light scattering can be observed in pure EPS25 and pure DER732. Such light scattering often indicates the phase separation in the liquid.

Additionally, following the reference [51], we have also conducted the dissolution tests of the polymer network. It is known that disulfide bonds can be cleaved by DTT through reduction. We submerged the polymer with different volumetric fractions of EPS25 into 0.1M DTT solution with methylene chloride as the solvent. When the fraction of EPS25 was less than 5 mol%, after the polymer was submerged in the DTT solution, the sample became porous but still maintained its integrity, indicating EPS25 is embedded in the continuous DER732 matrix. The SEM image of a slightly etched surface of the sample containing 5mol% EPS25 is shown in Figure 2.9, where heterogenous etching can be clearly seen. However, as shown in Figure 2.10, the polymer with 20

mol% EPS25 could be completely dissolved in 0.1M DTT solution, indicating EPS25 forms a continuous phase in the hybrid network as sketched in Figure 2.7d.

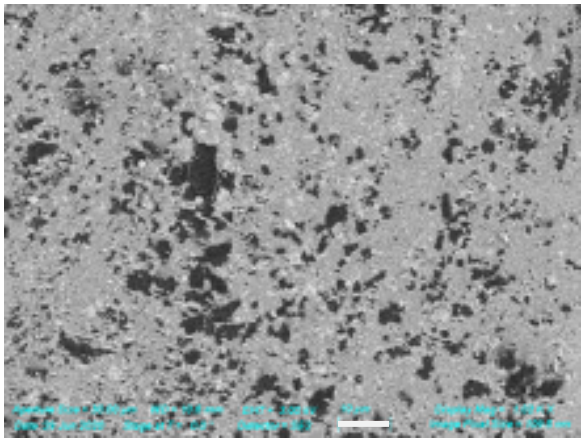

Figure 2.9: The scanning electronic microscopic image of 5 mol% EPS25 after etching. 5 mol% EPS25 vitrimer is etched for 5 min by 0.1M DTT solution (solvent: dichloromethane). The scale bar is 10 μm.

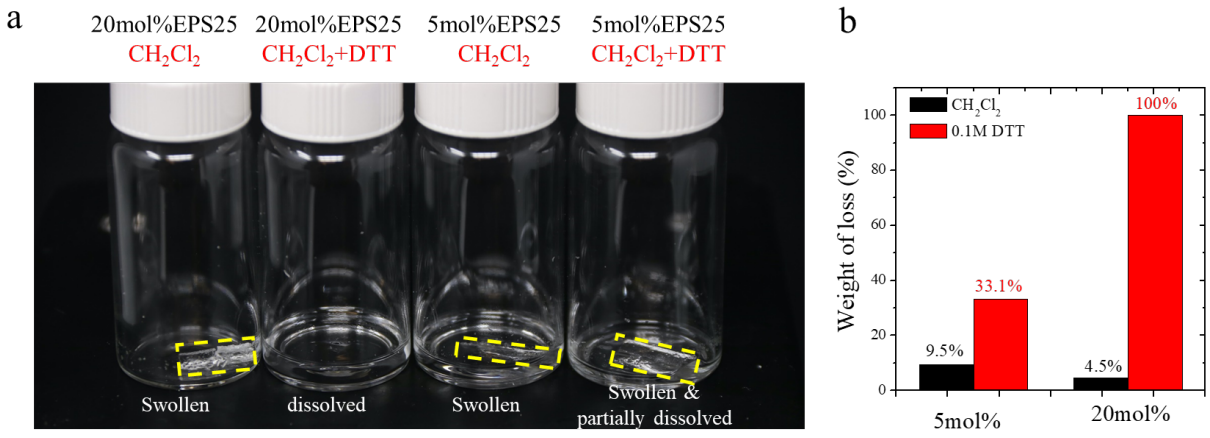

Figure 2.10: Dissolution of vitrimer with hybrid networks. a Polymer specimen was immersed in methylene chloride and 0.1M DTT methylene chloride solution. For the polymer with 20 mol% EPS25, the polymer could be completely dissolved in the DTT solution. For the polymer with 5 mol% EPS25, the polymer was only partially dissolved in the DTT solution. **b** The weight loss of the polymers after they were immersed in methylene chloride and the DTT solution for 24 hours.

In the following session, we will develop a quantitative rheological model for the vitrimer with hybrid networks and compare our predictions with the experimental measurements.

2.2.6 Rheological model for vitrimers with hybrid networks

Based on the previous understanding, in the model, we simplify the morphology of the phase separation in the vitrimer as shown in Figure 2.11a. We assume that when the molar concentration of EPS25 is more than 20 mol%, small DER732 cubes of equal size are embedded in EPS25 matrix homogenously.

As shown in Figure 2.11b, the ratio between the size of the cube (denoted by a) and the distance between each cube (denoted by b) can be simply determined by the volumetric fractions of the two phases as

$$\frac{a}{b} = \sqrt[3]{1-\phi_V}\,, \tag{2.5}$$

where ϕ_V is volumetric fraction of EPS25.

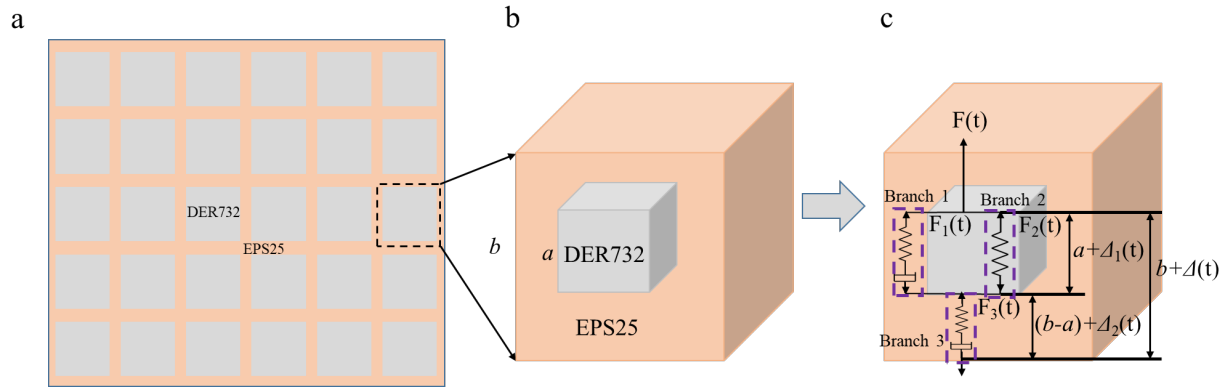

Figure 2.11: A simplified model for the vitrimer with more than 20 mol % of EPS25. a The schematic of the phase separation of the vitrimer with hybrid networks. **b** Representative volume element of the vitrimer. The size of DER732 cube is a, and the size of the representative volume element is b. **c** Spring-dashpot model of the vitrimer. DER732 is represented by a linear spring while the EPS25 is represented by a series connection of a spring and a dashpot.

In a representative volume element as shown in Figure 2.11(c), based on the force balance, we have the following relationship

$$F(t) = F_3(t) = F_1(t) + F_2(t), \tag{2.6}$$

where $F(t)$ is the force applied onto the element, $F_1(t)$ and $F_3(t)$ are the forces applied on the EPS25 (branch 1 and branch 3) and $F_2(t)$ is the force applied on DER732 (branch 2). Based on the geometry of the representative volume element as shown in Figure 2.11b-c, we can obtain that:

$$F_1(t) = \sigma_1(t)\left(b^2 - a^2\right), \tag{2.7}$$

$$F_2(t) = \sigma_2(t)a^2, \tag{2.8}$$

$$F_3(t) = \sigma_3(t)b^2, \tag{2.9}$$

in which $\sigma_1(t)$ and $\sigma_3(t)$ are the stresses applied on EPS25 of different branches (branch 1 and branch 3) in the representative volume element and $\sigma_2(t)$ is the stress applied on DER732 (branch 2).

As shown in section 2.2.4, the rheological behaviors of EPS25 can be represented by a series connection of a spring and a dashpot (Maxwell model), while DER732 behaves like a linear spring. Consequently, the entire vitrimer with hybrid networks can be represented by a combination of springs and dashpots as shown in Figure 2.11c.

The displacement of the representative volume element is

$$\Delta(t) = \Delta_1(t) + \Delta_3(t), \tag{2.10}$$

where $\Delta_1(t)$ is the displacement of branch 1 representing EPS25 and branch 2 representing DER732, and $\Delta_3(t)$ is the displacement of branch 3 representing EPS25 on the bottom of the representative volume element, as shown in Figure 2.11c. So, we have

$$\Delta_1(t) = \varepsilon_1(t)a, \tag{2.11}$$

$$\Delta_3(t) = \varepsilon_3(t)(b-a), \tag{2.12}$$

in which $\varepsilon_1(t)$ is the strain of the parallel connection of the EPS25 and DER732, $\varepsilon_3(t)$ is the strain of EPS25 on the bottom of the representative volume element (branch 3).

The relationship between the stress and strain for EPS25 (branch 1 and branch 3) can be given by:

$$\frac{d\sigma_i(t)}{dt} + \frac{\sigma_i(t)}{\tau} = E_{EPS}\frac{d\varepsilon_i(t)}{dt}, \tag{2.13}$$

where *i*=1,3, and E_{EPS} and τ are instantaneous modulus and relaxation time of pure EPS25, respectively. For DER732, the relation of stress and strain is simply,

$$\sigma_2(t) = E_{DER}\varepsilon_1(t), \tag{2.14}$$

where E_{DER} is the elastic modulus of pure DER732 elastomer.

The stress $\sigma(t)$ and strain $\varepsilon(t)$ in the representative volume element are defined by:

$$F(t) = \sigma(t)b^2, \tag{2.15}$$

$$\Delta(t) = \varepsilon(t)b. \tag{2.16}$$

Combining Eqs. (2.6-2.16), we can obtain the relationship between the applied stress and strain of representative volume element in Laplace space as [68]

$$\bar{\sigma} = \frac{1}{\dfrac{(\tau s+1)ab}{\left(E_{DER}a^2 + E_{EPS}b^2 - E_{EPS}a^2\right)\tau s + E_{DER}a^2} + \dfrac{(\tau s+1)(b-a)}{E_{EPS}\tau s b}}\bar{\varepsilon}, \tag{2.17}$$

where

$$\begin{aligned}\bar{\sigma} &= \int_0^\infty \sigma(t) e^{-st} dt, \\ \bar{\varepsilon} &= \int_0^\infty \varepsilon(t) e^{-st} dt,\end{aligned} \tag{2.18}$$

and s is a complex frequency variable.

For stress relaxation, the strain of representative volume element in real space is a constant, $\varepsilon = \varepsilon_{\text{const}}$ and in Laplace space, we have

$$\bar{\varepsilon} = \varepsilon_{\text{const}} / s\,. \tag{2.19}$$

Relaxation modulus is defined as:

$$E(t) = \frac{\sigma(t)}{\varepsilon_{const}}. \tag{2.20}$$

Combining Eqs. (2.17), (2.19) and (2.20), we obtain the relaxation modulus by reverse Laplace transformation:

$$E(t) = \frac{E_{EPS}}{2-\phi_V-(1-\phi_V)^{2/3}} \left(1-(1-\phi_V)^{2/3}\exp\left(-\frac{t}{\tau}\right)+\frac{E_{DER}(1-\phi_V)}{E_{DER}\left[(1-\phi_V)^{2/3}-(1-\phi_V)\right]+E_{EPS}\left[2-\phi_V-(1-\phi_V)^{2/3}\right]}\exp\left(-\frac{t}{\tau_2}\right)\right) \tag{2.21}$$

where the first relaxation time τ defined in Eq. (2.13) follows the Arrhenius law given by Eq. (2.3), and the second relaxation time τ_2 is the function of the first relaxation time τ and the modulus ratio between E_{EPS} and E_{DER} as

$$\tau_2 = \tau + \frac{E_{EPS}}{E_{DER}}\left(\frac{1}{(1-\phi_V)^{2/3}}-1+\frac{1}{(1-\phi_V)^{1/3}-(1-\phi_V)^{2/3}}\right)\tau\,. \tag{2.22}$$

The instantaneous modulus of the element can be obtained by letting t=0 in Eq. (2.21):

$$E_0 = \frac{E_{EPS}}{2-\phi_V-(1-\phi_V)^{2/3}} \left(1-(1-\phi_V)^{2/3}+\frac{E_{DER}(1-\phi_V)}{E_{DER}\left[(1-\phi_V)^{2/3}-(1-\phi_V)\right]+E_{EPS}\left[2-\phi_V-(1-\phi_V)^{2/3}\right]}\right). \quad (2.23)$$

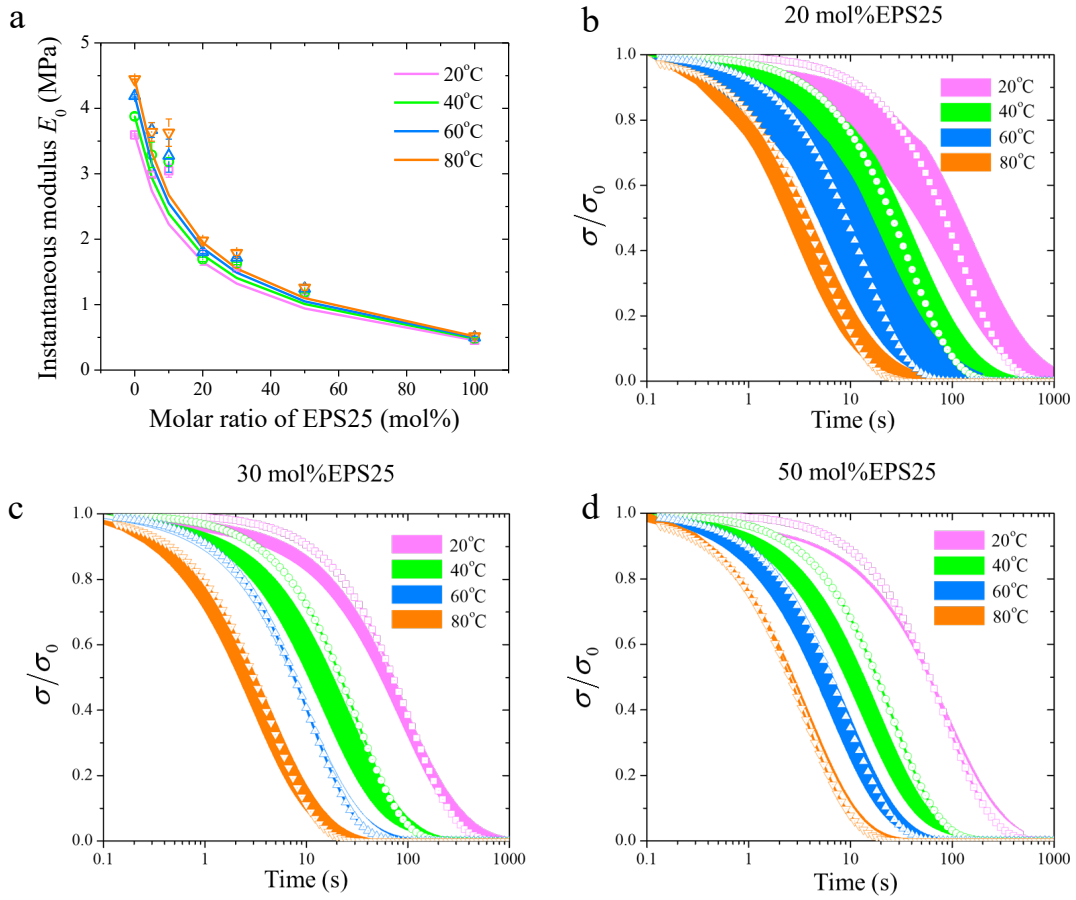

Figure 2.12: Comparisons between experiments and predictions of stress relaxation of the vitrimer. a Instantaneous modulus of the vitrimer as function of molar ratio of EPS25 at different temperatures: 20℃, 40℃, 60℃, and 80℃. The band plot of stress relaxation of the vitrimer **b** 20 mol% EPS25, **c** 30 mol% EPS25 and **d** 50 mol% EPS25 at different temperatures. In **a**, the solid curves are theoretical predictions and open dots are the experimental results (the error bars represent standard deviation). In **b**, **c** and **d**, the line with dots are theoretical predictions; and the colored bands are the range of experimental results and their widths represent the dispersion between the fast and slowest stress relaxations.

Figure 2.12a shows the prediction and experimental measurements of the dependence of the instantaneous modulus of the vitrimer network (at different temperatures) on the molar ratio between the two monomers: EPS25 and DER732. To make the predictions shown in Figure 2.12a, the instantaneous modulus of pure DER732 and pure EPS25 at different temperatures are given based on the experimental measurements. Without any fitting parameters, the agreements between the predictions of the relaxation modulus of the vitrimer given by Eq. (2.21) and the measurements shown in Figure 2.12b-d are satisfactory.

Based on the results in Eq. (2.17), we can also predict the creep of the vitrimer. During the creep, stress applied onto the material is a constant, $\sigma = \sigma_{\text{const}}$, which is

$$\bar{\sigma} = \sigma_{\text{const}} / s, \tag{2.24}$$

in Laplace space.

Creep compliance is defined as:

$$S(t) = \frac{\varepsilon(t)}{\sigma_{\text{const}}}. \tag{2.25}$$

Combining Eqs. (2.17), (2.24), (2.25), the creep compliance can be predicted as:

$$\begin{aligned} S(t) = & \frac{\left(1-\phi_V\right)^{-1/3}}{E_{DER}} + \frac{1-\left(1-\phi_V\right)^{1/3}}{E_{EPS}}\left(1+\frac{t}{\tau}\right) \\ & -\frac{E_{EPS}}{E_{DER}} \frac{1-\left(1-\phi_V\right)^{2/3}}{E_{DER}\left(1-\phi_V\right)^{2/3} + E_{EPS}\left[\left(1-\phi_V\right)^{2/3} - \left(1-\phi_V\right)\right]} \exp\left(-\frac{t}{\tau_3}\right), \end{aligned} \tag{2.26}$$

where

$$\tau_3 = \tau + \frac{E_{EPS}}{E_{DER}}\left[1-\left(1-\phi_V\right)^{2/3}\right]\tau. \tag{2.27}$$

As shown in Figure 2.6, creep of vitrimer can be significantly slowed down by introducing monomers with only regular covalent bonds (DER732) into the monomers with dynamic covalent bonds. When the molar concentration of EPS25 is 20%, the theoretical predictions given by Eq. (2.26) also agree well with experimental measurement without any fitting parameters.

2.2.7 Self-healing and reprocessing capability of the vitrimer with hybrid networks

Self-healing capability is often regarded as one important feature of vitrimer. Figure 2.13 shows the self-healing capability of the vitrimer network with two different molar ratios of EPS25: 5 mol% and 20 mol%. As shown in Figure 2.13c, for the vitrimer with 20 mol% EPS25, the strength of a broken sample increases gradually with the increase of healing time. After 6 hours, the strength of the healed sample (0.217 MPa) almost recovers to the original strength of the pristine sample (0.226 MPa) (Figure 2.13d). However, as shown in Figure 2.13h, for the polymer with 5 mol% EPS25, its strength can only reach a tiny fraction of the strength of a pristine sample, even after 48 hours healing process. The self-healing testing results are consistent with the stress relaxation measurement shown in Figure 2.4 and our hypothesis. Once the molar ratio of EPS25 can reach as high as 20 mol%, EPS25 forms the continuous phase, and thus the hybrid polymer network behaves like a viscous fluid as shown in Figure 2.4 and can be fully self-healed. However, if the molar ratio EPS25 is too low (e.g. 5 mol%), EPS25 cannot form a continuous phase, and thus the polymer network behaves like a solid as shown in Figure 2.4 and cannot be self-healed.

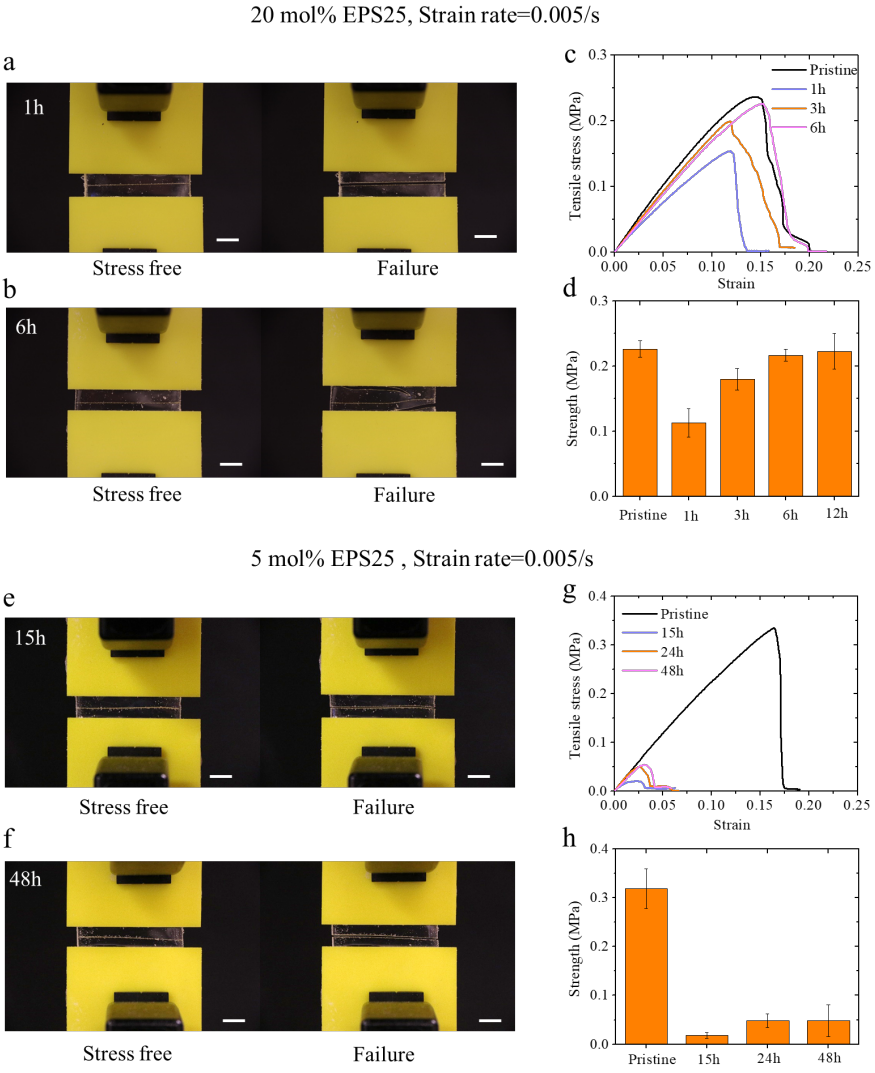

Figure 2.13: Self-healing capability of the polymer with two different molar ratios of EPS25. **a** The precut sample (20 mol% EPS25) after the healing time of 1 hour before and after tensile test. **b** The precut sample with the healing time of 6 hours before and after tensile test. **c** The stress-strain curve of the pristine sample and the precut samples with the healing time of 1 hour, 3 hours and 6 hours. **d** The strength of the pristine samples and the precut samples with healing time of 1 hour, 3 hours, 6 hours and 12 hours. **e** The precut sample (5 mol% EPS25) with healing time of 15 hours before and after tensile test. **f** The precut sample with the healing time of 48 hours before and after tensile test. **g** The stress-strain curve of the pristine sample and the precut samples with healing time of 15 hours, 24 hours and 48 hours. **h** The strength of the pristine samples and the precut samples with healing time of 15 hours, 24 hours and 48 hours. The scale bars in **a**, **b**, **e** and **f** are 1 cm. The strain rates in the experiments were 0.005/s.

The reprocessing capability is another highly desired feature of vitrimer in applications. The reprocessing experiments of the vitrimer with 20 mol% EPS25 are shown in Figure 2.14. The reprocessed sample of the vitrimer with 20 mol% EPS25 is a thin film with smooth surface as shown in Figure 2.14c. As shown in Figure 2.14d, the mechanical properties, e.g. modulus, strength and failure strain, of pristine and reprocessed samples are comparable. The vitrimer with 20 mol% EPS25, similar to pure EPS25, have excellent reprocessing abilities.

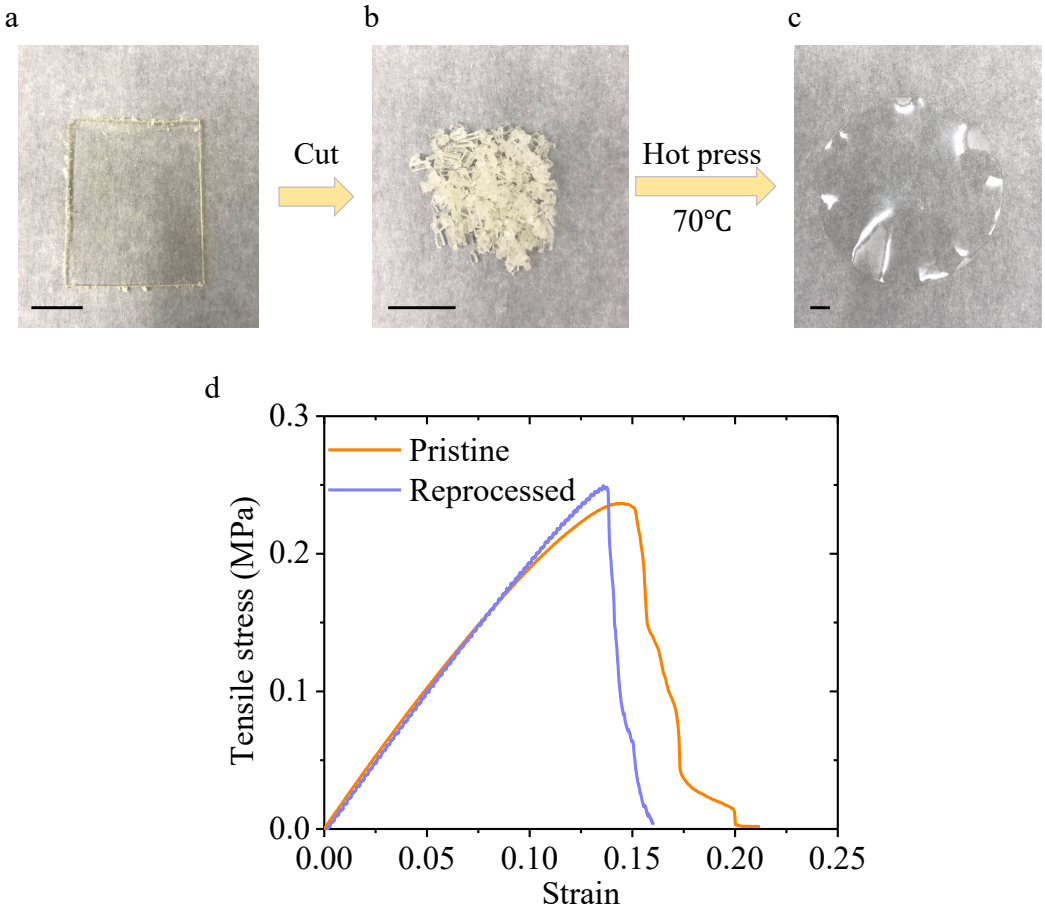

Figure 2.14: Reprocessing capability of the vitrimer with 20 mol% EPS25. a Photo of a pristine sample. **b** The vitrimer was fragmented to small pieces of size around 1 millimeter. **c** Photo of the reprocessed sample after heat pressing the fragmented pieces for 4 hours at 70°C with 5 tons compression load. **d** The stress-strain curve of the pristine sample and the reprocessed sample. The scale bars are 1 cm in **a**, **b** and **c**.

2.2.8 Toughness enhancement in the vitrimer with hybrid network

In the section, we show that the fracture energy of the vitrimer with hybrid network can be tailored by changing the molar ratio of EPS25 ranged from 5 mol% and 50 mol%. We conduct pure shear test on the vitrimer to measure the fracture energy. The fracture energy using pure shear test is calculated as

$$\Gamma_0 = W\left(\lambda_f\right) H, \tag{2.28}$$

where H is the height of sample in reference (unstretched) state, λ_f is the stretch for crack propagation of precut sample as shown in Figure 2.15b, and $W\left(\lambda_f\right)$ is the strain energy density of uncut sample at strain λ_f as

$$W\left(\lambda_f\right) = \int_1^{\lambda_f} s\left(\lambda\right) d\lambda, \tag{2.29}$$

in which $s\left(\lambda\right)$ is nominal stress and λ is stretch as shown in Figure 2.15a. The fracture experiments are conducted at strain rate 0.01/s and room temperature.

The fracture energy of vitrimers with hybrid networks as function of EPS25 content is shown in Figure 2.15c. We find that the fracture toughness of vitrimers with hybrid networks can be larger than the pure vitrimers (100 mol% EPS25) as well as the network only containing regular covalent bonds (0 mol% EPS25). The value of fracture energy attains its maximum (140.8 J/m^2) when the concentration of EPS25 is 30 mol%. The fracture energy is 1.45 times that of the pure vitrimers only containing EPS25 (97.3 J/m^2) and 1.7 times that of DER732 (82.9 J/m^2). The toughening mechanism is similar to that of most particle reinforced composite [29, 69].

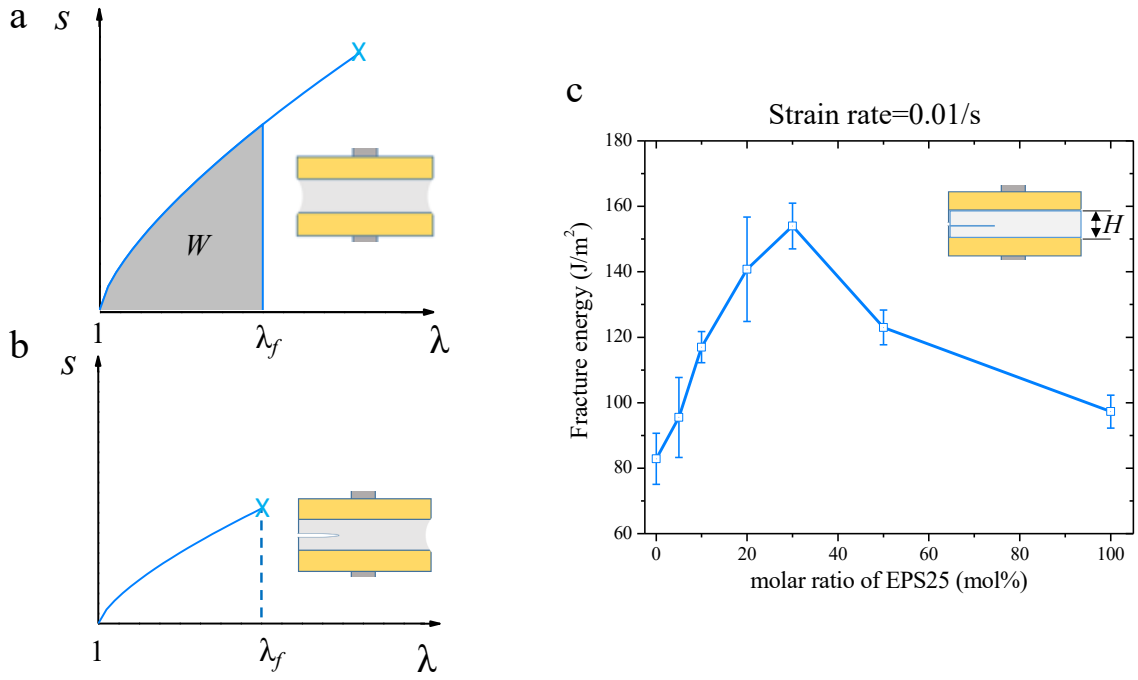

Figure 2.15: Fracture energy of vitrimers with hybrid networks. a Stress-stretch curve of pure shear test of a pristine sample. The strain energy density W is the area under the stress-stretch curve. **b** The stress-strain curve of the sample with a pre-crack. The failure stretch of the sample with a pre-crack is λ_f. The fracture energy of the sample can be calculated as $\Gamma_0 = W(\lambda_f)H$, where H is the height of sample in reference (unstretched) state. **c** The dependence of fracture energy of the polymer on the molar ratio of EPS25 at room temperature. The strain rate of pure shear experiments was set to be 0.01/s.

2.3 Conclusion

In this work, we have synthesized a polymer network with mixed regular and dynamic covalent bonds. Because of the phase separation of the two monomers, the polymer network behaves like a vitrimer even with only 20 mol% of the monomers containing dynamic covalent bonds. The vitrimer with hybrid networks exhibits excellent self-healing and reprocessing capabilities. Such observations are in contrast to most of the previous work on hybrid network

containing dynamic covalent bonds. We have also shown that by mixing the two monomers with and without dynamic covalent bonds, the creep of vitrimer can be greatly suppressed and its fracture toughness can be enhanced for a certain mixing ratio of the two monomers. Based on the assumption of phase separation and a spring-dashpot model, we have successfully predicted the stress relaxation and creep of the vitrimer with no freely adjustable parameters, which quantitatively agree well with experimental measurements. According to our knowledge, the specific model in this article for the vitrimer with hybrid network has been formulated for the first time.

In addition, as we mentioned in the article, the phase separation of the two main components (EPS25 and DER732) in the system is due to their high viscosity contrast. The detailed microstructure of the vitrimer with hybrid network is beyond the scope of this article, which, however, can be very interesting for the future work. Moreover, we have measured the fracture energy of vitrimer by simply following the classical pure shear test with a constant strain rate. Systematical studies of the fracture in vitrimer, such as the measurement and modelling of the rate-dependent fracture energy, is interesting and largely unexplored.

Chapter 2, in full, is a reprint of the material as it appears in "Mechanics of Vitrimer with Hybrid Networks", *Mechanics of Materials* (2021) 153: 103687, by Zhaoqiang Song, Zhijian Wang, and Shengqiang Cai. The dissertation author was the primary investigator and first author of this paper.

Chapter 3 Force-dependent bond dissociation explains the rate-dependent fracture of vitrimers

3.1 Introduction

Vitrimers have recently emerged as a promising class of polymer for a variety of potential applications [1]. Due to the presence of associative exchange reactions in the polymer network, vitrimers combine desired features of both thermosets and thermoplastics, such as stable high-temperature properties together with distinct reprocessability. Although intensive research has been conducted for understanding the constitutive properties of these new materials, their fracture behaviors have been largely unexplored.

Continuous exchange reactions of dynamic covalent bonds make vitrimers "strong" viscoelastic materials [70], namely, the dependence of their viscosity on temperature can be described by Arrhenius law. Despite intense efforts made in the past, quantitative modeling or prediction of fracture in viscoelastic polymers remains challenging [10]. The difficulties are mainly two-fold: first, the molecular origin of the fracture process, together with its dependence on rate is still unclear; this both blurs the interpretation of experimental results and hinders the rational design of tough polymers [71]; second, during crack propagation, bulk dissipation often competes with the crack propagation process in a complex and rate-dependent manner [6]. To tackle the first challenge, either simple theoretical models such as the Lake-Thomas theory or

empirical cohesive laws have been adopted [71]. The issue with these models, however, is that they are usually based on the assumption that the intrinsic fracture energy or the cohesive law is rate independent. To overcome the second difficulty, a linear rheology model is often adopted for viscoelastic polymers when modelling its fracture [8, 10, 13-16]. As a result, the bulk dissipation in the material caused by crack propagation is often quite rate-sensitive [10, 15]. However, those simplifications are often not sufficient to accurately capture the complex fracture phenomenon observed in viscoelastic polymers [17].

In this section, we aim to reveal critical insights into the fracture process of viscoelastic vitrimers through a combined experimental study and theoretical analysis. For this, we first conduct tear experiments on thin vitrimer films. By varying the thickness of the film, we can experimentally measure the dissipated energy in the fracture process zone (also known as intrinsic fracture energy) as well as the bulk dissipation in the film accompanied with crack extension (Figure 3.1). We find that the intrinsic fracture energy is highly rate-dependent, which is in contrast with the (rate-independent) assumption adopted in most previous studies on the fracture of viscoelastic polymers[10, 15]. Using concepts from the classical Eyring theory, we are then able to successfully explain the scaling relationship between the vitrimer's intrinsic fracture energy and the tearing speed. This study also reveals that the bulk dissipation in the vitrimer film is only weakly dependent on the tearing rate within a range that spans three orders of magnitude; this finding is in contrast to previous studies on conventional viscoelastic polymers and gels[72]. We

ascribe such weak rate-dependence of the bulk dissipation to the strong force sensitivity of the dynamic exchange reaction. Taken together, our study provides the first demonstration that thin-film tear test can be used to reveal critical insights into the fracture behavior of vitrimers.

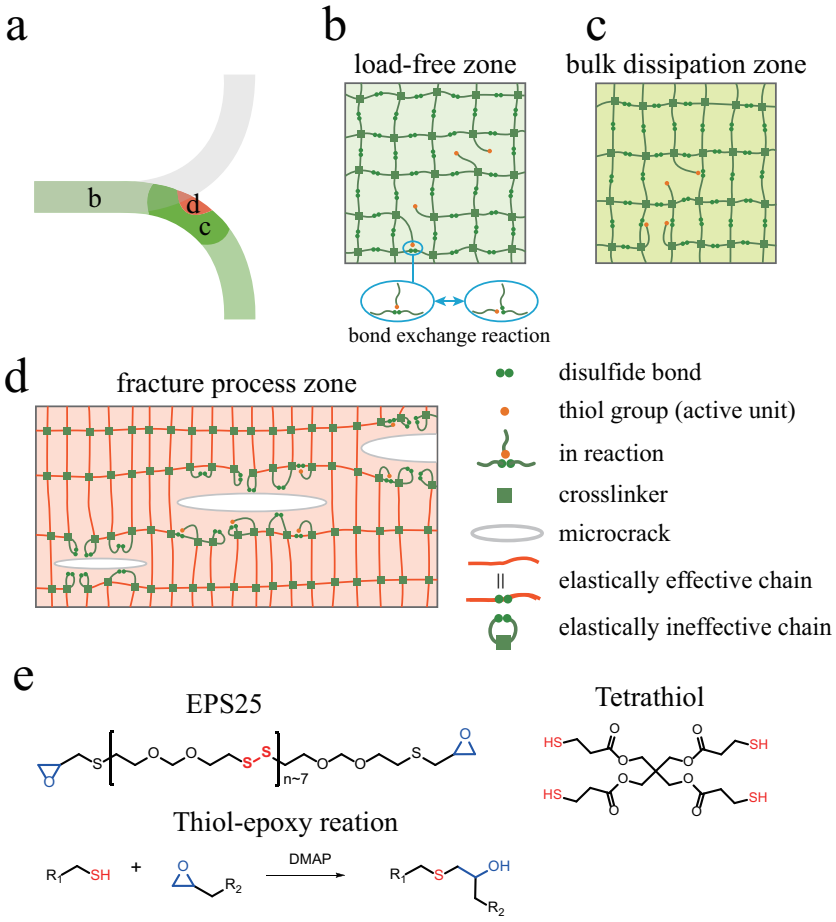

Figure 3.1: Chemical component of vitrimer and schematic of tear test of vitrimer with fracture process zone, bulk dissipation zone and load-free zone. a Fracture process zone and bulk dissipation zone in the vitrimer in one of two arms of the specimen during the tearing test from side view. **b** Associative exchange reactions (thiol-disulfide exchange reactions) can happen in load-free zone. The thiol group is from the crosslinking molecules. **c** Associative bond exchange reactions occur more frequently in the bulk dissipation zone. **d** The formation of microcracks in fracture process zone reduces the areal density of elastically effective crosslinks (Σ_b) and increases the density of elastically ineffective crosslinks. **e** Chemical structures of the monomer (EPS25) and the crosslinker (tetrathiol) for synthesizing the vitrimer in this study; crosslinking is achieved through thiol-epoxy reaction with DMAP (4-Dimethylaminopyridine) as the catalyst.

3.2 Results and discussion

Figure 3.2a shows the schematic of the tear test adopted in our study, where a vitrimer film, glued to an inextensible backing layer, is introduced with a cut along its center line. More details of the material can be found in references [57, 73]. The two separated arms are then stretched vertically in the opposite directions by a constant relative speed $v_0 = 2v$. Since the backing layers constrain the sample deformation, the crack is forced to propagate accordingly at a velocity v. Compared to many other fracture tests such as pure shear, single-edge notched tension, compact tension and center cracked tension, tear tests adopted in our experiment, similar to peeling test for measuring adhesion, have two advantages. First, the crack propagation speed can be easily controlled by the pulling speed. Second, by changing the sample thickness, the intrinsic fracture energy and the bulk dissipation can be simultaneously measured based on a simple scaling law without needing specific material models [65, 74].

In the experiments, we measure the force-extension relation of thin vitrimer films with different thicknesses ($h = 1$ mm, 1.5 mm, 2 mm and 2.5 mm) and different tearing speeds (v_0/h=0.01/s, 0.1/s, 1/s and 10/s) as shown in Figure 3.2c and Figure 3.3. To analyze our experiment results, we normalize the crack velocity by introducing the normalized crack velocity $\bar{V} = v_0\tau/h$, where τ=42 s is the characteristic relaxation time of the vitrimer determined by its stress relaxation measurement at a small strain (5%) as shown in Figure 3.4a, and h is the film thickness as shown in Figure 3.2a. It is noted that the characteristic relaxation time of the vitrimer

is very close to the time scale obtained from creep tests (Figure 3.4b) and the small-amplitude oscillation shear test (Figure 3.4c). In the experiment, the normalized crack velocity $\bar{V}$ is varied between 0.42 to 420. When $\bar{V}$ is larger than 1, the crack surface is smooth as shown in Figure 3.2b, indicating quasi-brittle fracture. In each experiment, the pulling force oscillates around a plateau value (F) after an initial increase (Figure 3.2c), indicating the stick-slip crack growth[65]. Here we do not study the stick-slip dynamics, and simply use the average tear force on plateau F to estimate the energy release rate G. Because of the simple geometry and the inextensible backing layer, the energy release rate can be given by $G=2F/h$[65].

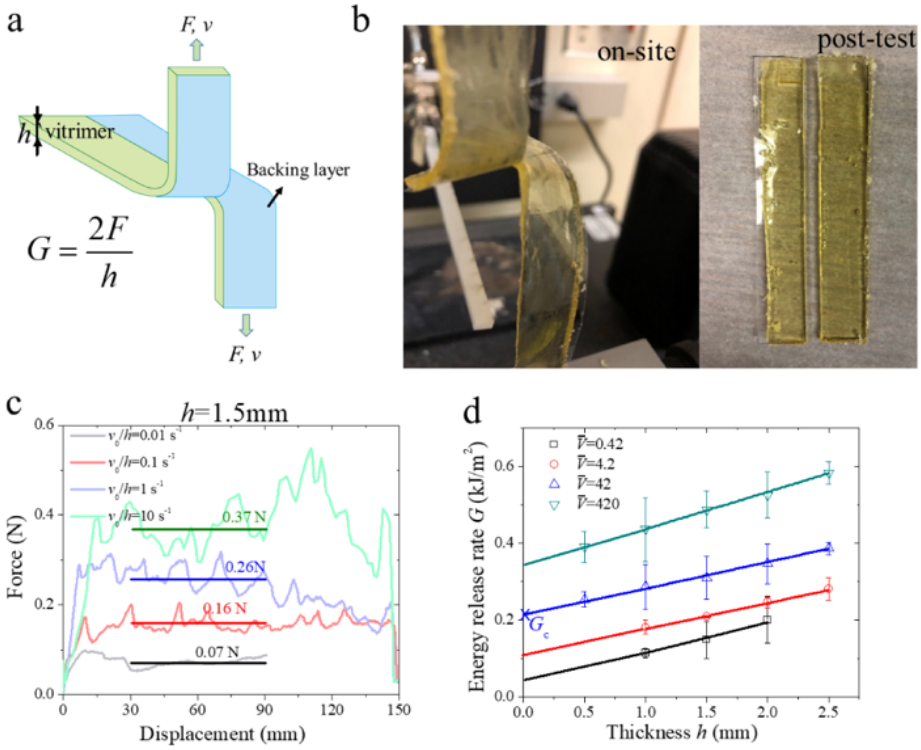

Figure 3.2: Results of tear test in vitrimer. a A schematic of tear test. **b** Tearing the vitrimer and the torn vitrimer with a smooth crack surface. **c** Force vs. Displacement of tear experiments with the film thickness of 1.5mm. **d** Energy release rate as a function of thickness of the films with different normalized crack velocities $\bar{V}$.

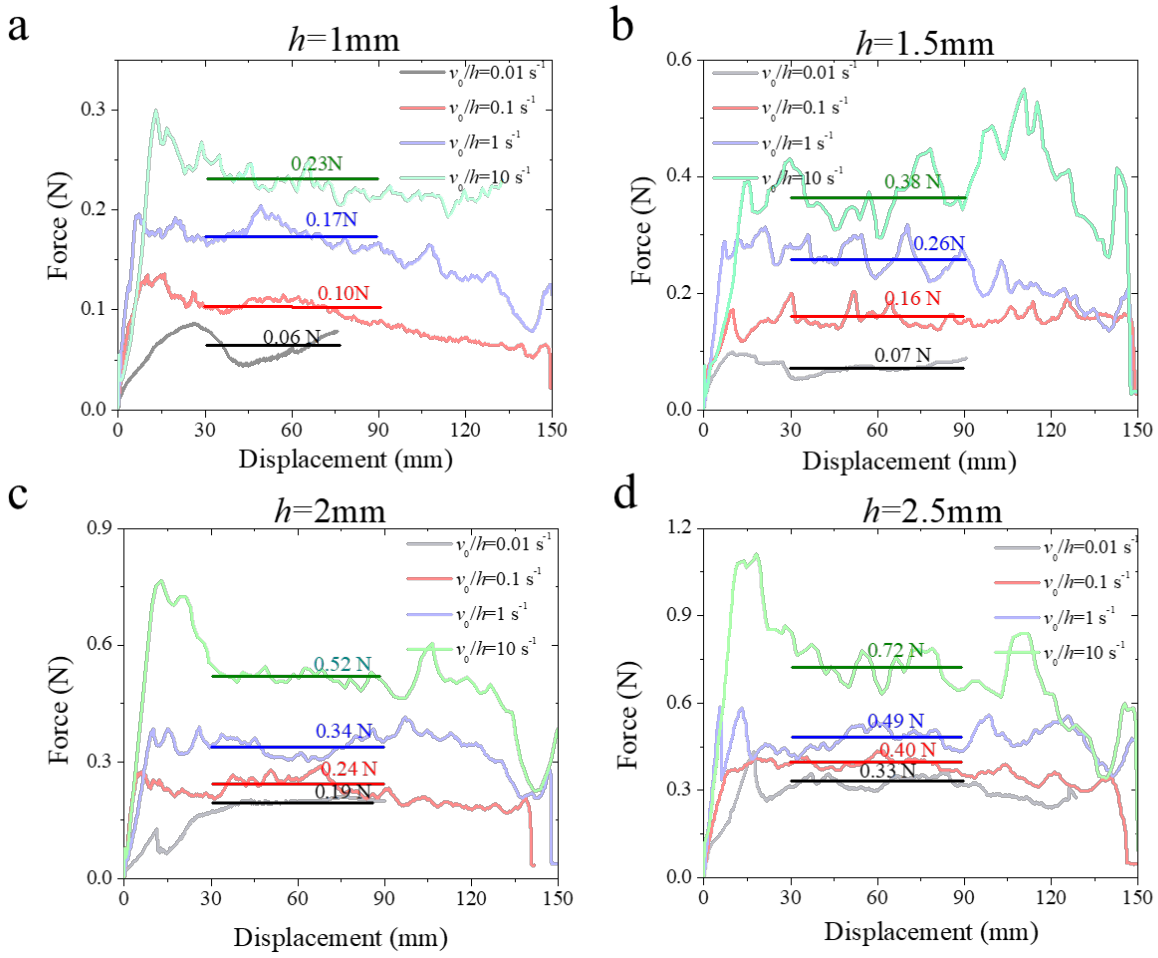

Figure 3.3: Force-displacement of tear experiments with different thickness. a 1mm, **b** 1.5mm, **c** 2mm, **d** 2.5mm.

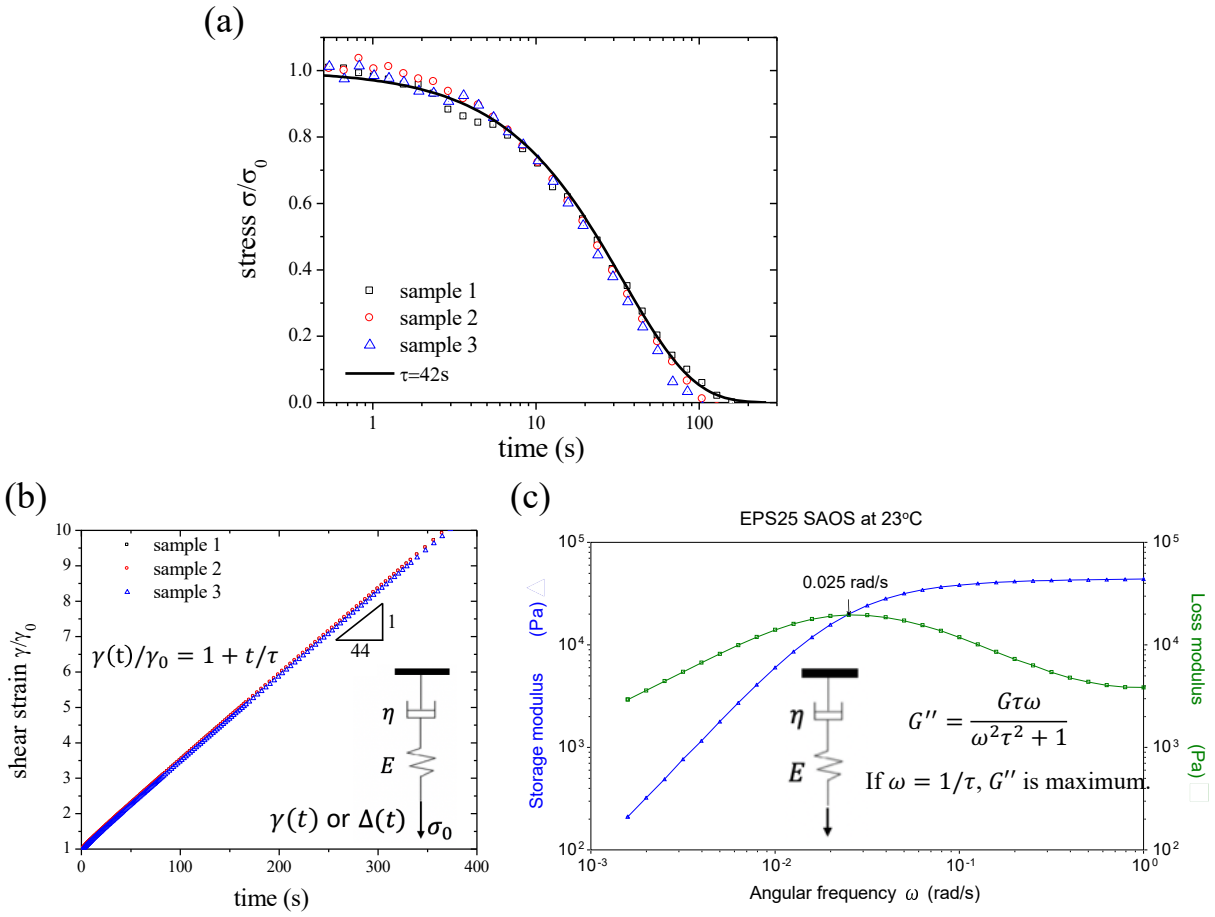

Figure 3.4: Rheology of vitrimer. a Stress relaxation of vitrimer at room temperature (23°C) with a small applied strain (5%), and the characteristic relaxation time predicted from Maxwell model is 42 s. **b** Creep of EPS25 at 23°C with the characteristic time as 44 s; **c** The small-amplitude oscillation shear experiment with the terminal relaxation time 40 s.

In Figure 3.2d, we plot the energy release rate G as a function of the film thickness h for four different crack velocities $\overline{V}$. We find that the relationship between the energy release rate and the film thickness is linear for all of the four different crack velocities ($\overline{V}$). Such linear relationship indicates that the size of the fracture process zone or "fractocohesive length" is much smaller than the film thickness [65, 74], as shown in Figure 3.1a, so we can separate the fracture energy into two parts:

$$G = G_c + G_d, \tag{3.1}$$

where G_c is the energy dissipation (intrinsic fracture energy) in the fracture process zone (Figure 3.1d), and G_d is the energy dissipated by viscoelastic loss in the bulk of the film (Figure 3.1c).

Based on de Gennes's model for fracture in a viscoelastic materials [75], the size of bulk dissipation zone in the material is given by $R_d = \frac{E_0}{E_\infty} R_0$, where R_0 is the fractocohesive length, E_0 is the instant modulus, and E_∞ is the equilibrium modulus. For a vitrimer, the equilibrium modulus is zero, so the characteristic size of bulk dissipation in a vitrimer is infinitely large. As a result, the film thickness *h* is the only relevant length scale for bulk dissipation and thus $G_d \propto h$ [74, 75]. Our experimental data in Figure 3.2d also suggests the linear dependency of G_d on h, so $G = G_c + w_p h$, where G_c is independent of h and w_p is the average density of bulk dissipation [76]. Based on this equation, the intersection of the fitted linear relationship between *G* and *h* with the vertical axis gives the intrinsic fracture energy G_c, as shown in Figure 3.2d. By measuring the slopes of the fitting lines relating the energy release rate *G* and the thickness *h* in Figure 3.2d, we can further measure the magnitude of w_p.

We envision different energy dissipation processes in the area near the crack tip and in the bulk. In the bulk, the energy dissipation is mainly through viscoelasticity resulted from dynamic exchange reactions. However, moving towards the crack tip, the chains are increasingly stretched due to the stress concentration. According to Eyring's theory [7], this leads to an increase in the bond exchanging rate, facilitating the formation of cavities or microcracks. With associative bond

exchange, though the crosslink density remains unchanged in the vitrimer, the elastically effective chains may become elastically ineffective (such as loops as shown in Figure 3.1d). Therefore, within a small region near the crack tip, the network loses its integrity as damage occurs.

Figure 3.5a plots the intrinsic fracture energy G_c as a function of the normalized crack velocity ($\bar{V}$). The strong rate-dependent intrinsic fracture energy of our vitrimer is in contrast to the assumption of rate-independent intrinsic fracture energy of viscoelastic polymers commonly adopted in previous studies [10, 15, 72]. It is also noted that the magnitude of G_c is much larger than the value predicted from the Lake-Thomas model (see Supporting Information). As shown in Figure 3.1, we believe that a fracture process zone, which is much larger than the mesh size of the polymer network, exists near the crack tip during tearing. To explain the scaling relationship between G_c and the crack velocity ($\bar{V}$), we extend the theory developed by Chaudhury and Hui [7, 77] and assume that in the fracture process zone, the energy dissipation is mainly caused by accelerated bond dissociation. Similar to the picture depicted by Lake and Thomas [78], the energy stored (denoted as W) in a polymer chain is entirely dissipated and we have $G_c \sim \Sigma W$, where Σ is areal density of polymer chains.

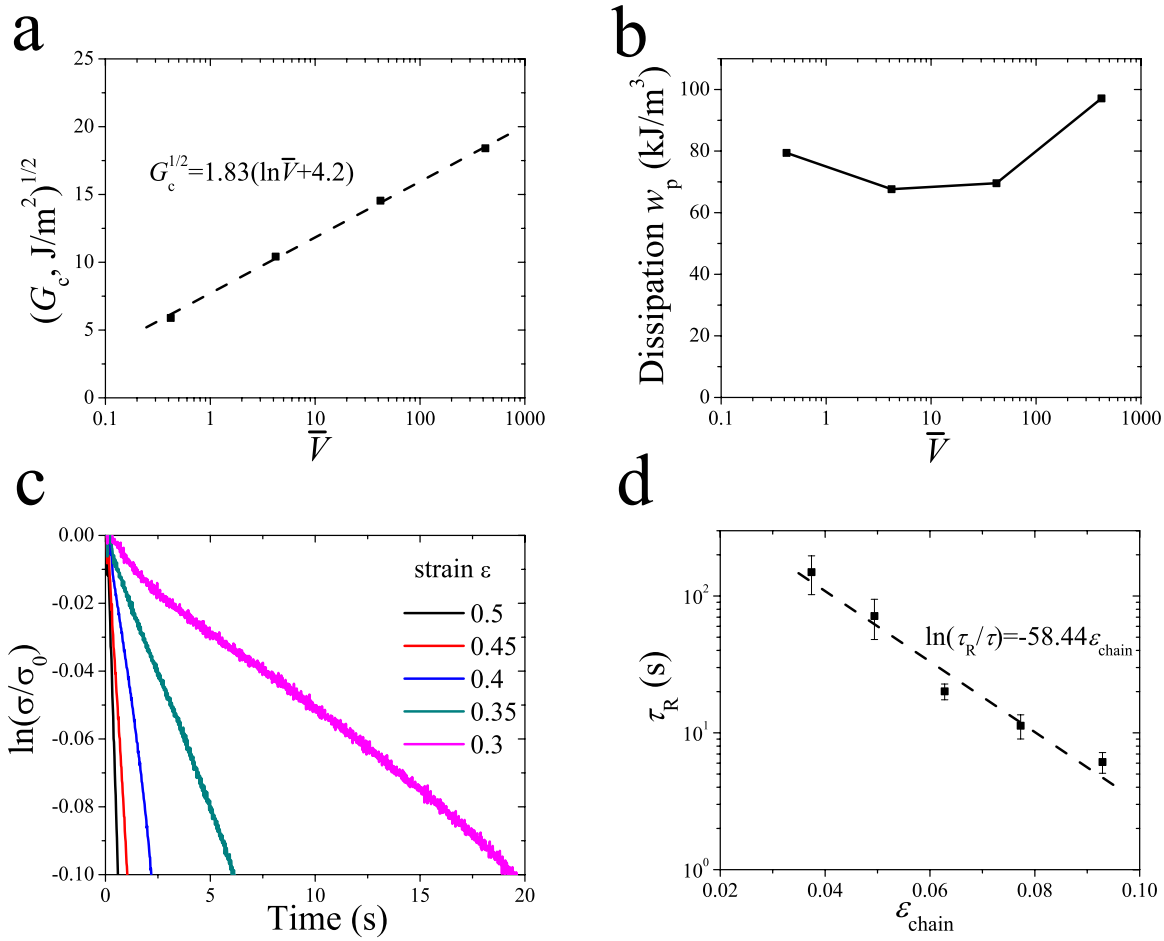

Figure 3.5: Fracture energy and stress relaxation of vitrimer. a The intrinsic fracture energy as a function of the normalized crack velocity, where the intrinsic fracture energies are the interceptions of the lines with vertical axis in Figure 3.2d; **b** Bulk dissipation of vitrimer with different normalized crack velocities, where bulk dissipation is the slopes of the lines in Figure 3.2d. **c** Stress relaxation of a vitrimer with different applied strains ε. **d** Relaxation time as a function of the chain strain ε_{chain}.

According to Eyring theory, the force f applied to a chain modifies the energy landscape for bond dynamics. This leads to an increase of bond exchanging rate $k_d = \tau^{-1} \exp\left(\frac{f\Delta_a}{k_B T}\right)$, where τ is the natural frequencies for bond exchanging [79]. In the fracture process zone, we assume that polymer chains that experience exchange reaction become elastically ineffective and lose their

load-bearing capacity (Figure 3.1d). Consequently, the decrease in the areal density Σ_b of elastically effective crosslinks follows the rate equation:

$$-\frac{D\Sigma_b}{Dt} = \tau^{-1} \exp\left(\frac{f\Delta_a}{k_B T}\right) \Sigma_b, \tag{3.2}$$

where k_B is the Boltzmann constant, Δ_a is the activation length of the covalent bond, *T* is the absolute temperature. The frequency of bond exchanging follows the Arrhenius law, $\tau = k_0 \exp(\frac{E_a}{k_B T})$, in which k_0 is a precursor and E_a is the activation energy of bond exchanging without external force. Considering linear chains with spring stiffness k_s, the force is related to deformation as $f = k_s \delta = k_s \varepsilon_{chain} L_0$, where δ, ε_{chain} and $L_0 = \sqrt{n} l$ are respectively the extension, strain and end-to-end distance of the polymer chain in a free standing state with *n* and *l* the number and length of Kuhn segments in a chain, respectively.

The force-sensitivity of bonds described in Eq. (3.2) can be experimentally explored by subjecting the vitrimer to a stress relaxation test. Indeed, during the relaxation process, once a polymer chain dissociates at fixed strain it no longer contributes to the network mechanics since free chains reassociate in a stress-free state, and the chain reassociation does not contribute to the stress. Therefore, the characteristic relaxation time of the network when a force *f* is applied on a polymer chain in Eq. (3.2) is $\tau_R = \tau \exp(-\frac{f\Delta_a}{k_B T})$. With the linear spring assumption of the polymer chain, we find that:

$$\ln\left(\frac{\tau_R}{\tau}\right) = -\frac{k_s L_0 \Delta_a}{k_B T} \varepsilon_{chain}. \tag{3.3}$$

This implies that the force sensitivity ($\frac{k_s L_0 \Delta_a}{k_B T}$) of the bond is a material parameter that remains constant during stress relaxation. The experimental results of the relaxation of vitrimer at different strains are shown in Figure 3.5c. We find that the stress reduction follows an exponential decay as: $\sigma/\sigma_0 = \exp(-t/\tau_R)$. To extract the force sensitivity of dynamic covalent bond, we employ the eight-chain model [80] and extract the strain of the polymer chain as $\varepsilon_{chain} = \sqrt{I_1/3} - 1$, where I_1 is the first invariant of the left Cauchy-Green deformation tensor and $I_1 = (1+\varepsilon)^2 + 2/(1+\varepsilon)$ for uniaxial tension with ε the tensile strain. Figure 3.5d shows the experimental result of relaxation time as a function of the strain, where a linear relationship between $\ln(\tau_R/\tau)$ and ε_{chain} is found and can be fitted by Eq. (3.3). The slope of line can be used to extract the force-sensitivity of dynamic disulfide bonds as $k_s L_0 \Delta_a/(k_B T) = 58.44$. This force sensitivity can be also estimated as follows. The spring stiffness of a polymer chain can be estimated by the modulus of the elastomer E and the mesh size of the network L_0 as $k_s \sim E L_0$, where $E \sim 1$ MPa is Young's modulus [73] and $L_0 \sim 10$ nm of our vitrimer. So, the spring stiffness of polymer chain k_s is in an order of 0.01 N/m. With the consideration of the activation length of disulfide bonds $\Delta_a \sim 0.3$ nm and temperature $T \sim 300$ K, we can estimate the force sensitivity is $\frac{k_s L_0 \Delta_a}{k_B T} \sim 10$, which has the same order of the value of force sensitivity measured from stress relaxation in Figure 3.5d.

We next investigate how the role of the bond's force sensitivity on the rate-dependent intrinsic fracture energy measured in the experiment (Figure 3.5a). We rewrite Eq. (3.2) as

$$v_c \frac{d\Sigma_b}{d\delta} = -\frac{1}{\tau}\Sigma_b \exp\left(\frac{k_s \delta \Delta_a}{k_B T}\right), \tag{3.4}$$

where the velocity of the chain stretch is $v_c = d\delta/dt$. v_c can be estimated from the crack velocity as follows: due to the existence of a backing layer, the material deformation is constrained into a small region of length h around the moving crack tip [65]. Therefore, a characteristic time for chain deformation is obtained as $t_0 = h/v_0$. Furthermore, since the surface is fully separated at the end of the deformation zone, we assume that chains are elongated from their natural length $\sqrt{n}l$ to the contour length nl when they travel through the deformation zone. Based on this conceptual picture, the velocity of the chain stretch can be estimated as $v_c = \left(\sqrt{n} - 1\right)L_0 v_0/h$ in Eq. (3.4). An average dissociation length of polymer chain can be defined as $\bar{\delta} = \int_0^\infty \frac{\Sigma_b}{\Sigma_0} d\delta$, where Σ_0 is total number of chains per unit area. By recalling Eq. (2.4) and following the derivation of Chaudhury [7], the integration can be obtained as $\bar{\delta} = \frac{k_B T}{k_s \Delta_a} \ln\left(\frac{(\sqrt{n}-1)k_s \Delta_a L_0}{k_B T}\bar{V}\right)$, if $k_s \Delta_a L_0 \bar{V} \gg k_B T$ [77, 81]. The average force on a chain before failure can be expressed as $f_{break} = k_s \bar{\delta}$ and the average energy stored in a polymer chain before breakage is $W = \frac{1}{2} k_s \bar{\delta}^2$. Invoking our scaling analysis, the intrinsic fracture energy G_c therefore scales as:

$$G_C \propto \left[\ln\left(\frac{(\sqrt{n}-1)k_s \Delta_a L_0}{k_B T}\bar{V}\right)\right]^2, \tag{3.5}$$

or $\sqrt{G_c} = \alpha(\ln(\bar{V}) + \beta)$, where the coefficient α is related to the thermally activated force-sensitivity of dynamic covalent bonds and the size of the fracture process zone, coefficient β is a rate-independent constant expressed as

$$\beta = \ln\left(\frac{(\sqrt{n}-1)k_s \Delta_a L_0}{k_B T}\right). \tag{3.6}$$

From Eq. (3.5), we know that $\sqrt{G_c} \propto \ln\bar{V}$, which agrees well with the result shown in Figure 3.5a. A good agreement between model and experiment is further obtained with $\beta = 4.2$ as shown by the fitting shown in Figure 3.5a.

We can also evaluate the coefficient β defined in Eq. (3.6), based on that $k_s L_0 \Delta_a/(k_B T) = 58.44$, determined from the stress relaxation measurements previously, and the number of Kuhn segments n. To estimate the number of Kuhn segments of the vitrimer for our experiment, we conducted uniaxial tension tests on a thin vitrimer strip with a strain rate of 100%/s. For such a strain rate, the bond exchange reaction is negligible during the deformation. We found that the rupture strain of the vitrimer strip is around 150% as shown in Figure 3.6. According to the eight-chain model [80], the chain locking stretch (defined as the stretch of a chain when it is fully extended) can be estimated from the rupture strain of the vitrimer strip as $\lambda_L = 1.54$, under the assumption that the polymer chain is fully extended at rupture. The number (n) of Kuhn segments could further be related to the chain locking stretch (λ_L) as $\lambda_L = \sqrt{n}$, which yields $n = 2.4$. Consequently, we can obtain $\beta = 3.5$, which is close to the one estimated from the measurement of the rate-sensitivity of the intrinsic fracture energy shown in Figure 3.5a.

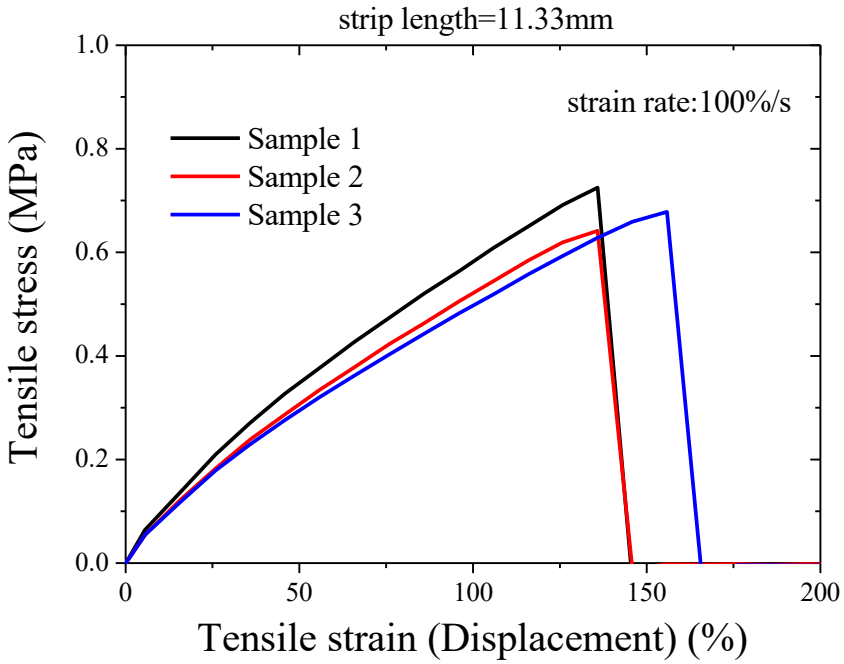

Figure 3.6: The uniaxial tension test of vitrimer strips. The strain rate is 100%/s and the strip length is 11.33 mm.

Another notable result of this study pertains to the rate of bulk dissipation w_p. Indeed, Figure 3.5b suggests that it is only weakly dependent of the tearing rate, varying between 65~98 kJ/m^3 over the range of $\bar{V}$ from 0.42 to 420. This weak rate-dependence is in sharp contrast to the rate-dependent bulk dissipation of most viscoelastic polymers studied in the past [72]. For a linear viscoelastic material, it is expected that bulk dissipation should reach a maximum when the loading time is comparable to the single relaxation time of the material, and reach a minimum when the loading rate is too small or too large, as shown in Figure 3.7a-b. We postulate that such difference is caused by the nonlinear viscoelasticity of the vitrimer, where the rate of bond exchange increases at larger forces or strains ($\bar{V}$) and thus there is no single relaxation time in the material. The stretch-stress curve of a strongly force-sensitive vitrimer (using the parameter

$k_s L_0 \Delta_a/(k_B T) = 58.44$) experiencing loading-unloading history at different loading rates, is calculated by combining the classic transient network theory with Eyring's theory and steady-state kinetics for chain dissociation and reassociation [6], as shown in Figure 3.7c. The strong force-sensitivity of dynamic covalent bonds leads to large bulk dissipation even when $\bar{V}$ is very large e.g. $\bar{V}$ =42, 420, as shown in Figure 3.7d. A more detailed study of w_p in the tear test of a vitrimer film requires a full-field simulation of the tearing process with a nonlinear viscoelastic material model, which is a challenging task and has not been achieved in the literature yet. However, in this work, we circumvent this difficulty and simply extract the effect of w_p on the fracture energy based on geometric scaling.

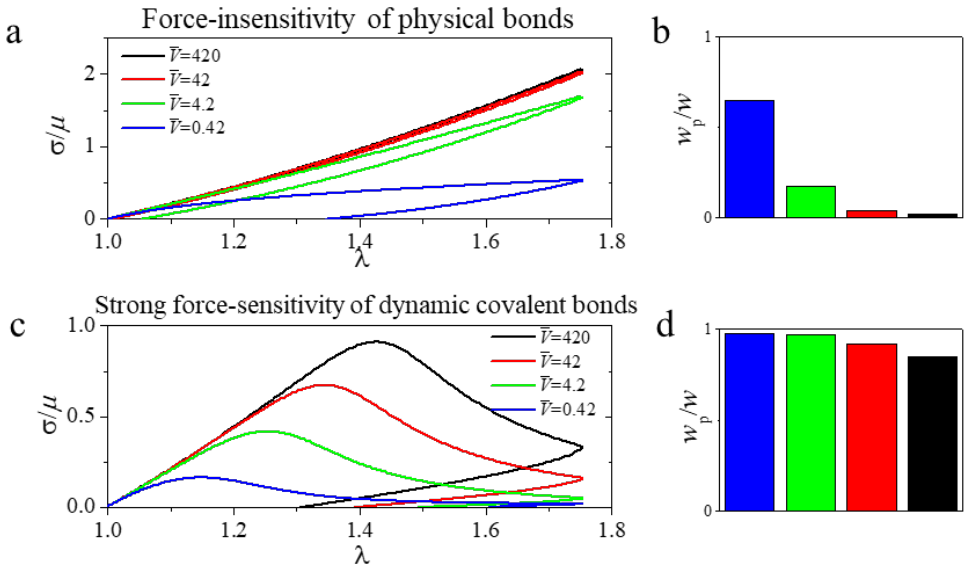

Figure 3.7: Stress-strain responses of materials with force-insenstiviy and with a strong force-sensitivity. a Stress-strain curve of a force-insensitivity polymer experiencing loading-unloading history at different loading rates ($\bar{V}$). **b** The proportion of dissipation energy (w_p) in total strain energy (w) of a force-insensitivity polymer. **c** Stress-strain curve of a strong force-sensitivity vitrimer experiencing loading-unloading history at different loading rates. **d** The proportion of dissipation energy (w_p) in total strain energy (w) of a strong force-sensitivity vitrimer.

3.3 Conclusion

In summary, our study clearly shows that tear test of a vitrimer film is an effective way to explicitly reveal the molecular origins of rate-dependent energy dissipation associated with its fracture. Through the experiment, we find that the intrinsic fracture energy of vitrimers with disulfide bonds is highly rate-dependent while their bulk dissipation is rather rate-insensitive during fracture; this is significant contrast to most previously studied viscoelastic polymers. By assuming a small fracture process zone near the crack tip within which the acceleration of bond dissociation is the main energy dissipation mechanism, we could explain the scaling relationship between the intrinsic fracture energy and the normalized crack velocity based on the classical Eyring theory.

Chapter 3, in full, is currently being under review, “Force-dependent bond dissociation explains the rate-dependent fracture of vitrimers”, by Zhaoqiang Song, Tong Shen, Franck Vernerey and Shengqiang Cai. The dissertation author was the primary investigator and first author of this paper.

Chapter 4 Non-steady fracture of transient networks: the case of Vitrimer

4.1 Introduction

Understanding the conditions that lead to fracture in polymeric materials is an important problem of both industrial and fundamental interests. A common agreement is that fracture of polymer originates from successive chain scission resulting from the application of an excessive stress on the network[71]. This consideration leads to the early work of Griffith that predicts the onset of crack propagation based on the competition between two quantities: the crack tip driving force G_{tip} that provides the fuel for fracture, and the intrinsic fracture toughness G_0, which represents the material's resistance to fracture [82]. To propagate a crack, the former needs to reach or exceed the latter. This criterion further leads to deformation-based measurements such as the critical crack opening distance (COD) [83], critical stretch [84], or network damage models based on the chains' stretch limit [85-87]. These models have so far been instrumental in predicting the fracture of covalent polymer networks that are both elastic [82, 88-90] and viscoelastic [10-13, 16, 91, 92]. However, materials formed by weaker bonds (e.g., covalent adaptable bonds [93], ionic interaction [94, 95] or entanglements [96-98]) exhibit a much richer fracture behavior that do not only depend on deformation, but also greatly depend on the rate of loading [96, 97, 99]. Due to their inherent weakness, these bonds are prone to spontaneous dissociation and reassociation over

time, under the effects of thermal fluctuations. This leads to a wide spectrum of rate-dependent mechanical response wherein the networks behave like viscous fluid at slow loading rates (relative to the rate of bond exchange), while they exhibit elastic solid-like behavior at fast loading [96]. This coupling between deformation and network relaxation makes the prediction of fracture challenging, since the mechanical response becomes both time and rate dependent. In addition, the physical picture of chain scission at its stretch limit is no longer valid as a chain may dissociate in any conformation. This raises questions about the molecular origin of fracture and on its macroscopic manifestation and particularly, the conditions for its nucleation and its speed of propagation. Although some initial efforts were taken to understand the role of loading rate on fracture [97, 100] in transient networks, a systematic study of the physical rules behind crack characteristics, initiation and propagation, is still not established.

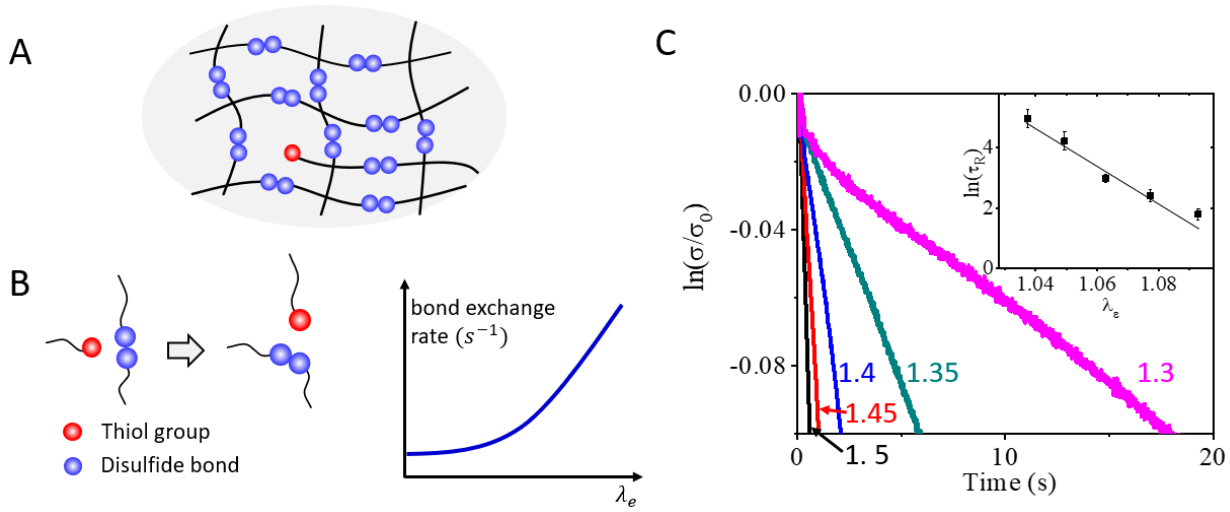

Figure 4.1: Bond dynamics in the transient network. A Schematic of the transient network, where bonds can spontaneously dissociate at rate k_d and associate at rate k_a. **B** As a result of the bond dynamics, cracks in these networks are transient in nature as they nucleate and heal in time. **C** Stress relaxation experiment at different strain ϵ with uniaxial tensile loading.

To address these questions, we have carried out fracture experiments on a vitrimer network formed by disulfide bonds. In the presence of a catalyst, the bond exchange reaction (Figure 4.1B) can be triggered by thermal fluctuations at room temperature [101]. A full characterization of this network has been performed in our previous study [102]. In this paper, we are specifically interested in the stress relaxation experiment as it unveils the rate of bond exchange reaction (i.e, the bond dynamics). For this, we conducted a series of stress relaxation experiment at different stretch levels, in which the inverse of characteristic relaxation time is interpreted as the average rate of bond exchange at the applied deformation [103]. Our result shows that this rate, denoted as k_d, is particularly sensitive to the level of chain stretch λ_e. After calibration, we found that bond dissociation is well described by the relation $k_d = k_d^0 \exp(\alpha\lambda_e)$ where k_d^0 is the spontaneous rate and $\alpha = 58.4$ is a sensitivity parameter, as shown by the relaxation results in Figure 4.1**:**C and the fitting in its inset. This exponential dependency agrees with Eyring's model [48, 104] based on the transition state theory. To characterize the response of this vitrimer in fracture, we then devised a pure-shear fracture experiment, where a pre-cut sample of width $L = 35\,mm$, height H_0 $(10\,mm)$ which contains a pre-cut of length $c_0 = 15\,mm$ was stretched vertically at constant nominal strain rate $\dot{\lambda} = \dot{H}/H_0$ (Figure 4.2A). In what follows, this variable is normalized by the bond dynamics rate k_d^0 so that the ratio $W_0 = \dot{\lambda}/k_d^0$ (denoted as the nominal Weissenberg number) describes the competition between network deformation and reconfiguration.

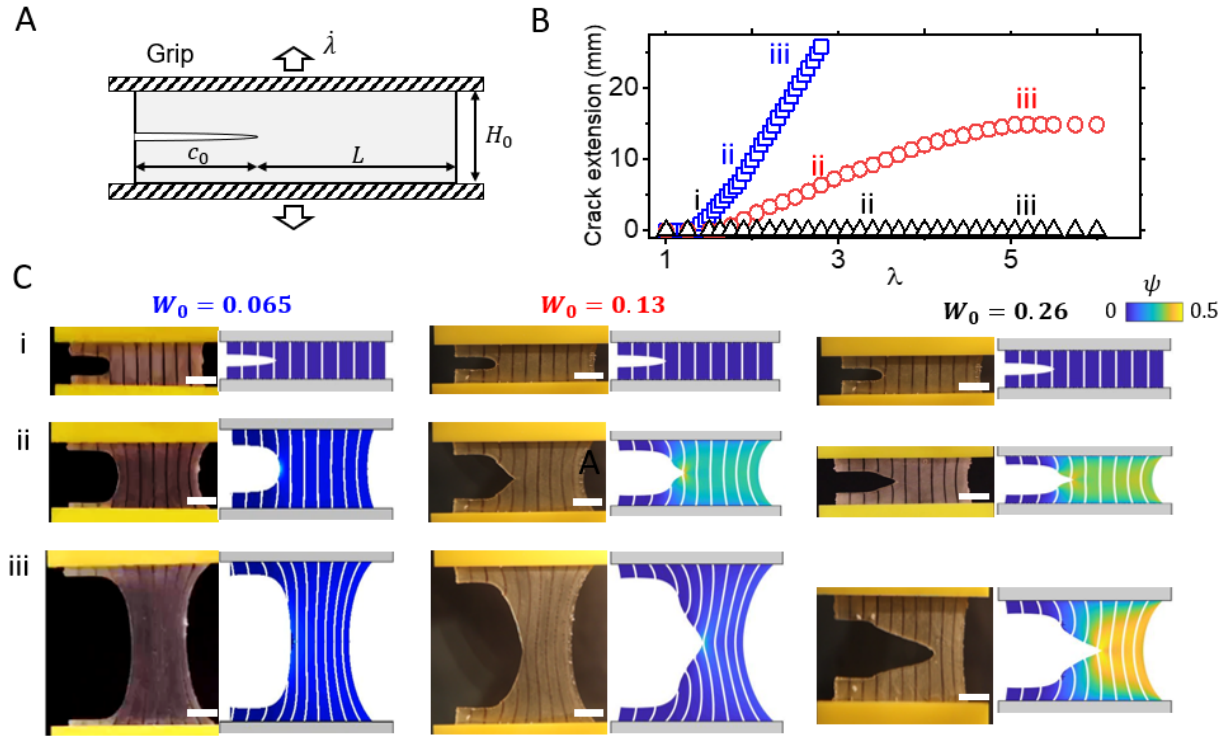

Figure 4.2: Pure shear experiments of transient networks. **A** A schematic of fracture of the specimen, the crack tip driving force $\mathcal{G}$ measures the elastic energy infused to the crack tip. **B** Measurement of crack extension during the deformation history. **C** Experimental and finite element simulation snapshots of crack profile under different loading rates. The scale bars are 10 mm.

Our measurements of crack extension (Figure 4.2B and C) reveal three distinct characteristic regimes depending on the magnitude of W_0. For a small loading rate ($W_0 = 0.065$), the induced cut opens continuously and eventually becomes a curved edge. Over the course of the experiment, no observable fracture is recorded. For an intermediate rate ($W_0 = 0.13$), a peculiar phenomenon occurs where a sharp crack first nucleates from the tip of the cut and quickly propagates with a characteristic trumpet-shaped profile (Figure 4.2C). However, the propagation stops at a finite time, after which the crack "dies" and gives rise to a blunted edge. We note that this phenomenon is observed in covalently crosslinked networks, since a propagating crack usually

travels continuously at constant velocity through the specimen [105] under monotonic loading. Finally, for fast loading ($W_0 = 0.26$), we similarly observe an initial blunting of the cut, quickly followed by crack nucleation. In this case, this new-born crack accelerates and fully ruptures the specimen. We used image processing techniques and measured the crack extension as a function of stretch λ (Figure 4.2B), where we see that crack propagation is highly unsteady with varying velocity. The above observations cannot be explained by the current fracture theories for the following reasons. First, the onset of fracture highly depends on loading rate in addition to the level of deformation, therefore a criterion derived from the elastic theory such as the Crack Opening Distance (COD) or the critical stretch cannot be used. Second, the life of a propagation crack varies between loading conditions, where it may accelerate, decelerate or even stop under monotonic loading.

To understand these observations, we have recently developed a theoretical framework that allows one to evaluate the energetic fracture criterion and calculate crack velocity based on the stress field and bond dynamics [6]. Combining this approach with Finite Element simulations, we were able to simulate the non-steady state fracture behavior of the vitrimer and qualitatively match the experimental crack profiles in Figure 4.2C. Predominantly, our simulations suggest that crack initiation and propagation are associated with the increase of strain energy density ψ stored in the network, which itself is a function of nominal Weissenberg number W_0 and loading history. In addition, the speed of the crack depends on both the magnitude of ψ and the sensitivity of bond

dynamics k_d upon deformation. In summary, our simulation work has allowed us to identify three kinetic rates that collectively govern fracture in transient networks: the rate of loading, the rate of bond dynamics and the rate of crack propagation. The way by which these rates compete during fracture is however unclear. This work's objective is thus to combine theoretical analysis with experiment and extract the physical mechanisms behind these peculiar phenomena.

4.2 Results and discussion

4.2.1 Fracture controlled by non-equilibrium processes

Recalling from the work of Griffith [82], the criterion for crack propagation relies on the competition between the crack tip driving force G_{tip} and material's fracture resistance G_0. As shown by Rivlin and Thomas [88], G_{tip} depends on both the stored elastic energy density ψ in the specimen and its geometry. The former determines the energy stored in the system while the latter dictates the amount of energy fed to the crack tip. As shown by our previous serial work [6, 106-108] on the Transient Network Theory (TNT), ψ is directly related to the elastic distortion of the network. However, since the network constantly reconfigures, its distortion is usually different from the specimen deformation. To quantify the network distortion, the TNT introduced the so-called chain conformation tensor $\boldsymbol{\mu} = \boldsymbol{F}_e\boldsymbol{F}_e^T$ that measures the mean squared elastic deformation of chains in the network. At the stress-free state, $\boldsymbol{\mu}$ is equal to the identity tensor $\boldsymbol{I}$, indicating an undeformed state. Over the deformation history, the TNT allows us to track the chain

conformation and the stored elastic energy via their evolutions that read $\dot{\boldsymbol{\mu}} = \boldsymbol{L}\boldsymbol{\mu} + \boldsymbol{\mu}\boldsymbol{L}^T - k_d\left(\boldsymbol{\mu} - \frac{3}{tr(\boldsymbol{\mu}^{-1})}\boldsymbol{I}\right)$ and $\dot{\psi} = \frac{s}{2}(\boldsymbol{\mu}:\boldsymbol{L}) - k_d(\psi - \psi_0)$. The tensor $\boldsymbol{L} = \boldsymbol{L}(\dot{\epsilon})$ is the velocity gradient related to the Hencky or true strain rate $\dot{\epsilon}$ [6], and s is the shear modulus of the network. In both equations, the terms associated with $\boldsymbol{L}$ describe the effect of external load while the terms associated with k_d are related to network reconfiguration. In what follows, we will explore the fracture criterion based on these two equations.

4.2.2 Crack initiation and arrest

In a pure-shear extension experiment, the specimen only deforms along x and z directions (Figure 4.3A). Therefore, the chain conformation tensor $\boldsymbol{\mu}$ simplifies to a diagonal form expressed in the $x - z$ coordinate system with $\boldsymbol{\mu} = [1/\lambda_e^2,\ 0; 0, \lambda_e^2]$ where λ_e is the mean chain stretch along z direction. During deformation, the evolution of λ_e and the stored elastic energy density ψ become:

$$\dot{\lambda}_e = \frac{\lambda_e k_d}{2}\left[2W + \frac{2}{(\lambda_e^4 + 1)} - 1\right] \tag{4.1a}$$

$$\dot{\psi} = \frac{s k_d}{2}\left[2W\left(\lambda_e^2 - \frac{1}{\lambda_e^2}\right) - \psi\right] \tag{4.1b}$$

where $W = \dot{\epsilon}/k_d$ is the true Weissenberg number. At the initial state, this quantity is equal to the nominal Weissenberg number $W = W_0$. We note that Eq. (4.1) can describe a wide spectrum of network response ranging from elastic solid to viscous fluid-like behavior. At extremely fast loading ($W \to \infty$), Eq. (4.1) becomes $\dot{\lambda_e} = \dot{\epsilon}\lambda_e$ and $\dot{\psi} = \frac{\mu}{2}\dot{\epsilon}(\lambda_e^2 - 1/\lambda_e^2)$ which are the evolution laws for Neo-Hookean elastic solid [106]. At the other extreme ($W \to 0$), Eq. (4.1)

degenerates to $\dot{\lambda_e} = \dot{\psi} = 0$, showing that the chains remain unstretched regardless of macroscopic deformation, similar to the behavior of Newtonian fluid. In addition, our previous studies [6] show that when W is held constant during deformation, the chains evolve towards a steady-state stretch λ_e^s. As shown by Figure 4.3B, λ_e^s increases monotonically with W, characterizing a more elastic solid-like behavior. When $W > 0.5$, the steady-state stretch diverges, implying that rate of elastic deformation is predominant over bond dynamics. We note here that our experiments (Figure 4.2) were conducted at constant $W_0 = \dot{\lambda}/k_d$, which is equivalent to a monotonically decreasing true Weissenberg number W with stretch, given by $W = W_0/\lambda$. As a result, the specimen response becomes more fluid-like during deformation and therefore fracture becomes less favorable. To relate the specimen's energy state to fracture, we first note that the crack tip driving force is defined as the energy consumed by unit area of crack extension as $G_{\text{tip}} = \lim_{\delta A \to 0} (\delta \Pi_c / \delta A)$. The term $\delta \Pi_c$ is the energy consumed by crack propagation, which can be calculated from the conservation of energy:

$$\delta \Pi_c = \delta \Pi_w - \delta \Pi_e - \delta \Pi_{\text{d}}. \tag{4.2}$$

where $\delta \Pi_w$ is the work done by external forces $\delta \Pi_e$ the change in elastic energy and $\delta \Pi_d$ the energy loss by viscous dissipations. Physically, $\delta \Pi_w - \delta \Pi_e$ represents the system's dissipative energy, either by bond dynamics or crack propagation. For fluid-like materials, $\delta \Pi_d$ becomes the dominant term for dissipation and therefore fracture is unfavorable. Contrarily, for elastic network, $\delta \Pi_d = 0$ and fracture becomes the only dissipative mechanism. In our previous work, Eq. (4.2)

was numerically evaluated by computing $\delta\Pi_w$, $\delta\Pi_e$ and $\delta\Pi_d$ from the finite element solution of the stress field [6]. In this work, to analytically investigate the problem, we simplify the problem by assuming a relatively sharp crack tip (small to moderate deformation) and apply a binary simplification to the stress field (i.e., the specimen is split into a uniformly loaded and a fully unloaded region) as shown in Figure 4.3A. Under such simplifications, a first order approximation of the crack tip driving force $\mathcal{G}$ can be obtained as:

$$G_{\text{tip}} = \frac{\lambda}{\lambda_e} \mathrm{H}_0 \psi(W_0, \lambda) \tag{4.3}$$

This expression takes a similar form as that its counterpart for elastic materials [88] with two major differences. First, due to bond dynamics, the strain energy ψ is rate and history dependent as shown by Eq. (4.1). Second, there is a factor λ/λ_e due to the mismatch between chain stretch and the applied deformation. For elastic networks, $\lambda_e = \lambda$ and Eq. (4.2) degenerates to its form for elastic solids [75]. To further simplify our analysis, we assume that the rate of bond dynamics remains constant as $k_d = k_d^0$ in the specimen due to the low elastic deformation. However, we will show in next section that accelerated bond dynamics becomes critical in a small region near the crack tip, where the deformation is greatly amplified. Using Eqs. (4.1) and (4.3), Figure 4.4A plots the change of G over the loading history for the three strain rates used in experiment. By comparing its value with the intrinsic fracture toughness G_0 (obtained as $70\,J/mm^2$ by fitting with experiment on crack initiation), we split Figure 4.4A into two regimes, the flow regime ($G_{\text{tip}} < \mathrm{G}_0$) shown in grey background and crack propagation regime ($G_{\text{tip}} > \mathrm{G}_0$) with white

background. For a slow loading rate ($W_0 = 0.065$), the $G_{\text{tip}} - \lambda$ curve remains in the flow regime and no fracture occurs. Physically, this means that the elastic energy in the specimen is too low to break the chains and initiate crack propagation. At faster loading, we see a non-monotonic behavior where the specimen first enters the crack propagation regime but eventually drops towards the flow regime as it becomes increasingly fluid-like. This yields the peculiar crack arrest behavior, where the crack only propagates within a range of deformation. According to Eq. (4.3), this "propagation window" solely depends on the experimental control of the specimen height H_0 (set as 10 mm in experiment) and the nominal Weissenberg number W_0. Therefore, one way to regulate the fracture of the specimen is to control the propagation window via these two parameters.

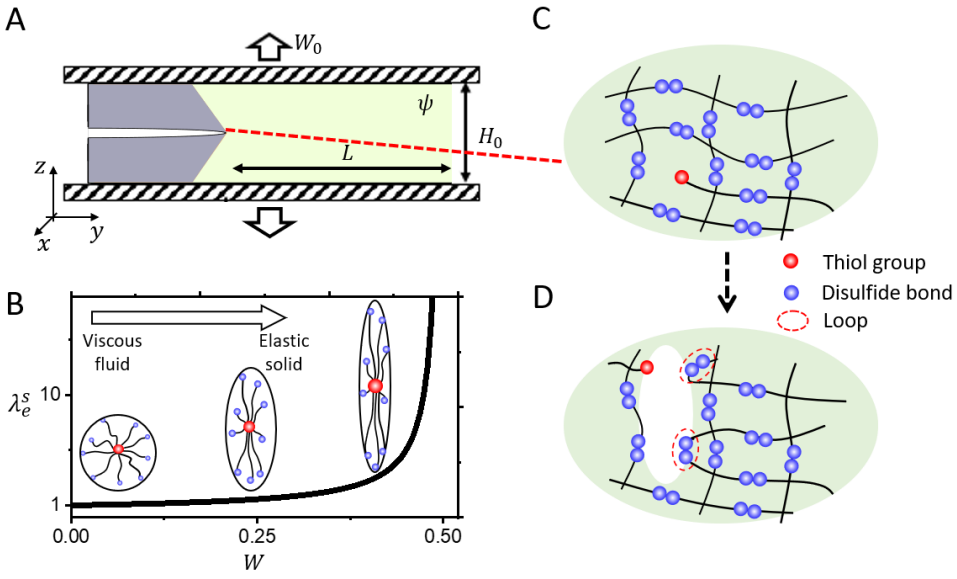

Figure 4.3: Bond dynamics at the crack tip. (A) A schematic of fracture of the specimen. (B) Under constant true Weissenberg number loading, the mean chain stretch λ_e increases monotonically with W, the insets are the graphical visualization of chain stretch along vertical direction. (C) and (D) Schematics of cavity and loop chains formation when the network is under tension.

4.3.3 Load dependent crack velocity

We note that the above analysis on crack arrest was carried out by assuming an infinitely large specimen (i.e., the crack never propagates through the sample). Since the experiments were conducted on a finite size specimen, the crack may travel through the specimen before it is arrested. To capture the effect of the specimen's finite size, we thus introduce another nondimensional parameter, the extension parameter $Z = \dot{c}/Lk_d^0$, where $\dot{c}/k_d^0$ is a characteristic crack length derived from the Trumpet model by De Gennes [13, 91]. This length describes the size of a region around the crack tip within which the network behaves like an elastic solid due to the amplified strain rate. A large Z ($Z \gg 1$) indicates a rapid crack propagation such that network reconfiguration becomes negligible. In this scenario, phenomena observed in elastic fracture can be seen in transient networks, including a parabolic crack profile and steady crack velocity, as shown in the fracture experiment of complex fluid filaments [7, 96, 97] during extension. Contrarily, a small Z ($Z \ll 1$) indicates that network reconfiguration occurs at the same time scale as crack propagation, which leads to more complicated Trumpet-shaped crack profile and non-steady crack propagation . In our experiment, the maximum value of Z is calculated from experiment as $= 0.12$, implying that the elastic fracture theory cannot be used to describe crack propagation. To address this, we need to look closely at the crack tip region and understand the local processes. A physical picture of this process can be shown by the time sequence of Figure 4.3C-D and explained as follows. When energy is infused to the crack tip, it leads to an

amplification of chain stretch in the tip neighborhood and an increase in rate of bond dynamics. This facilitates the formation of elastic ineffective chains (such as loops shown in Figure 4.3D) as chain reassociation occurs more likely at the stress-free configuration than at a stretched state. This further facilitates the formation of cavities or microcracks within the fracture process zone during propagation. Based on this physical picture, our previous work [103] showed that the crack velocity ($\dot{c}$) – crack tip driving force (G_{tip}) obeyed the following relationship

$$\dot{c} = \begin{cases} \dot{c}_0 \exp\left(\sqrt{\dfrac{G_{\text{tip}}}{\beta}}\right) & G_{\text{tip}} \geq G_0 \\ 0 & G_{\text{tip}} < G_0 \end{cases} \tag{4.4}$$

where $\dot{c}_0 = \alpha \ell_0 k_d^0$ is a characteristic chain velocity that depends on chain length ℓ_0, bond dynamics k_d^0 and its sensitivity α. The parameter β is a characteristic crack driving force that increases with the size of damage zone. In this work, β is set as the fitting parameter since the damage zone size cannot be accurately measured. Physically, Eq. (4.4) suggests that as energy is fed to the crack tip, bonds cannot sustain the stretch and dissociate more frequently, leading to a faster crack propagation. It also provides insight on the effect of the damage zone size where for a larger damage zone (i.e., larger β), more energy is needed to maintain the crack velocity. As discussed in the literature [17, 109-111], the size of damage zone (i.e., the magnitude of β) can be tuned by modifying the microscopic properties of the network, such as varying the bond connectivity, having a higher polydispersity, or increasing the bond sensitivity. To control crack velocity, one may also tune the characteristic parameter $\dot{c}_0$, which changes linearly with bond

sensitivity, chain length and natural bond dissociation rate. To sum up, over the deformation history, one can track the mechanical state of the specimen via Eq. (4.1). Using this information, one can determine the evolution of the crack based on Eqs. (4.3) and (4.4).

4.4.4 Non-steady state fracture of vitrimer

To check whether this model is consistent with experimental observations, we used Eqs. (4.1), (4.3) and (4.4) to predict the stability and the velocity of a crack subjected to our experimental conditions. By matching predictions with experiment measurements on crack extension history (Figure 4.4A and B), we found that our model accurately captured the non-steady extension of the crack by using the fitting parameter $\beta = 4.8\, J/m^2$. We however noticed that the model tended to underpredict the crack velocity c when as it approaches the right boundary of the specimen (this was especially apparent for the case $W_0 = 0.26$). We used finite element simulations and found the discrepancy to be caused by boundary effect when the crack interacted with the free edge, producing complicated stress patterns that are not captured by the analytical model. To inform the experimental design, we then theoretically explore the crack arrest length c_{arrest} under different conditions. Since modifying the molecular properties is out of the scope of this work, we keep the extension parameter Z constant, and tune the crack tip driving force by varying the loading rate (the normalized Weissenberg number $W_0 = \dot{\lambda}/k_d^0$) and the specimen's normalized height $H_0 k_d^0/\dot{c}_0$. By performing large numbers (~ 2000 simulations) of virtual experiments using Eqs. (4.1), (4.3) and (4.4), we summarize our result in a contour map (units in

mm) shown in Figure 4.4C. We see that increasing both the specimen height and loading rate favors crack propagation, as shown by the increase of c_{arrest}. To verify this prediction, we performed additional fracture tests on a specimen of width $50\,mm$ and overlayed contour plots with scatter points representing the experimental results with squares (flow), cross (crack arrest) and circles (rupture). We note that rupture occurs when the crack arrest length is greater than the specimen width. When the cracks were arrested, we experimentally measured their final length as represented by the numbers on top of the crosses in Figure 4.4C. We see that the model accurately captures each regime as well as provides reasonable predictions on the crack arrest length.

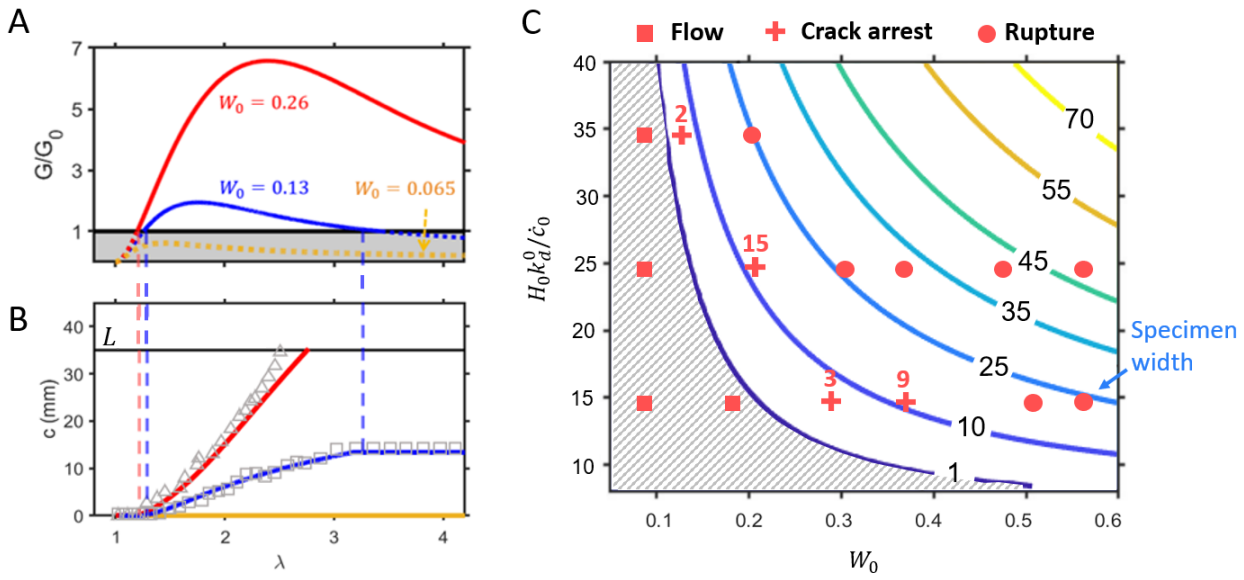

Figure 4.4: Phase map of three characteristic fracture phenomena. A $\mathcal{G} - \lambda$ relation for different loading rates conducted in experiment. **B** Comparison between model prediction (lines) and experimental measurement (scattered symbols) on the evolution of crack length over loading history. **C** A contour map with unit of mm that relates experimental conditions to the three characteristic fracture phenomena (flow, crack arrest and rupture). Scatter points are experimental results for flow (square), crack arrest (cross) and rupture (circle).

Furthermore, while the results of Figure 4.4C are generated under relatively simple loading conditions (constant W_0), one may ask if this quantitative understanding can be used to mitigate or even control fracture using more complicated loading processes. For instance, can we tune the loading history such that the material preserves its mechanical integrity during most of its life? To illustrate this, we designed a pure-shear experiment with the loading pattern (Figure 4.5A), alternates between fast ($W_0 = 0.5$) and slow stretch rates ($W_0 = 0.05$). Our model shows that this oscillatory loading leads to sharp spike and decrease of G_{tip} over time (Figure 4.5B), leading to multiple crack propagation events. Although a crack initiates and propagates rapidly during the fast-loading stage, it decelerates immediately once the loading rate changes and is eventually arrested. Over the course of two cycles, our model shows that the specimen maintains its integrity, although the majority of its deformation is applied during the fast-loading stage. We then performed experiment under the same condition and found that the measurement on crack extension c agrees very well with the semi-analytical model (Figure 4.5C). In addition to crack extension, the change of crack profile also distinguishes the flow and elastic solid response of the specimen. At fast loading, the crack tip advances in a relatively sharp parabolic shape (i and ii), after which it becomes a curved edge after arrest (iii). Notably, during the second loading stage, fracture occurs by the nucleation of a new crack at the curved edge (iv), instead of propagating the arrested one. This phenomenon illustrates well the transient nature of cracks in transient network. When a crack is arrested, its life comes to an end as the singular stress fields around its tip gradually

relax in time. While the detailed profile and its evolution over time cannot be captured by the analytical model, finite element simulation under the same conditions clearly show the “death” of a crack as the energy level decreases, as well as the “birth” of the secondary crack during the second fast loading (Figure 4.5E). Notably, Figure 4.5C shows that finite element (dash line) agrees very well with both the semi-analytical model and experiment on the crack propagation. This again verifies the applicability of the semi-analytical model even when for complicated loading history. From a practical viewpoint, this example illustrates a strategy on fracture control of materials made of transient networks. For instance, in 3D printing applications, this example provides ideas towards a new technique to “program” the fracture of ink during extrusion to achieve very thin filaments. A relevant idea on varying printing resolution by rate control was proposed by Yuk and Zhao [111]. We foresee the capacity of “fracture on demand” will further enrich the design space. In addition, the combined crack propagation and flow may be related to observations in other experimental studies. For instance, in the probe tack experiments of soft adhesives, a micro-defect on the interface may first grows horizontally (fracture) into a microscopic crack, after which it grows vertically (blunting) and leads to cavitation. This crack arrest phenomenon was discussed as an early stage of cavitation failure in adhesives [112, 113].

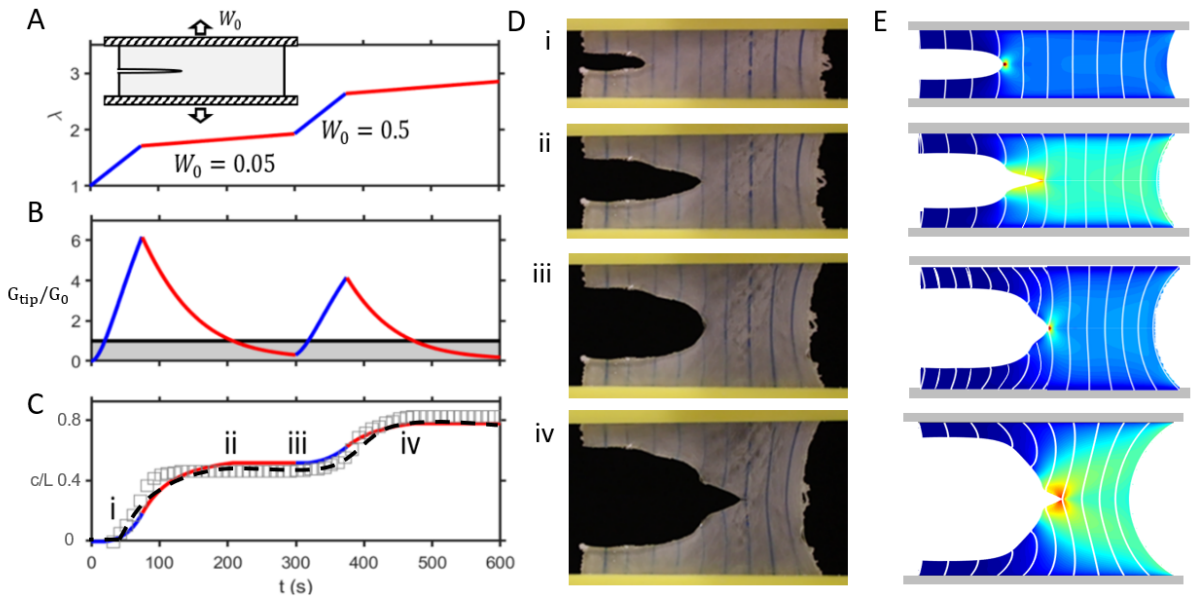

Figure 4.5: Programming of crack propagation. (A) Schematic of experimental geometry and loading history, where the specimen is stretched by two alternating rates. (B) The $\mathcal{G} - \lambda$ path of the specimen during loading, we see that the path enters and leaves crack propagation regime repeatedly. (C)The crack speed $\dot{c}$ as a function of deformation λ. The red-blue line is analytical model prediction, scatter square is experimental measurement and black dash line is FEM prediction. (D)&(E) Snapshots of experiments (D) and FEM simulation (E) taken at three time frames in experiment.

4.3 Conclusion

We have identified a peculiar form of fracture that occurs in polymer networks formed by transient crosslinks in which a propagating crack evolves in a highly non-steady manner. As a result, the specimen can continue to deform without catastrophic rupture at low loading rate. We identified that such phenomenon originates form the nonequilibrium nature of the network, where it constantly reconfigures and dissipates energy. To understand the physical laws behind this process, we combined the rate-dependent crack tip driving force G_{tip} and the local network

damage near the crack tip, and identified two parameters that govern this problem. The nominal Weissenberg number W_0 that controls the onset of crack propagation and arrest, and the propagation parameter $Z = \frac{\dot{c}}{L} k_d^0$ that provides information about how far a crack can extend during propagation. Between these two parameters, the former can be controlled by varying experimental condition (loading rate and specimen height), while the latter can be tuned by the molecular structure of the polymer. We further showed how one may control the life of cracks by simply varying the loading condition.

In summary, this work enriches the field of quasi-brittle fracture by introducing a new way of analyzing the fracture in nonequilibrium systems. This opens the door to the prediction and control of non-steady fracture of transient networks that are crucial in engineering applications and scientific research. For instance, some of the example problems explored in this paper can be related to the combined fracture and cavitation of adhesives [112, 114], the blunting-advancing of cracks in physical crosslinked polymers [115] and the fracture-flow transition of transient fluids made of associated polymers [98]. Application-wise, this model can be used to provide control guidance on the material extrusion in additive manufacturing [111], polymer coating [116] and rheological regulating [117]. Due to the simplicity of this model, one may even be able to use it for real time experimental optimization. As a first attempt, this model employs coarse-grained approximations on both the macroscopic stress field and the crack tip damage profile. Therefore, the applicability of this model remains in small to moderate deformation with a small damage zone

compared to specimen size. For ductile fracture (i.e., damage zone is comparable to specimen size), more complicated damage mechanisms, including cavitation, fibrillation become non-negligible, where discrete modeling approaches may be supplemental to understand the damage kinetics of these processes.

Chapter 4, in full, is currently being under review, “Non-steady fracture of transient networks: the case of vitrimer”, by Tong Shen, Zhaoqiang Song, Shengqiang Cai and Franck Vernerey. The dissertation author was the primary investigator and co-first author of this paper.

Chapter 5 Fracture Modes and Hybrid Toughening Mechanisms in Oscillated/Twisted Plywood Structure

5.1 Introduction

Fiber-reinforced composites can be widely seen in nature and diverse engineering applications. In most engineering applications, unidirectional and cross-ply fiber-reinforced composites have been adopted to achieve high tensile, compressive and torsional strengths and stiffnesses [118]. However, in many biological composites, the orientation of reinforced fibers in the matrix changes continuously, forming so-called plywood structure or Bouligand structure. Such fiber alignment can be found in exoskeleton of crabs [119], claws of lobsters [120], bone of mammals [121], exoskeleton of beetles [122], and dactyl club of mantis shrimps [123] as shown in Figure 5.1, though the compositions of the fiber and the matrix vary for those different biomaterials. Recent studies have shown that the fiber-reinforced composites with plywood structure may lead to superior mechanical properties, including extraordinarily high impact resistance [24] and fracture toughness [25, 27, 119].

To understand the significant enhancement of the mechanical properties of a composite with plywood structure, several mechanics models have been recently proposed [25, 27, 28]. In most of the previous studies, crack deflection has been regarded as the main toughening mechanism of a composite with twisted plywood structure [27, 28, 123, 124]. Based on the

principle of maximizing the motive force of the crack [125], a crack in twisted plywood structure usually propagates between layers with the crack front parallel to the fibers and gradually deflects from the initial crack plane, if the fracture toughness of the interface between fiber and matrix is much smaller than that of the fibers [27]. Because of the twisted and enlarged crack surface, it has been shown that the fracture toughness of the composite can be greatly enhanced [27, 69, 124]. More detailed studies have found that the fracture toughness of those materials can be affected by the pitch angle, defined as the rotational angle of two adjacent twisted plywood layers [25, 27]. For example, Fischer et al. [25] treated the twisted plywood structure as an isotropic material with periodically varied elastic properties, resulting in spatial variation of the driving force for the crack propagation. Such variation can also increase the effective fracture toughness of the materials. Some recent experimental studies have further confirmed [120, 122, 126] that the magnitude of pitch angle plays an important role in determining the energy absorption before catastrophic failure of the composite.

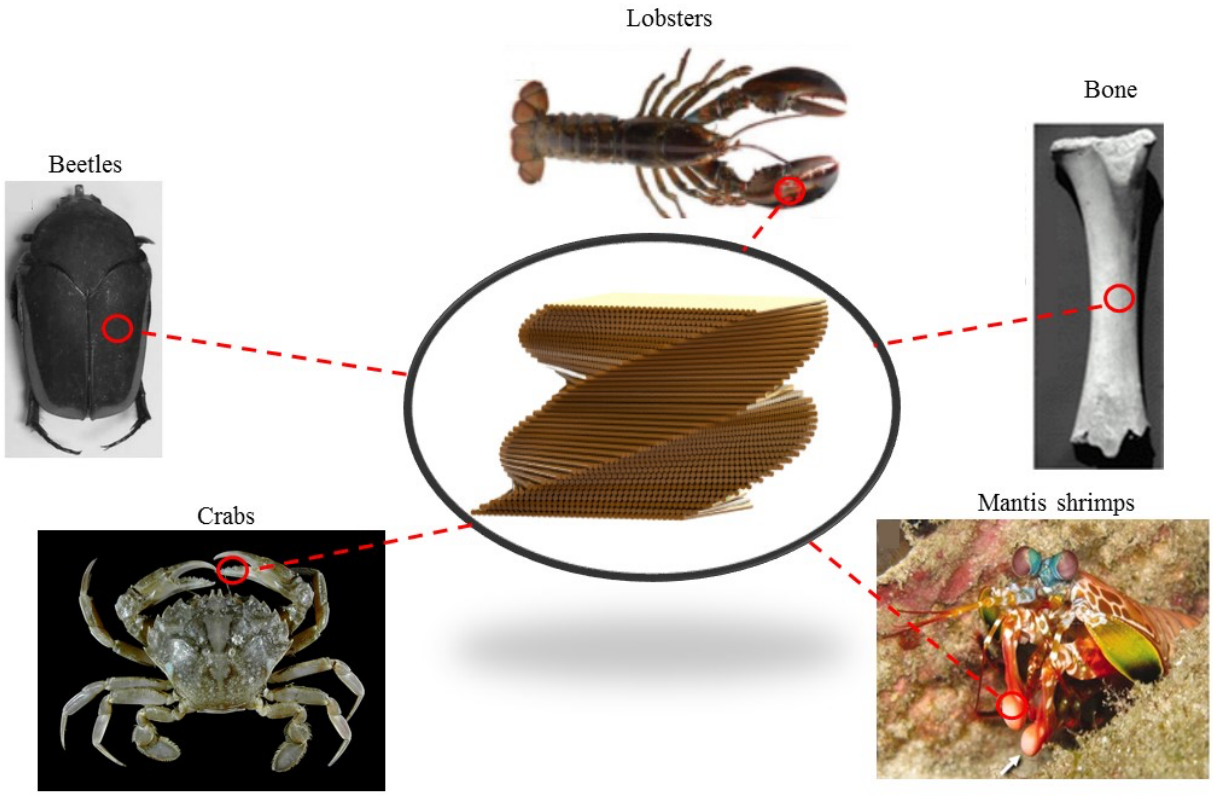

Figure 5.1: Twisted or oscillated plywood structure in biological materials. Twisted or oscillated plywood structure can be found in exoskeleton of beetles [122], claw of lobsters [120], bone of mammals [121], claw of crabs [119] and dactyl club of mantis shrimps [123].

However, all the previous studies provide little insight into the optimized pitch angle for maximizing the fracture energy of the composite. Whereas, it has been found that the pitch angle in beetle exocuticle always falls in a narrow range: 12-18° [122]. Recent experiments have also shown that the fracture toughness of a biomimetic twisted plywood composite constructed by hydroxyapatite mineral microfibers and sodium alginate, reaches a maximal value with the pitch angel around 10° [127].

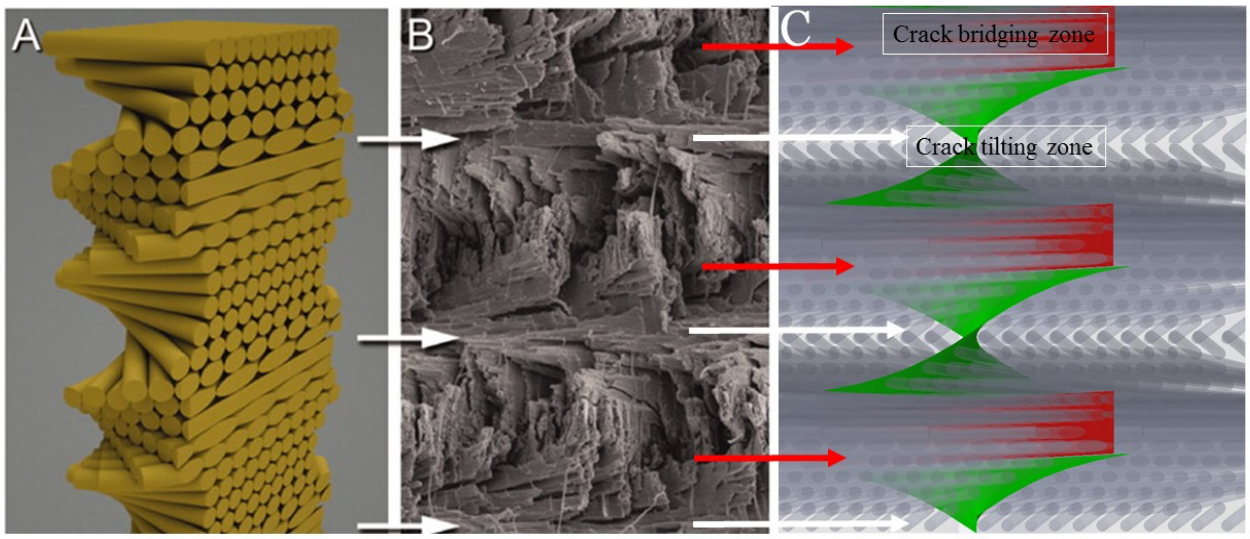

Figure 5.2: The crack propagation in a twisted plywood structure. (A) The schematic of twisted plywood structure [123]; (B) An SEM fractography in stomatopod dactyl club [123]; (C) Schematic of two fracture modes (crack tilting zone with green color and crack bridging zone with red color) in the twisted plywood structure.

It has been known that for a fiber-reinforced composite, during its fracture, a crack usually propagates either along the interface between the fiber and matrix (named as crack tilting) or in the matrix across the fibers (named as crack bridging), both of which can result in the increase of the effective fracture toughness of the material. In this article, we try to reveal that a combination of both crack tilting and crack bridging determines the effective fracture toughness of the composite with a twisted plywood structure (Figure 5.2 and Figure 5.3) or an oscillated plywood structure. During the fracturing process, a crack plane in the composite may first propagate following the twisted fiber orientation till the local energy release rate drops below a value (a purely geometrical consequence), which is too small to drive the crack to further propagate along the fiber-matrix interface. As a consequence, the crack propagates into the matrix crossing the fibers, conventionally termed as crack bridging (as shown in Figure 5.3). Based on our modelling,

we find out that with certain material properties, the effective fracture toughness of the composite is maximized for a certain pitch angle of the twisted plywood structure, which agrees well with the measurements in previous experiments [122]. We hope the model developed in the article will be useful for designing fiber-reinforced composites with tailorable mechanical properties.

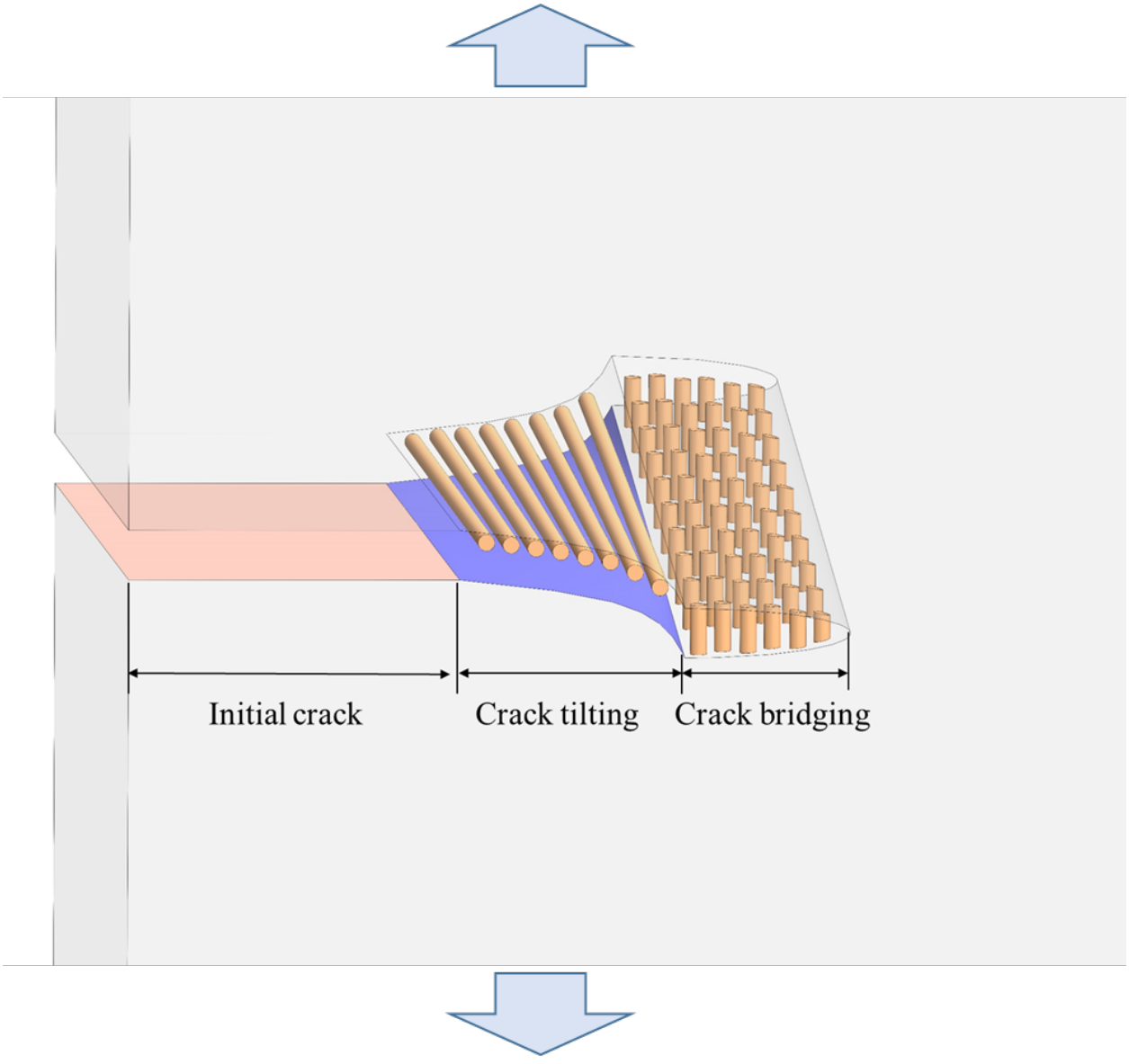

Figure 5.3: A 3D schematic of fractography in twisted plywood structure. Three fracture zones are defined in the schematic: initial crack zone (pink), crack tilting zone and crack bridging zone. In the figure, only the fibers near the crack surface are shown, and all the other fibers are hidden.

5.2 Results and discussion

In our model, we make the following assumptions to simplify the analysis. For the modelling of crack tilting, we assume that fibers and matrix have the same elastic properties including elastic modulus and Poisson's ratio [69], and the model is based on linear elastic fracture mechanics with only mode I loading as shown in Figure 5.3. The solution used in the paper is accurate to the first order [128]. A few more assumptions are then adopted in the modelling of crack bridging. First, the crack bridging occurs in the composite where the fibers are nearly parallel to the loading direction, and the toughening factor of crack bridging is a constant and independent of pitch angle. Second, the crack propagation direction in crack bridging zone is parallel to the initial crack plane. Additionally, to predict the effective fracture toughness, in oscillated plywood structure, we assume the crack bridging zone continuously connects two crack tilting zones. In twisted plywood structure, we assume the crack will propagate from the crack bridging zone to the tilting zone discontinuously. The criterion for determining the crack propagation path is given by the maximization of local energy release rate [129].

5.2.1 Model of crack tilting

We first review the approach proposed by Faber and Evans [69] for modelling crack tilting, taking into consideration a modification made by N. Suksangpanya et al. [27] later on. The increase in the fracture toughness caused by crack deflection can be evaluated from local stress intensity factors at the tilted and twisted portions of crack front. The local stress intensity factors, k_1', k_2'

and k_3', are assumed to be functions of the deflection angles as shown in Figure 5.4. The crack is represented as a rotated flat plane with a straight crack front. Based on the results of B. Cotterell and J. Rice [128], the local stress intensity factors are then obtained by transforming the local stress field of kinked crack with tilted angle α onto the twisted plane by a twisted angle of ϕ, namely [27, 69]:

$$\begin{aligned} k_1'/K_I^0 &= \cos^2\left(\frac{\alpha}{2}\right)\left\{2\nu\sin^2\phi+\cos^2\left(\frac{\alpha}{2}\right)\cos^2\phi\left[1+2\sin^2\left(\frac{\alpha}{2}\right)\right]\right\} \\ k_2'/K_I^0 &= -2\sin^3\left(\frac{\alpha}{2}\right)\cos^3\left(\frac{\alpha}{2}\right)\cos\phi \\ k_3'/K_I^0 &= -\cos^2\left(\frac{\alpha}{2}\right)\sin\phi\cos\phi\left\{2\nu-\cos^2\left(\frac{\alpha}{2}\right)\left[1+2\sin^2\left(\frac{\alpha}{2}\right)\right]\right\} \end{aligned}, \tag{5.1}$$

where K_I^0 is the global applied stress intensity factor of mode I fracture, ν is Poisson's ratio of the materials (we set $\nu = 0.3$ for later calculation), and the twisted angle ϕ and tilted angle α can be rewritten as [27]

$$\begin{aligned} \phi &= \bar{X}\gamma \\ \alpha &= \tan^{-1}\left(\frac{\bar{Y}}{\bar{X}}\tan\left(\bar{X}\gamma\right)\right), \end{aligned} \tag{5.2}$$

where the dimensionless coordinates are given by $\bar{X} = X/d, \bar{Y} = Y/d, \bar{Z} = Z/d$, and d is the fiber diameter; γ is pitch angle.

The advancement of the tilted crack is assumed to be governed by the local energy release rate G_{tilt}, which can be calculated based on the local stress intensity factor k_1', k_2', and k_1' [69], namely,

$$G_{tilt} = \frac{1}{E}\left[k_1'^2\left(1-\nu^2\right)+k_2'^2\left(1-\nu^2\right)+k_3'^2\left(1+\nu\right)\right], \tag{5.3}$$

where E is Young's modulus of the composite. The critical value of local energy release rate G_{tilt} for steady-state crack propagation is the intrinsic fracture energy Γ_{int} which is taken as a material constant reflecting the energy dissipated by the breakage of matrix material to form a void ahead of the crack tip. The normalized local energy release rate with crack titling is defined as $\bar{G}_{tilt} = G_{tilt}/G_0$, where $G_0 = \left(1-\nu^2\right)\left(K_I^0\right)^2/E$ is global energy release rate. Without considering the toughening mechanism of crack tilting ($\alpha = 0, \phi = 0$), the local energy release rate G_{tilt} is equal to the gobal energy release rate G_0. Thus, the critical energy release rate G^c is equal to intrinsic fracture energy Γ_{int} for steady-state crack propagation. If considering the crack tilting and steady-state crack propagation, local energy release rate G_{tilt} must equal the intrinsic fracture energy Γ_{int}, and the global energy release rate measured from experiments is the fracture toughness of the composite with crack tilting, $G_{tilt}^c = \Gamma_{\text{int}}/\bar{G}_{tilt}$.

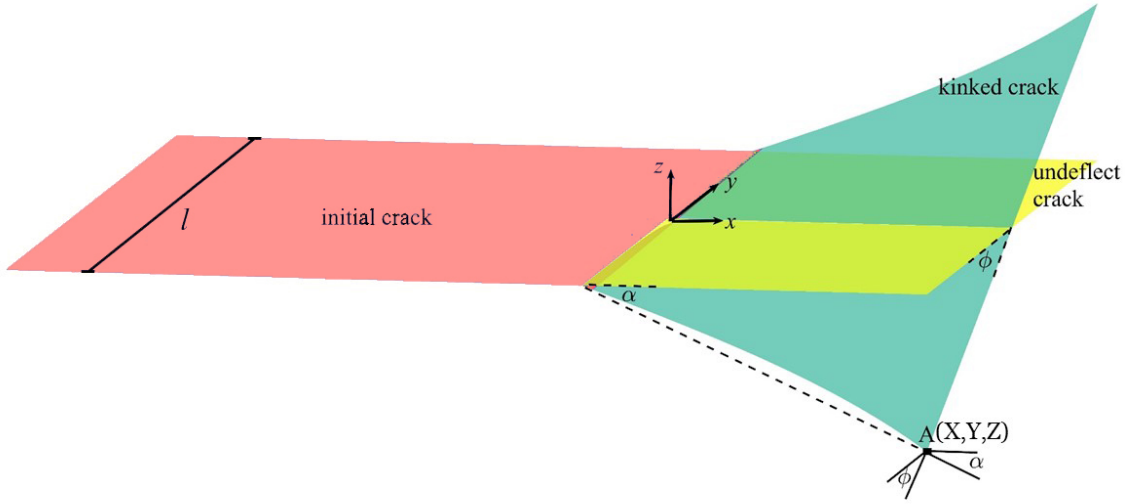

Figure 5.4: The model of the crack tilting defined by Faber and Evans [13]. The kinked crack is represent by a twisting surface with the tilted angle α and twisted angle of ϕ and the angles are mathematically defined by Eq. (5.2).

A combination of Eqs. (5.1)-(5.3) allows us to compute the local energy release rate G_{tilt} at each point with the coordinate $\left(\bar{X},\bar{Y}\right)$ as shown in Figure 5.4. The tilted crack shape in one period can be described by

$$\bar{Z}=\bar{Y}\tan\left(\bar{X}\gamma\right),0\le\bar{X}\le\pi/\gamma,-\bar{l}/2\le\bar{Y}\le\bar{l}/2, \tag{5.4}$$

for twisted plywood structure, and

$$\bar{Z}=\bar{Y}\tan\left(\frac{\pi}{2}-\left|\frac{\pi}{2}-\bar{X}\gamma\right|\right),0\le\bar{X}\le\pi/\gamma,-\bar{l}/2\le\bar{Y}\le\bar{l}/2, \tag{5.5}$$

for oscillated plywood structure, where $\bar{l}=l/d$ is dimensionless fiber length. The crack shape and its corresponding local energy release rate of oscillated and twisted plywood structure is shown in Figure 5.5A-B, respectively.

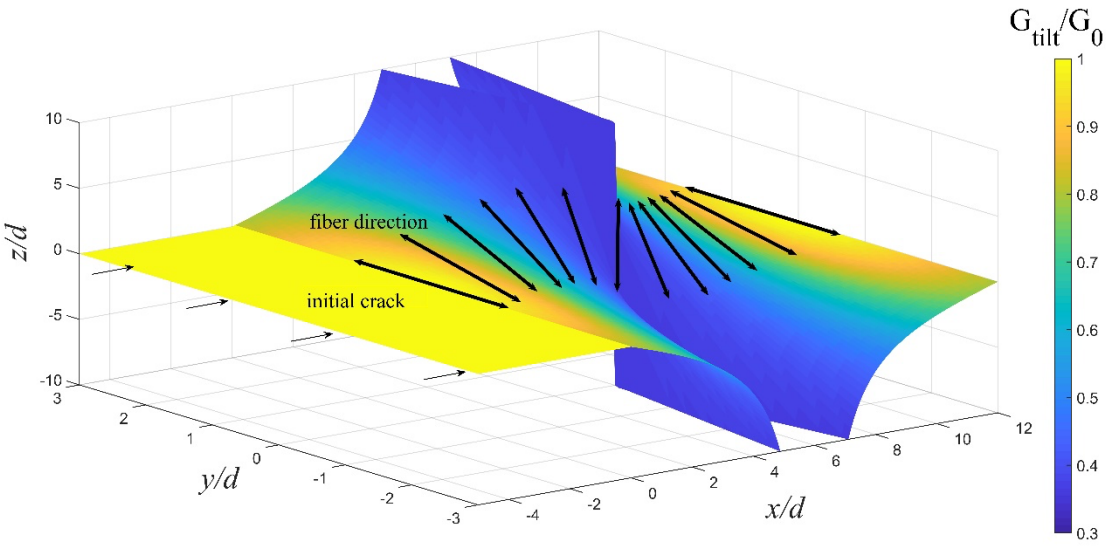

A

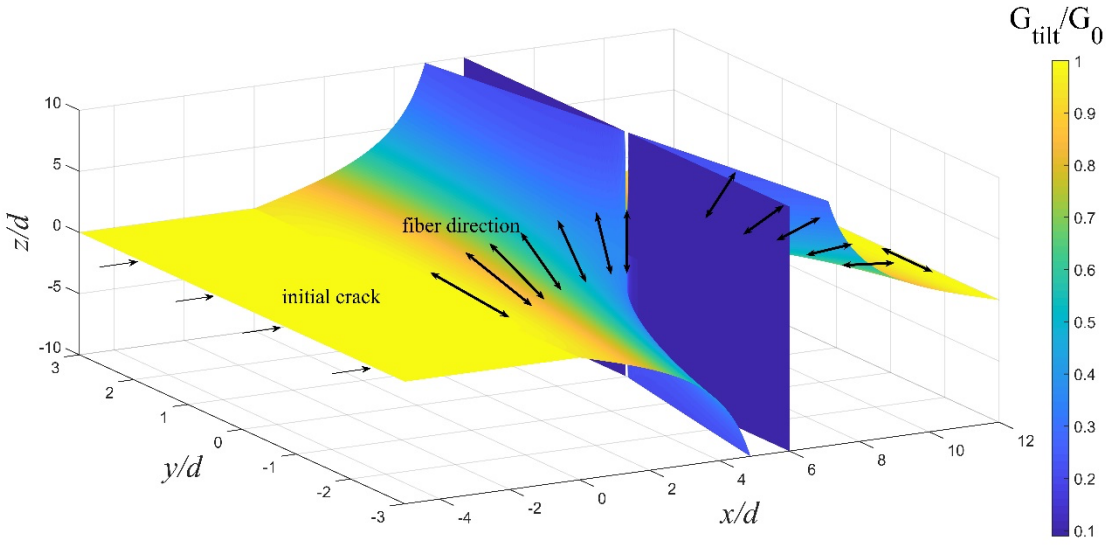

B

Figure 5.5: The shape of crack surface and local energy release rate as the crack propagates along fibers. A oscillated plywood structure; **B** twisted plywood structure. The pitch angle is $\gamma = 15^{o}$. Double-headed arrows represent the fiber direction and dashed single-headed arrows represent the propagation direction of initial crack. The color represents the value of local energy release rate. The line of x=0 is boundary of initial crack and propagated crack.

In oscillated plywood structure shown in Figure 5.5A, the oscillated angle ranges from $0°$ to $90°$. The energy release rate dramatically decreases as the crack is significantly titled toward the direction parallel to the loading direction. Similar result is shown in twisted plywood structure in Figure 5.5B. The decrease of local energy release rate and the increase of twisting of crack surface could both increase the effective fracture toughness of the composite.

5.2.2 Model of crack bridging

When the crack surface is tilted to the direction almost parallel to the loading direction, its local energy release rate can reduce dramatically as shown in Figure 5.5 calculated by Eq. (5.3), which may not be large enough to drive further crack propagation along the twisted fiber alignment. Instead, the crack can propagate perpendicular to the loading direction and cross the fibers to form crack bridging or branching [28]. To simplify the analysis, in the model, we only consider crack bridging. As a matter of fact, experimental investigations showed that the main toughening mechanisms are crack tilting and crack bridging in many plywood structures, such as claws of lobsters [130], exoskeleton of beetles [131], dactyl club of mantis shrimps [123], scales of fishes [132] and cellulose nanocrystal (CNC) composites [126].

We adopted a two-dimensional discontinuous crack bridging model developed by S. Yue et al [133, 134]. In steady-state crack propagation, if neglecting any toughening mechanisms (e.g. crack bridging), the global stress intensity factor K_I^0 is equal to the intrinsic fracture toughness K_I^{int} (fracture toughness of matrix material), i.e. $K_I^0 = K_I^{\text{int}}$. Otherwise, with considering the

crack bridging (shown in Figure 5.6), the fracture toughness of the composite K_I^0 measured from most experiments can be written as,

$$K_I^0 = K_I^{\text{int}} + K_I^b, \tag{5.6}$$

where K_I^b is the stress intensity factor for crack bridging which denotes the stress intensity factor induced by the bridging forces from the fibers, which is calculated by [133, 135, 136],

$$K_I^b = \sqrt{\frac{2}{\pi}} \int_0^{l_{br}} \frac{\sigma_{br}(x)}{\sqrt{l_{br} - x}} dx, \tag{5.7}$$

in which l_{br} is crack bridging length and σ_{br} is the normal stress of crack bridging. Here, we assume the fibers distribute in densest packing in 2D, as shown in Figure 5.6. The distance between neighboring fibers is d_0. As a result, the bridging length is

$$l_{br} = \frac{N}{2} d_0, \tag{5.8}$$

where *N* is the number of the discrete bridging forces in crack bridging zone.

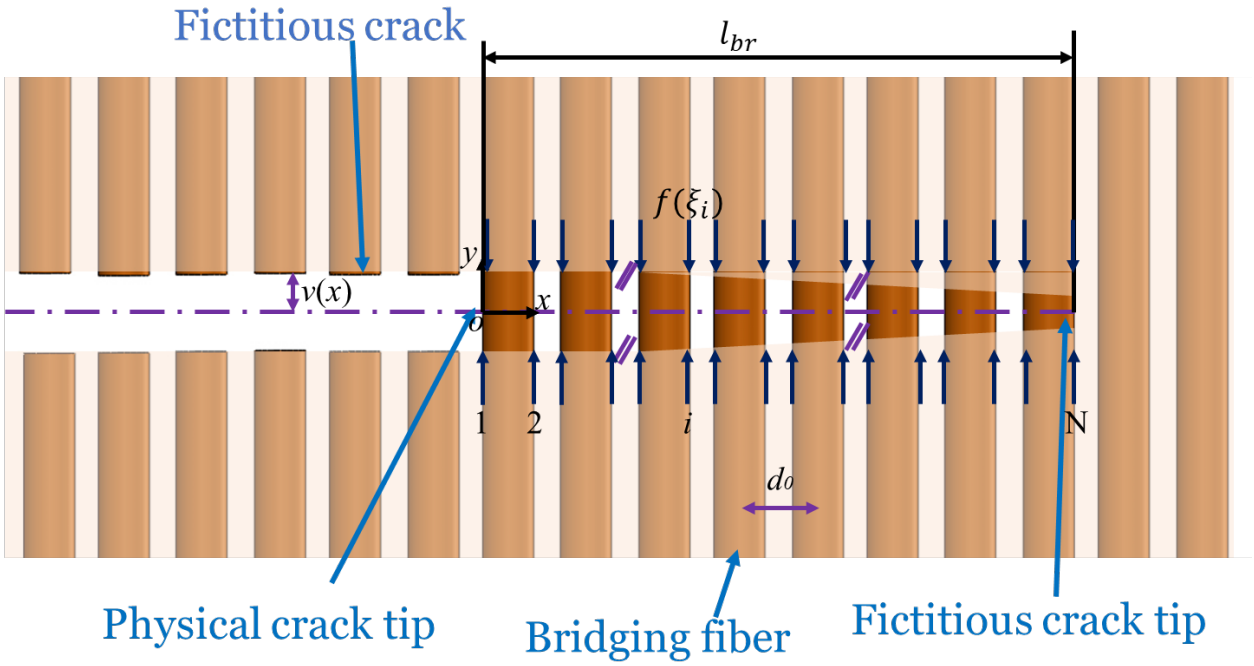

Figure 5.6: Schematic of 2D discontinuous crack bridging. l_{br} presents the bridging length, ξ_i presents the location of i, $v(x)$ presents the crack opening displacement, and $f(\xi_i)$ presents the discretized concentrated force in crack bridging zone.

The toughening ratio at the stage of steady-state crack propagation due to the bridging traction is calculated by Yue S. et al. [133] as

$$\eta_{SS} = \frac{K_I^b}{K_I^{\text{int}}}, \tag{5.9}$$

which is a function of fiber length l, volume fraction of fiber V_f, modulus of fiber E, fiber diameter d, interfacial strength τ_m, and fracture toughness of fiber K_{Ic}^{fiber}, estimated by Meng et al. [137],

$$\eta_{SS} = f(\Phi) = 7.6 - 7.1\exp\left(-\frac{\Phi}{68.25}\right), \tag{5.10}$$

where the dimensionless parameter is:

$$\Phi = \frac{V_f \tau_m E l^2}{\left(K_{Ic}^{fiber}\right)^2 d}. \tag{5.11}$$

The critical energy release rate with crack bridging is $G_{br}^{c} = \left(1+\eta_{SS}\right)^2 \Gamma_{\text{int}}$ [133, 137], where Γ_{int} is the intrinsic fracture energy.

The local stress intensify factor is equal to the intrinsic fracture toughness in the case of steady-state crack propagation. Based on Eqs. (5.6) and (5.9), the local energy release rate with crack bridging for steady-state crack propagation could be given by,

$$G_{br} = \frac{\left(1-\nu^2\right)\left(K_I^{\text{int}}\right)^2}{E} = \frac{1}{\left(1+\eta_{SS}\right)^2} G_0, \tag{5.12}$$

where $G_0 = \left(1-\nu^2\right)\left(K_I^0\right)^2 / E$ is the energy release rate determined by the remote loading.

5.2.3 Transition from crack tilting to crack bridging

We assume that if the local energy release rate for a crack propagating along the tilted path given by Eq. (5.3) is lower than the local energy release rate for crack bridging given by Eq. (5.12), crack bridging happens. Based on this assumption, the local energy release rate in a plywood structure can be calculated as $G = \max\left(G_{tilt}, G_{br}\right)$. Therefore, the shape of the crack plane can be determined by comparing the magnitude of the local energy release rate along the tilted path and the local energy release rate in the matrix with crack bridging. In the following calculations, we consider two cases with $G_{br}/G_0 = 0.2$ and $G_{br}/G_0 = 0.4$, corresponding to $\eta_{SS} = 0.581$ and $\eta_{SS} = 1.236$ in Eq. (5.12), respectively. As shown in the later session, $G_{br}/G_0 = 0.2$ is indeed very

close to the value for exoskeleton of beetles and the fabricated cellulose nanocrystal (CNC) composites.

In Figure 5.7, the crack propagates along fibers at the beginning, because the initial crack plane is perpendicular to the loading direction and the energy release rate is large for crack tilting, compared to the crack bridging. With the increase of tilting angle of crack plane, the energy release rate decreases. When the local energy release rate of crack tilting is smaller than that of crack bridging, the crack propagates across the fibers, forming crack bridging zone. With the further growth of the crack plane, the fracture mode goes back to crack tilting if the local energy release rate of crack bridging is smaller than that of crack tilting. With the increase of the local energy release rate for crack bridging, the area of crack bridging zone shrinks as shown in Figure 5.7 (A) and (B).

Similarly, the crack path selection in twisted plywood structure is also determined by maximizing the local energy release rate. However, the connection between crack tilting and crack bridging is discontinuous as shown in Figure 5.8 (A) and (B). In the following analysis, we ignored the effect of such discontinuous transition, which may actually cause additional energy dissipation.

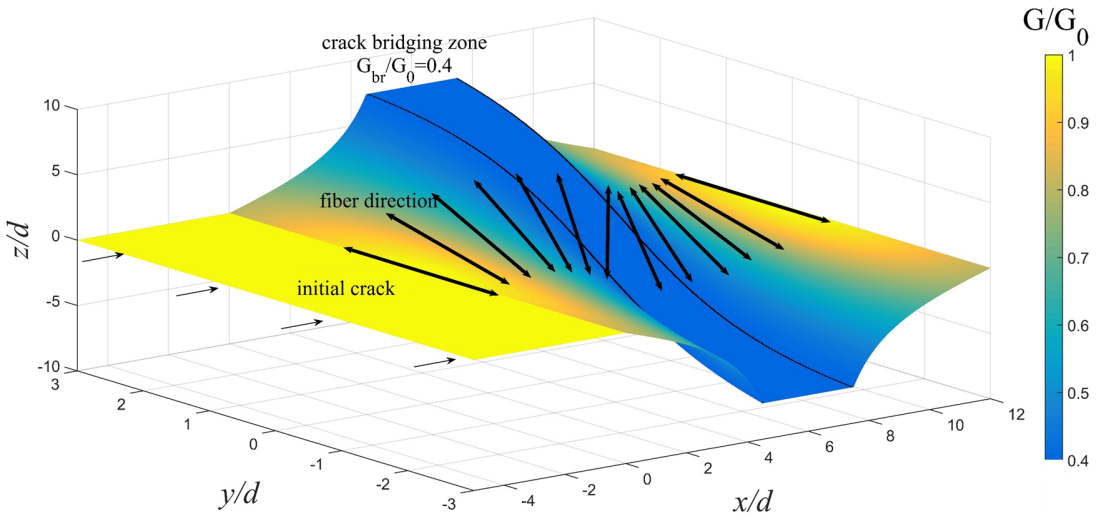

A

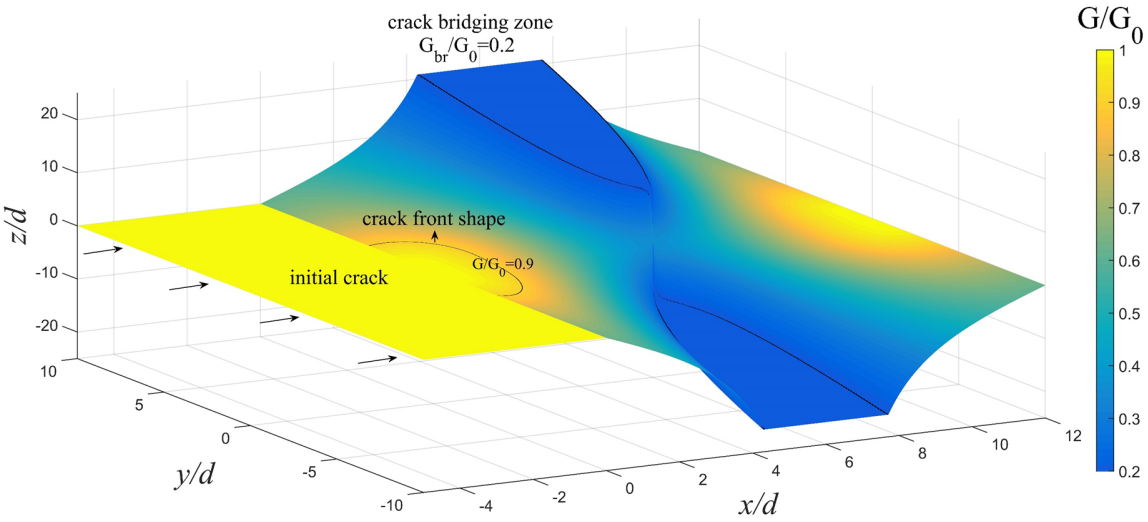

B

Figure 5.7: The shape of crack surface and local energy release rate in oscillated plywood structure. The shape of crack surface and local energy release rate as the crack propagates along fibers and across fibers in oscillated plywood structure with different critical energy release rate of crack bridging. **A** $G_{br}/G_0 = 0.4$ and **B** $G_{br}/G_0 = 0.2$. The pitch angle is $\gamma = 15°$. Black line of $G_{br}/G_0 = 0.4$ and $G_{br}/G_0 = 0.2$ in figure A and figure B, respectively, is the boundary between crack tilting zone and crack bridging zone. The crack front could be curved by contour line of local energy release rate (e.g. $G/G_0 = 0.9$) in figure B.

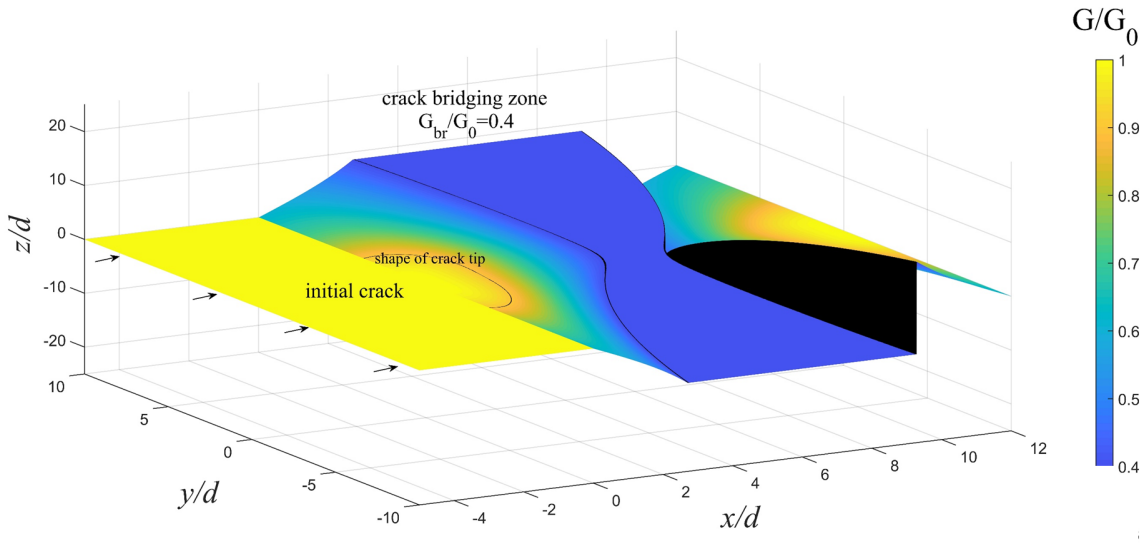

A

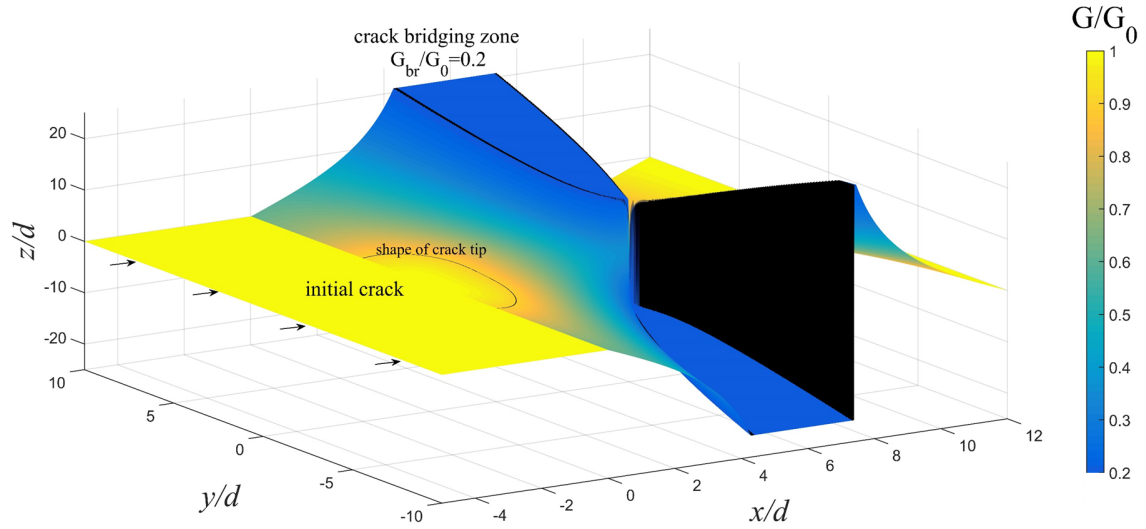

B

Figure 5.8: The shape of crack surface and local energy release rate in twisted plywood structure. The shape of crack surface and local energy release rate as the crack propagates along fibers and across fibers in twisted plywood structure with different critical energy release rate of crack bridging. **A** $G_{br}/G_0 = 0.4$ and **B** $G_{br}/G_0 = 0.2$. The pitch angle is $\gamma = 15°$. The black line is the boundary between the crack tilting zone and crack bridging zone.

5.2.4 Effective fracture energy of the composite with oscillated or twisted plywood structure

We have calculated the crack shape and local energy release rate of oscillated plywood structure and twisted plywood structure in sessions 5.2.1 and 5.2.2. Considering both the crack shape and local energy release rate, the normalized fracture energy with respect to the area of the undeflected crack plane can be given by [69],

$$\frac{\Gamma_{\text{int}}}{G_{eff}^{c}} = \frac{1}{S_0}\int_{A_0}\frac{G}{G_0}\cos\beta dS_0 = \frac{\gamma}{\pi\bar{l}}\int_{-0.5\bar{l}}^{0.5\bar{l}}\int_{0}^{\pi/\gamma}\frac{G}{G_0}\cos\beta dxdy, \tag{5.13}$$

where $S_0 = \int_S \cos\beta dS$ is the area of undeflected crack plane (e.g. yellow plane shown in Figure 5.4), S is the area of deflected crack plane (e.g. green plane shown in Figure 5.4), G_{eff}^{c} is the effective fracture energy and β is the kinking angle between the normal to the deflected crack plane and the normal to the undeflected crack plane. So, the dimensionless effective fracture energy is

$$\bar{G}_{eff}^{c} = \frac{\pi}{\gamma}\frac{\bar{l}}{\int_{-0.5\bar{l}}^{0.5\bar{l}}\int_{0}^{\pi/\gamma}\frac{G}{G_0}\cos\beta dxdy}, \tag{5.14}$$

where $\bar{G}_{eff}^{c} = G_{eff}^{c}/\Gamma_{\text{int}}$.

The dimensionless effective fracture energy of the composite depends on the length of fibers, pitch angle, and fracture energy of crack bridging. In the discussion section, we will fix the fracture energy of the crack bridging zone to investigate the effects of fiber length and pitch angle on the effective fracture energy of the composite.

5.2.5 Optimized pitch angle in biological materials

The results obtained in the previous section are in dimensionless forms, so they are generic. In this section, we plug real dimensional numbers measured from the exoskeleton of beetles [122] and cellulose nanocrystal (CNC) composites [126] into the dimensionless equations obtained in the previous section. Therefore, we can compare the predictions of our theory to real experiments.

Table 5.1 shows the parameters of two types of nanofibers: chitin-protein fibers which can be found in many biomaterials such as exoskeleton of beetles, and cellulose nanocrystal (CNC) fibers which widely exist in wood, tunicate, et al.

Table 5.1: Parameters of chitin-protein fibers in exoskeleton of beetles and cellulose nan0crystal fibers.

	chitin-protein fibers	cellulose nanocrystal fibers
Length l (μm)	~1 [138]	~1 [126]
Diameter d (nm)	20 [122, 138]	10 [126]
Modulus E (GPa)	8 [139]	120 [126]
Strength σ_m (MPa)	200 [139]	1000 [140]
Interfacial strength τ_m (MPa)	10	20
Volumetric fraction in composite V_f	0.5	0.5
Fracture toughness $K_{Ic}^{fiber}(MPa \cdot m^{1/2})$	2 [20]	10 [141]

As the parameters of chitin-protein fibers in exoskeleton of beetles listed in table 1, the length is around 1 μm [139], the diameter is 20 nm [122, 139], the modulus is 8 GPa [138], the strength is 140 MPa [138], and the fracture toughness is 2 $MPa \cdot m^{1/2}$ [20]. We estimate the volumetric fraction of the fiber in composite is 0.5 and interfacial strength between chitin-protein fibers and matrix material is 10 MPa. According to Eq. (5.11), the corresponding dimensionless parameter is $\Phi = 0.5$. The steady-state toughening ratio for crack bridging calculated by Eq. (5.10) is $\eta_{SS} \approx 0.55$. Substituting these parameters into Eq. (5.12), we can get fracture energy of crack bridging of exoskeleton of beetles: $\bar{G}_{br}^{c} = G_{br}^{c} / \Gamma_{\text{int}} = 2.41$.

Recently, cellulose nanocrystal (CNC) composites with twisted plywood structure have been synthesized by J. W. Gilman et al [126]. As the parameters of CNC fibers listed in Table 5.1, the length is around 1 μm, the diameter is 10 nm, the modulus is 120 GPa, the strength is 1 GPa, and the fracture toughness is 10 $MPa \cdot m^{1/2}$. We estimate the volumetric fraction in composite is also around 0.5 and the interfacial strength between CNC fibers and matrix material is 20 MPa. According to Eq. (5.11), the corresponding dimensionless parameter is $\Phi = 1.2$. The steady-state toughening ratio for crack bridging calculated by Eq. (5.10) is $\eta_{ss} \approx 0.62$. Substituting the parameters into Eq. (5.12), we can get the fracture energy of crack bridging of CNC composites to be around $\bar{G}_{br}^{c} = 2.62$.

As shown above, the dimensionless fracture energies of crack bridging for exoskeleton of beetles containing chitin-protein fibers ($\bar{G}_{br}^{c} = 2.41$) and the synthesized composite containing

cellulose nanocrystal fibers ($\bar{G}_{br}^{c} = 2.62$) are close, though the dimensionless fiber lengths are quite different for these two fibers, $\bar{l} = 50$ for chitin-protein fibers and $\bar{l} = 100$ for cellulose nanocrystal fibers. In order to investigate the length effect of fibers on effective fracture energy, we choose a unique value ($\bar{G}_{br}^{c} = 2.5$) for chitin-protein fibers and CNC fibers. We first study the effective fracture energy of the plywood structure as a function of dimensionless fiber length with different pitch angles in Figure 5.9. If we fix the fracture energy of crack bridging ($\bar{G}_{br}^{c} = 2.5$) and pitch angle (e.g. $\gamma = 15°$) in Figure 5.9, there is an optimal fiber length, $\bar{l} = 50$, to achieve the maximal effective fracture energy. If fiber length departs from the optimal value, the effective fracture energy drops rapidly. With the increase of pitch angles in Figure 5.9, the optimal fiber length decreases. The peak value of effective fracture energy in Figure 5.9 is about $\bar{G}_{eff}^{c} = 3.5$, which is significantly larger than the fracture energy of the composite with only crack bridging $\bar{G}_{br}^{c} = 2.5$. It has been measured in the experiments that the pitch angle in exoskeleton of beetles ranged from $12°$ to $18°$ with the dimensionless fiber length $\bar{l} = 50$ [122], which agrees well with our computation as shown in Figure 5.9.

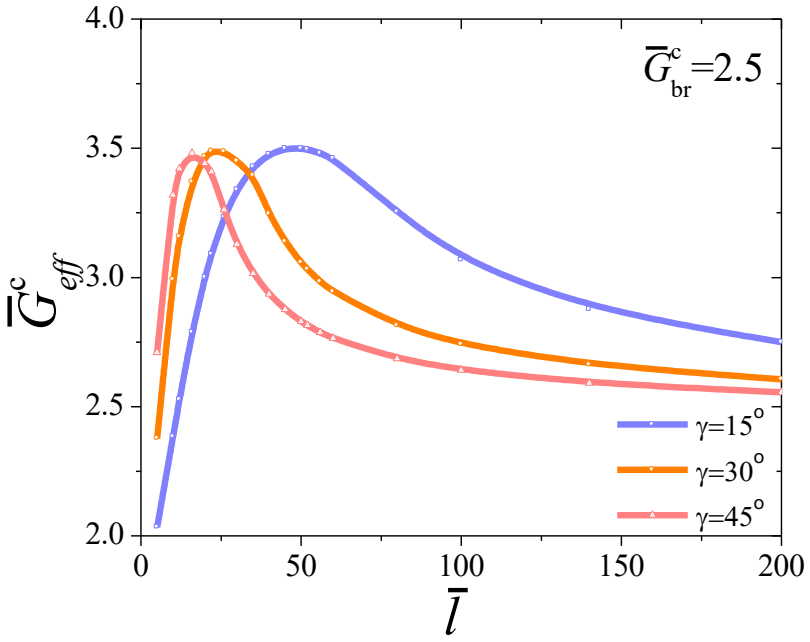

Figure 5.9: The effective fracture energy of oscillated/twisted plywood structure as a function of fiber lengths. The effective fracture energy of oscillated/twisted plywood structure as a function of different dimensionless fiber length with different pitch angle γ in consideration of the fracture energy of crack bridging $\bar{G}^c_{br} = 2.5$.

We next consider the chitin-protein fiber-reinforced composite of exoskeleton of beetles [122], in which the fracture energy of crack bridging is around $\bar{G}^c_{br} = 2.5$. As observed in the experiments, the pitch angle of twisted plywood structure is around $12° \sim 18°$ in the exoskeleton of beetles. Figure 5.10 plots the effective fracture energy against the pitch angle with $\bar{G}^c_{br} = 2.5$. For chitin-protein fibers of the exoskeleton of beetles, the fiber length is around $\bar{l} = 50$, and thus the optimized pitch angle for the largest fracture energy is $15°$, which also agrees with the experimental measurements.

The toughness of CNC composites is also measured as a function of pitch angle in the experiments [126]. The largest toughness is 1.01 $MPa \cdot m^{-3}$, when the pitch angle of plies in

CNC composites is 9.7°. As shown in Table 5.1, the dimensionless fiber length for the CNC composites is around 100. Figure 5.10 shows that, the largest fracture energy is achieved for the composite when the pitch angle is $\gamma = 8°$, which also agrees reasonably well with the experimental measurements.

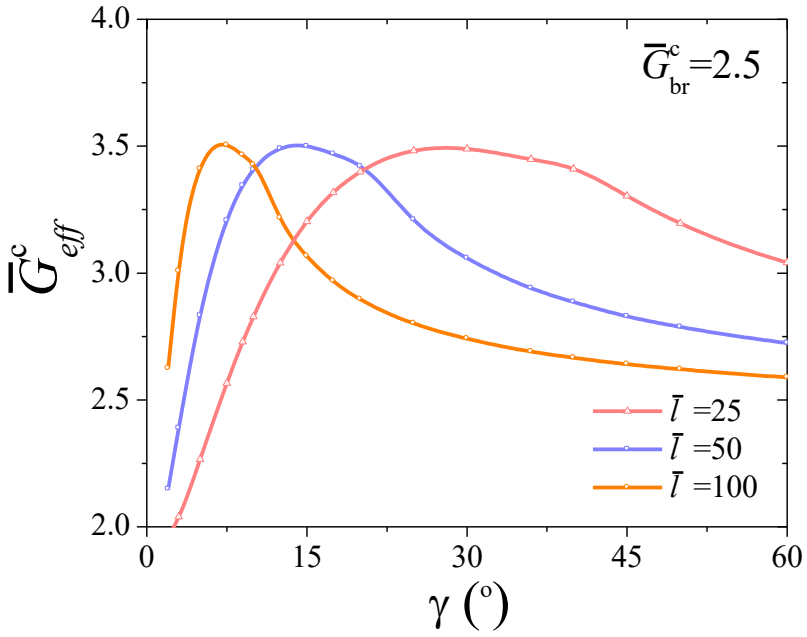

Figure 5.10: The effective fracture energy of oscillated/twisted plywood structure as a function of pitch angles. The effective fracture energy of the plywood structure as a function of the pitch angle with different dimensionless fiber lengths $\bar{l} = 25, 50, 100$ with a fixed fracture energy of crack bridging zone $\bar{G}^c_{br} = 2.5$.

The enhancement of fracture toughness in oscillated/twisted plywood structures is caused by the decrease of the local energy release rate and the enlargement of crack surface. Compared to the toughening mechanism of crack bridging only, the combination of crack bridging and crack tilting can dramatically enlarge the crack surface. As shown in Figure 5.7 and Figure 5.8, when the fracture energy of crack bridging is increased from $\bar{G}^c_{br} = 2.5$ to $\bar{G}^c_{br} = 5$, the area of the

twisted crack surface is increased, and consequently, the effective fracture toughness of the composite also increases. With the increase of the pitch angle, the area of the crack surface is decreased, but the local energy release rate is also decreased. Consequently, the competition between the shrinkage of the area of crack surface and the decrease of local energy release rate leads to an optimized pitch angle for the maximal effective fracture energy as shown in Figure 5.10. Similarly, with the increase of fiber length, the normalized area of the crack surface and local energy release rate decrease. Such competition results in an optimized fiber length for the maximal effective fracture energy as shown in Figure 5.9.

5.3 Conclusion

There has been mounting experimental evidence that both crack tilting and crack bridging could occur in the fiber-reinforced composites with twisted or oscillated plywood structure during its fracturing process. In this article, we develop a fracture mechanics model combining crack bridging and crack tilting to predict effective fracture toughness of the composite with plywood structure. In the model, we assume that whether crack tilting or crack bridging occurs during crack propagation is determined by the relative magnitude of the energy release rate for the two mechanisms. Our calculations further reveal that an optimized fiber length and pitch angle exist for achieving maximal fracture toughness of the composite, which agrees well with experimental observations.

Despite the uncovered insights into the fracturing process of the composite with twisted or oscillated plywood structure, the current model has several limitations and can be further improved in the future study. As shown in the model development, a large number of simplifying assumptions are adopted, among which we want to restate the most critical ones. First, we assume the fiber and matrix have identical elastic properties, which is usually not the case for most fiber-reinforced composites. Second, we ignore the possibility of crack branching during the crack growth, which may be in contrast to the fracturing process in some fiber-reinforced composite materials. Third, as shown in the Figure 5.3 and Figure 5.6, we assume the composite is a stack of laminates with embedded long fibers, which may be not true for many biological composites. Last, in the modelling of crack bridging, we assume the crack plane is perpendicular to the fiber direction, which is also an idealized scenario. These simplifying assumptions may result in inaccurate predictions of the fracture toughness of a composite with plywood structure. However, we do not see any intrinsic difficulties in developing more complex or realistic models with abandoning some or even all those assumptions mentioned above, which will be our research of interest for the next step.

Chapter 5, in full, is a reprint of the material as it appears in "Fracture Modes and Hybrid Toughening Mechanisms in Oscillated/Twisted Plywood Structure", *Acta biomaterialia* 91 (2019): 284-293, by Zhaoqiang Song, Yong Ni and Shengqiang Cai. The dissertation author was the primary investigator and first author of this paper.

Chapter 6 Conclusion

6.1 Summary of the dissertation

Vitrimers have emerged as a class of polymers combining great processability, self-healing capability and high-temperature mechanical properties. Most of these salient features of vitrimers originate from the existence of dynamic covalent bonds in the polymer network. We exploit the rate-dependent fracture properties of vitrimers which are originated from the bond exchanging exchange reaction. We find that the strong force-sensitivity of dynamic covalent bond leads to the rate-dependent fracture toughness and the rate-independent bulk dissipation. Moreover, we study the mechanical properties, especially the fracture toughness, of the polymer composites, i.e. vitrimers with hybrid networks and biocomposites. The strong and tough polymer composites are essential for the commercial applications. The toughening mechanism in polymer composites can guide the design of strong and tough polymers. The main results of each chapter are summarized as follows:

In Chapter 2, we describe the synthesis and characterizations of vitrimers with the hybrid networks. The vitrimers with the hybrid networks can be synthesized with a low molar ratio of dynamic covalent bonds (less than 20 mol%), which still maintains its reprocessing and self-healing capabilities. We develop a theoretical model to predict stress relaxation and creep of the vitrimers with hybrid networks at different temperatures and with different molar ratios between

the two monomers. The vitrimers with hybrid networks exhibit maximum fracture energy at a certain molar ratio.

In Chapter 3, we investigate the rate-dependent fracture of vitrimers, and we, for the first time, obtain the intrinsic fracture energy and bulk dissipation of vitrimers during crack extension. The intrinsic fracture energy strongly depends on tear speed, and such dependence can be well explained by Eyring theory. In contrast, the bulk dissipation only weakly depends on tear speed, which is drastically different from observations on traditional viscoelastic polymers.

In Chapter 4, we find that the transient nature of a vitrimer network yields peculiar fracture characteristics that cannot be understood from existing fracture theories. Crack propagation is a non-equilibrium process whose velocity depends on the interplay between external load, bond dynamics and network damage. To explain the transient life of a crack in the vitrimer, we extend the linear elastic fracture theory to a dynamic model that predicts the time-dependent evolution of a crack during loading.

In Chapter 5, we propose that a combination of crack tilting and crack bridging determines the effective fracture toughness of the fiber-reinforced composite with the plywood structure. Based on our quantitative analysis, it is found that the effective fracture toughness of the composite can be maximized for a certain pitch angle of the oscillated/twisted plywood structure, which agrees well with experiments.

6.2 Outlook for future work

A lot of challenges are still existed in the study of polymers and polymer composites. First, a more detailed study of bulk dissipation w_p in the tear test of a vitrimer film requires a full-field simulation of the tearing process with a nonlinear viscoelastic material model, which is a challenging task and has not been achieved in the literature yet. Second, a theoretical model is required to understand the toughening mechanism of the vitirmers with hybrid networks. Third, the complex fracture behaviors can exist in the fracture process of polymer composites, e.g., crack branching, et al., which are ignored in our study. Also, we assume the composite is a stack of laminates with embedded long fibers, which may be not true for many biological composites. Last, in the modelling of crack bridging, we assume the crack plane is perpendicular to the fiber direction, which is also an idealized scenario.

Bibliography

1. Podgórski, M., B.D. Fairbanks, B.E. Kirkpatrick, M. McBride, A. Martinez, A. Dobson, N.J. Bongiardina, and C.N. Bowman, *Toward Stimuli-Responsive Dynamic Thermosets through Continuous Development and Improvements in Covalent Adaptable Networks (CANs).* Advanced Materials, **32**(20): p. 1906876. 2020.

2. Wang, Z., H. Tian, Q. He, and S. Cai, *Reprogrammable, Reprocessible, and Self-Healable Liquid Crystal Elastomer with Exchangeable Disulfide Bonds.* ACS Applied Materials & Interfaces, **9**(38): p. 33119-33128. 2017.

3. Wang, Z., Q. He, Y. Wang, and S. Cai, *Programmable actuation of liquid crystal elastomers via "living" exchange reaction.* Soft matter, **15**(13): p. 2811-2816. 2019.

4. Wang, Y., Z. Wang, Q. He, P. Iyer, and S. Cai, *Electrically Controlled Soft Actuators with Multiple and Reprogrammable Actuation Modes.* Advanced Intelligent Systems, **2**(6): p. 1900177. 2020.

5. Song, Z. and S. Cai, *Cavitation dynamics in a vitrimer.* Acta Mechanica Sinica: p. 1. 2021.

6. Shen, T. and F.J. Vernerey, *Rate-dependent fracture of transient networks.* Journal of the Mechanics and Physics of Solids, **143**: p. 104028. 2020.

7. Chaudhury, M.K., *Rate-Dependent Fracture at Adhesive Interface.* The Journal of Physical Chemistry B, **103**(31): p. 6562-6566. 1999.

8. Williams, M., *Stress singularities resulting from various boundary conditions in angular corners of plates in extension.* Journal of applied mechanics, **19**(4): p. 526-528. 1952.

9. Geubelle, P.H. and W.G. Knauss, *Finite strains at the tip of a crack in a sheet of hyperelastic material: I. Homogeneous case.* Journal of Elasticity, **35**(1): p. 61-98. 1994.

10. Knauss, W.G., *A review of fracture in viscoelastic materials.* International Journal of Fracture, **196**(1-2): p. 99-146. 2015.

11. Schapery, R.A., *A theory of crack initiation and growth in viscoelastic media.* International Journal of Fracture, **11**(1): p. 141-159. 1975.

12. Schapery, R.A., *Correspondence principles and a generalizedJ integral for large deformation and fracture analysis of viscoelastic media.* International Journal of Fracture, **25**(3): p. 195-223. 1984.

13. de Gennes, P.G., *Soft Adhesives.* Langmuir, **12**(19): p. 4497-4500. 1996.

14. Hui, C.Y., Y.Y. Lin, and J.M. Baney, *The mechanics of tack: Viscoelastic contact on a rough surface.* Journal of Polymer Science Part B: Polymer Physics, **38**(11): p. 1485-1495. 2000.

15. Persson, B.N.J. and E.A. Brener, *Crack propagation in viscoelastic solids.* Physical Review E, **71**(3): p. 036123. 2005.

16. Nguyen, T. and S. Govindjee, *Numerical study of geometric constraint and cohesive parameters in steady-state viscoelastic crack growth.* International journal of fracture, **141**(1-2): p. 255-268. 2006.

17. Guo, J., A. Zhender, C. Creton, and C.-Y. Hui, *Time Dependent Fracture of Soft Materials: Linear versus Nonlinear Viscoelasticity.* Soft Matter, **16**: p. 6163-6179. 2020.

18. Barthelat, F. and H.D. Espinosa, *An Experimental Investigation of Deformation and Fracture of Nacre–Mother of Pearl.* Experimental Mechanics, **47**(3): p. 311-324. 2007.

19. Espinosa, H.D., A.L. Juster, F.J. Latourte, O.Y. Loh, D. Gregoire, and P.D. Zavattieri, *Tablet-level origin of toughening in abalone shells and translation to synthetic composite materials.* Nat Commun, **2**: p. 173. 2011.

20. Gao, H., B. Ji, I.L. Jager, E. Arzt, and P. Fratzl, *Materials become insensitive to flaws at nanoscale: lessons from nature.* Proc Natl Acad Sci U S A, **100**(10): p. 5597-5600. 2003.

21. Begley, M.R., N.R. Philips, B.G. Compton, D.V. Wilbrink, R.O. Ritchie, and M. Utz, *Micromechanical models to guide the development of synthetic 'brick and mortar' composites.* Journal of the Mechanics and Physics of Solids, **60**(8): p. 1545-1560. 2012.

22. Ni, Y., Z.Q. Song, H.Y. Jiang, S.H. Yu, and L.H. He, *Optimization design of strong and tough nacreous nanocomposites through tuning characteristic lengths.* Journal of the Mechanics and Physics of Solids, **81**: p. 41-57. 2015.

23. Song, Z.Q., Y. Ni, L.M. Peng, H.Y. Liang, and L.H. He, *Interface failure modes explain non-monotonic size-dependent mechanical properties in bioinspired nanolaminates.* Sci Rep, **6**: p. 23724. 2016.

24. Grunenfelder, L.K., N. Suksangpanya, C. Salinas, G. Milliron, N. Yaraghi, S. Herrera, K. Evans-Lutterodt, S.R. Nutt, P. Zavattieri, and D. Kisailus, *Bio-inspired impact-resistant composites.* Acta Biomater, **10**(9): p. 3997-4008. 2014.

25. Fischer, F.D., O. Kolednik, J. Predan, H. Razi, and P. Fratzl, *Crack driving force in twisted plywood structures.* Acta Biomaterialia, **55**: p. 349-359. 2017.

26. Yaraghi, N.A., N. Guarin-Zapata, L.K. Grunenfelder, E. Hintsala, S. Bhowmick, J.M. Hiller, M. Betts, E.L. Principe, J.Y. Jung, L. Sheppard, R. Wuhrer, J. McKittrick, P.D. Zavattieri, and D. Kisailus, *A Sinusoidally Architected Helicoidal Biocomposite.* Adv Mater, **28**(32): p. 6835-6844. 2016.

27. Suksangpanya, N., N.A. Yaraghi, D. Kisailus, and P. Zavattieri, *Twisting cracks in Bouligand structures.* J Mech Behav Biomed Mater, **76**: p. 38-57. 2017.

28. Suksangpanya, N., N.A. Yaraghi, R.B. Pipes, D. Kisailus, and P. Zavattieri, *Crack twisting and toughening strategies in Bouligand architectures.* International Journal of Solids and Structures, **150**: p. 83-106. 2018.

29. Song, Z., Y. Ni, and S. Cai, *Fracture modes and hybrid toughening mechanisms in oscillated/twisted plywood structure.* Acta Biomaterialia, **91**: p. 284-293. 2019.

30. Wu, K., Z. Song, S. Zhang, Y. Ni, S. Cai, X. Gong, L. He, and S.-H. Yu, *Discontinuous fibrous Bouligand architecture enabling formidable fracture resistance with crack orientation insensitivity.* Proceedings of the National Academy of Sciences, **117**(27): p. 15465-15472. 2020.

31. Capelot, M., M.M. Unterlass, F. Tournilhac, and L. Leibler, *Catalytic Control of the Vitrimer Glass Transition.* ACS Macro Letters, **1**(7): p. 789-792. 2012.

32. Röttger, M., T. Domenech, R. van der Weegen, A. Breuillac, R. Nicolaÿ, and L. Leibler, *High-performance vitrimers from commodity thermoplastics through dioxaborolane metathesis.* Science, **356**(6333): p. 62-65. 2017.

33. Callister Jr, W.D. and D.G. Rethwisch, *Fundamentals of materials science and engineering: an integrated approach*. 2012: John Wiley & Sons.

34. Capelot, M., D. Montarnal, F. Tournilhac, and L. Leibler, *Metal-Catalyzed Transesterification for Healing and Assembling of Thermosets.* Journal of the American Chemical Society, **134**(18): p. 7664-7667. 2012.

35. Denissen, W., M. Droesbeke, R. Nicolaÿ, L. Leibler, J.M. Winne, and F.E. Du Prez, *Chemical control of the viscoelastic properties of vinylogous urethane vitrimers.* Nature Communications, **8**(1): p. 14857. 2017.

36. Imato, K., M. Nishihara, T. Kanehara, Y. Amamoto, A. Takahara, and H. Otsuka, *Self-Healing of Chemical Gels Cross-Linked by Diarylbibenzofuranone-Based Trigger-Free Dynamic Covalent Bonds at Room Temperature.* Angewandte Chemie International Edition, **51**(5): p. 1138-1142. 2012.

37. Zhang, Z.P., M.Z. Rong, and M.Q. Zhang, *Polymer engineering based on reversible covalent chemistry: A promising innovative pathway towards new materials and new functionalities.* Progress in Polymer Science, **80**: p. 39-93. 2018.

38. Montarnal, D., M. Capelot, F. Tournilhac, and L. Leibler, *Silica-Like Malleable Materials from Permanent Organic Networks.* Science, **334**(6058): p. 965-968. 2011.

39. Ciaccia, M., R. Cacciapaglia, P. Mencarelli, L. Mandolini, and S. Di Stefano, *Fast transimination in organic solvents in the absence of proton and metal catalysts. A key to imine metathesis catalyzed by primary amines under mild conditions.* Chemical Science, **4**(5): p. 2253-2261. 2013.

40. Yan, P., W. Zhao, X. Fu, Z. Liu, W. Kong, C. Zhou, and J. Lei, *Multifunctional polyurethane-vitrimers completely based on transcarbamoylation of carbamates: Thermally-induced dual-shape memory effect and self-welding.* RSC Advances, **7**(43): p. 26858-26866. 2017.

41. Zheng, N., Z. Fang, W. Zou, Q. Zhao, and T. Xie, *Thermoset Shape-Memory Polyurethane with Intrinsic Plasticity Enabled by Transcarbamoylation.* Angewandte Chemie International Edition, **55**(38): p. 11421-11425. 2016.

42. Nishimura, Y., J. Chung, H. Muradyan, and Z. Guan, *Silyl Ether as a Robust and Thermally Stable Dynamic Covalent Motif for Malleable Polymer Design.* Journal of the American Chemical Society, **139**(42): p. 14881-14884. 2017.

43. Tanaka, F. and S. Edwards, *Viscoelastic properties of physically crosslinked networks. 1. Transient network theory.* Macromolecules, **25**(5): p. 1516-1523. 1992.

44. Long, R., H.J. Qi, and M.L. Dunn, *Modeling the mechanics of covalently adaptable polymer networks with temperature-dependent bond exchange reactions.* Soft Matter, **9**(15): p. 4083-4096. 2013.

45. Long, R., K. Mayumi, C. Creton, T. Narita, and C.-Y. Hui, *Time dependent behavior of a dual cross-link self-healing gel: Theory and experiments.* Macromolecules, **47**(20): p. 7243-7250. 2014.

46. Meng, F. and E.M. Terentjev, *Transient network at large deformations: Elastic–plastic transition and necking instability.* Polymers, **8**(4): p. 108. 2016.

47. Brighenti, R. and F.J. Vernerey, *A simple statistical approach to model the time-dependent response of polymers with reversible cross-links.* Composites Part B: Engineering, **115**: p. 257-265. 2017.

48. Vernerey, F.J., R. Long, and R. Brighenti, *A statistically-based continuum theory for polymers with transient networks.* Journal of the Mechanics and Physics of Solids, **107**: p. 1-20. 2017.

49. Parada, G.A. and X. Zhao, *Ideal reversible polymer networks.* Soft Matter, **14**(25): p. 5186-5196. 2018.

50. Meng, F. and E.M. Terentjev, *Fluidization of transient filament networks.* Macromolecules, **51**(12): p. 4660-4669. 2018.

51. Breuillac, A., A. Kassalias, and R. Nicolaÿ, *Polybutadiene Vitrimers Based on Dioxaborolane Chemistry and Dual Networks with Static and Dynamic Cross-links.* Macromolecules, **52**(18): p. 7102-7113. 2019.

52. Lessard, J.J., G.M. Scheutz, S.H. Sung, K.A. Lantz, T.H. Epps, and B.S. Sumerlin, *Block Copolymer Vitrimers.* Journal of the American Chemical Society, **142**(1): p. 283-289. 2020.

53. Li, L., X. Chen, K. Jin, and J.M. Torkelson, *Vitrimers Designed Both To Strongly Suppress Creep and To Recover Original Cross-Link Density after Reprocessing: Quantitative Theory and Experiments.* Macromolecules, **51**(15): p. 5537-5546. 2018.

54. Meng, F., M.O. Saed, and E.M. Terentjev, *Elasticity and Relaxation in Full and Partial Vitrimer Networks.* Macromolecules, **52**(19): p. 7423-7429. 2019.

55. Flory, P.J., *Molecular Size Distribution in Three Dimensional Polymers. I. Gelation1*. Journal of the American Chemical Society, **63**(11): p. 3083-3090. 1941.

56. Stockmayer, W.H., *Theory of Molecular Size Distribution and Gel Formation in Branched-Chain Polymers.* The Journal of Chemical Physics, **11**(2): p. 45-55. 1943.

57. Canadell, J., H. Goossens, and B. Klumperman, *Self-Healing Materials Based on Disulfide Links.* Macromolecules, **44**(8): p. 2536-2541. 2011.

58. Konuray, A.O., X. Fernández-Francos, and X. Ramis, *Analysis of the reaction mechanism of the thiol–epoxy addition initiated by nucleophilic tertiary amines.* Polymer chemistry, **8**(38): p. 5934-5947. 2017.

59. Ebewele, R.O., *Polymer science and technology*. 2000: CRC press.

60. Wang, S., S. Panyukov, M. Rubinstein, and S.L. Craig, *Quantitative Adjustment to the Molecular Energy Parameter in the Lake–Thomas Theory of Polymer Fracture Energy.* Macromolecules, **52**(7): p. 2772-2777. 2019.

61. de Luzuriaga, A.R., R. Martin, N. Markaide, A. Rekondo, G. Cabañero, J. Rodríguez, and I. Odriozola, *Epoxy resin with exchangeable disulfide crosslinks to obtain reprocessable, repairable and recyclable fiber-reinforced thermoset composites.* Materials Horizons, **3**(3): p. 241-247. 2016.

62. Zhou, F., Z. Guo, W. Wang, X. Lei, B. Zhang, H. Zhang, and Q. Zhang, *Preparation of self-healing, recyclable epoxy resins and low-electrical resistance composites based on double-disulfide bond exchange.* Composites Science and Technology, **167**: p. 79-85. 2018.

63. Fancey, K.S., *A mechanical model for creep, recovery and stress relaxation in polymeric materials.* Journal of materials science, **40**(18): p. 4827-4831. 2005.

64. Williams, G. and D.C. Watts, *Non-symmetrical dielectric relaxation behaviour arising from a simple empirical decay function.* Transactions of the Faraday society, **66**: p. 80-85. 1970.

65. Bai, R., B. Chen, J. Yang, and Z. Suo, *Tearing a hydrogel of complex rheology.* Journal of the Mechanics and Physics of Solids, **125**: p. 749-761. 2019.

66. Omonov, T., C. Harrats, P. Moldenaers, and G. Groeninckx, *Phase continuity detection and phase inversion phenomena in immiscible polypropylene/polystyrene blends with different viscosity ratios.* Polymer, **48**(20): p. 5917-5927. 2007.

67. Stamatoudis, M. and L. Tavlarides, *The effect of continuous-phase viscosity on the unsteady state behavior of liquid-liquid agitated dispersions.* The Chemical Engineering Journal, **35**(2): p. 137-143. 1987.

68. Kelly, P., *Solid mechanics part I: An introduction to solid mechanics.* Solid mechanics lecture notes: p. 241-324. 2013.

69. Faber, K.T. and A.G. Evans, *Crack deflection processes—I. Theory.* Acta Metallurgica, **31**(4): p. 565-576. 1983.

70. Angell, C.A., *Relaxation in liquids, polymers and plastic crystals — strong/fragile patterns and problems.* Journal of Non-Crystalline Solids, **131-133**: p. 13-31. 1991.

71. Long, R., C.-Y. Hui, J.P. Gong, and E. Bouchbinder, *The Fracture of Highly Deformable Soft Materials: A Tale of Two Length Scales.* Annual Review of Condensed Matter Physics, **12**(1): p. null. 2021.

72. Mayumi, K., J. Guo, T. Narita, C.Y. Hui, and C. Creton, *Fracture of dual crosslink gels with permanent and transient crosslinks.* Extreme Mechanics Letters, **6**: p. 52-59. 2016.

73. Song, Z., Z. Wang, and S. Cai, *Mechanics of vitrimer with hybrid networks.* Mechanics of Materials, **153**: p. 103687. 2021.

74. Wei, Y. and J.W. Hutchinson, *Interface strength, work of adhesion and plasticity in the peel test*, in *Recent Advances in Fracture Mechanics: Honoring Mel and Max Williams*, W.G. Knauss and R.A. Schapery, Editors. Springer Netherlands: Dordrecht. p. 315-333. 1998.

75. Tabuteau, H., S. Mora, M. Ciccotti, C.-Y. Hui, and C. Ligoure, *Propagation of a brittle fracture in a viscoelastic fluid.* Soft Matter, **7**(19): p. 9474-9483. 2011.

76. Liu, J., C. Yang, T. Yin, Z. Wang, S. Qu, and Z. Suo, *Polyacrylamide hydrogels. II. elastic dissipater.* Journal of the Mechanics and Physics of Solids, **133**: p. 103737. 2019.

77. Hui, C.-Y., T. Tang, Y.-Y. Lin, and M.K. Chaudhury, *Failure of Elastomeric Polymers Due to Rate Dependent Bond Rupture.* Langmuir, **20**(14): p. 6052-6064. 2004.

78. Lake, G.J., A.G. Thomas, and D. Tabor, *The strength of highly elastic materials.* Proceedings of the Royal Society of London. Series A. Mathematical and Physical Sciences, **300**(1460): p. 108-119. 1967.

79. Kauzmann, W. and H. Eyring, *The Viscous Flow of Large Molecules.* Journal of the American Chemical Society, **62**(11): p. 3113-3125. 1940.

80. Arruda, E.M. and M.C. Boyce, *A three-dimensional constitutive model for the large stretch behavior of rubber elastic materials.* Journal of the Mechanics and Physics of Solids, **41**(2): p. 389-412. 1993.

81. Ghatak, A., K. Vorvolakos, H. She, D.L. Malotky, and M.K. Chaudhury, *Interfacial Rate Processes in Adhesion and Friction.* The Journal of Physical Chemistry B, **104**(17): p. 4018-4030. 2000.

82. Griffith, A.A., *VI. The phenomena of rupture and flow in solids.* Philosophical transactions of the royal society of london. Series A, containing papers of a mathematical or physical character, **221**(582-593): p. 163-198. 1921.

83. Long, R. and C.-Y. Hui, *Crack tip fields in soft elastic solids subjected to large quasi-static deformation—a review.* Extreme Mechanics Letters, **4**: p. 131-155. 2015.

84. Zehnder, A.T., *Lecture notes on fracture mechanics*. 2007, Citeseer.

85. Mao, Y., B. Talamini, and L. Anand, *Rupture of polymers by chain scission.* Extreme Mechanics Letters, **13**: p. 17-24. 2017.

86. Talamini, B., Y. Mao, and L. Anand, *Progressive damage and rupture in polymers.* Journal of the Mechanics and Physics of Solids, **111**: p. 434-457. 2018.

87. Volokh, K., *Characteristic length of damage localization in rubber.* International Journal of Fracture, **168**(1): p. 113-116. 2011.

88. Rivlin, R. and A.G. Thomas, *Rupture of rubber. I. Characteristic energy for tearing.* Journal of polymer science, **10**(3): p. 291-318. 1953.

89. Wang, X. and W. Hong, *Delayed fracture in gels.* Soft Matter, **8**(31): p. 8171-8178. 2012.

90. Glassmaker, N., C. Hui, T. Yamaguchi, and C. Creton, *Detachment of stretched viscoelastic fibrils.* The European Physical Journal E, **25**(3): p. 253-266. 2008.

91. Saulnier, F., T. Ondarçuhu, A. Aradian, and E. Raphaël, *Adhesion between a viscoelastic material and a solid surface.* Macromolecules, **37**(3): p. 1067-1075. 2004.

92. Williams, J., *Energy release rates for the peeling of flexible membranes and the analysis of blister tests.* International Journal of Fracture, **87**(3): p. 265-288. 1997.

93. Long, R. and C.-Y. Hui, *Fracture toughness of hydrogels: measurement and interpretation.* Soft Matter, **12**(39): p. 8069-8086. 2016.

94. Bowman, C.N. and C.J. Kloxin, *Covalent Adaptable Networks: Reversible Bond Structures Incorporated in Polymer Networks.* Angewandte Chemie International Edition, **51**(18): p. 4272-4274. 2012.

95. Walter, J., J. Sehrt, J. Vrabec, and H. Hasse, *Molecular dynamics and experimental study of conformation change of poly (N-isopropylacrylamide) hydrogels in mixtures of water and methanol.* The Journal of Physical Chemistry B, **116**(17): p. 5251-5259. 2012.

96. Liu, M., J. Guo, C.-Y. Hui, and A. Zehnder, *Crack tip stress based kinetic fracture model of a PVA dual-crosslink hydrogel.* Extreme Mechanics Letters, **29**: p. 100457. 2019.

97. Ligoure, C. and S. Mora, *Fractures in complex fluids: The case of transient networks.* Rheologica Acta, **52**(2): p. 91-114. 2013.

98. Shabbir, A., Q. Huang, Q. Chen, R.H. Colby, N.J. Alvarez, and O. Hassager, *Brittle fracture in associative polymers: the case of ionomer melts.* Soft Matter, **12**(36): p. 7606-7612. 2016.

99. Huang, Q., N.J. Alvarez, A. Shabbir, and O. Hassager, *Multiple cracks propagate simultaneously in polymer liquids in tension.* Physical review letters, **117**(8): p. 087801. 2016.

100. Wang, Y. and S.-Q. Wang, *Rupture in rapid uniaxial extension of linear entangled melts.* Rheologica acta, **49**(11-12): p. 1179-1185. 2010.

101. Huang, Q., *Exploring the mechanism of fracture for entangled polymer liquids in extensional flow.* Physics of Fluids, **31**(8): p. 083105. 2019.

102. Pei, Z., Y. Yang, Q. Chen, Y. Wei, and Y. Ji, *Regional shape control of strategically assembled multishape memory vitrimers.* Advanced Materials, **28**(1): p. 156-160. 2016.

103. Krausz, A., *The theory of non-steady state fracture propagation rate.* International Journal of Fracture, **12**(2): p. 239-242. 1976.

104. Hansen, A.C. and J. Baker-Jarvis, *A rate dependent kinetic theory of fracture for polymers.* International Journal of Fracture, **44**(3): p. 221-231. 1990.

105. Qi, Y., Z. Zou, J. Xiao, and R. Long, *Mapping the nonlinear crack tip deformation field in soft elastomer with a particle tracking method.* Journal of the Mechanics and Physics of Solids, **125**: p. 326-346. 2019.

106. Vernerey, F.J., *Transient response of nonlinear polymer networks: A kinetic theory.* Journal of the Mechanics and Physics of Solids, **115**: p. 230-247. 2018.

107. Lalitha Sridhar, S. and F.J. Vernerey, *The chain distribution tensor: linking nonlinear rheology and chain anisotropy in transient polymers.* Polymers, **10**(8): p. 848. 2018.

108. Holzapfel, A.G., *Nonlinear solid mechanics II.* 2000.

109. Kothari, K., Y. Hu, S. Gupta, and A. Elbanna, *Mechanical response of two-dimensional polymer networks: role of topology, rate dependence, and damage accumulation.* Journal of Applied Mechanics, **85**(3). 2018.

110. Matsuda, T., R. Kawakami, T. Nakajima, and J.P. Gong, *Crack Tip Field of a Double-Network Gel: Visualization of Covalent Bond Scission through Mechanoradical Polymerization.* Macromolecules, **53**(20): p. 8787-8795. 2020.

111. Yuk, H. and X. Zhao, *A new 3D printing strategy by harnessing deformation, instability, and fracture of viscoelastic inks.* Advanced Materials, **30**(6): p. 1704028. 2018.

112. Yamaguchi, T., C. Creton, and M. Doi, *Simple model on debonding of soft adhesives.* Soft matter, **14**(30): p. 6206-6213. 2018.

113. Deplace, F., C. Carelli, S. Mariot, H. Retsos, A. Chateauminois, K. Ouzineb, and C. Creton, *Fine tuning the adhesive properties of a soft nanostructured adhesive with rheological measurements.* The Journal of Adhesion, **85**(1): p. 18-54. 2009.

114. Creton, C. and M. Ciccotti, *Fracture and adhesion of soft materials: a review.* Reports on Progress in Physics, **79**(4): p. 046601. 2016.

115. Luo, F., T.L. Sun, T. Nakajima, T. Kurokawa, Y. Zhao, A.B. Ihsan, H.L. Guo, X.F. Li, and J.P. Gong, *Crack blunting and advancing behaviors of tough and self-healing polyampholyte hydrogel.* Macromolecules, **47**(17): p. 6037-6046. 2014.

116. Kim, B.S. and D.J. Mooney, *Engineering smooth muscle tissue with a predefined structure.* Journal of Biomedical Materials Research: An Official Journal of The Society for Biomaterials, The Japanese Society for Biomaterials, and the Australian Society for Biomaterials, **41**(2): p. 322-332. 1998.

117. Kim, J., S.S. Kim, K.H. Kim, Y.H. Jin, S.M. Hong, S. San Hwang, B.-G. Cho, D.Y. Shin, and S.S. Im, *Applications of telechelic polymers as compatibilizers and stabilizers in polymer blends and inorganic/organic nanohybrids.* Polymer, **45**(10): p. 3527-3533. 2004.

118. Callister, W.D. and D.G. Rethwisch, *Materials science and engineering*. Vol. 5. 2011: John Wiley & Sons NY.

119. Ifuku, S., M. Nogi, K. Abe, M. Yoshioka, M. Morimoto, H. Saimoto, and H. Yano, *Preparation of chitin nanofibers with a uniform width as alpha-chitin from crab shells.* Biomacromolecules, **10**(6): p. 1584-1588. 2009.

120. Yang, Y., Z. Chen, X. Song, Z. Zhang, J. Zhang, K.K. Shung, Q. Zhou, and Y. Chen, *Biomimetic Anisotropic Reinforcement Architectures by Electrically Assisted Nanocomposite 3D Printing.* Adv Mater, **29**(11): p. 1605750. 2017.

121. Weiner, S. and H.D. Wagner, *THE MATERIAL BONE: Structure-Mechanical Function Relations.* Annual Review of Materials Science, **28**(1): p. 271-298. 1998.

122. Yang, R., A. Zaheri, W. Gao, C. Hayashi, and H.D. Espinosa, *AFM Identification of Beetle Exocuticle: Bouligand Structure and Nanofiber Anisotropic Elastic Properties.* Advanced Functional Materials, **27**(6): p. 1603993. 2017.

123. Weaver, J.C., G.W. Milliron, A. Miserez, K. Evans-Lutterodt, S. Herrera, I. Gallana, W.J. Mershon, B. Swanson, P. Zavattieri, E. DiMasi, and D. Kisailus, *The stomatopod dactyl club: a formidable damage-tolerant biological hammer.* Science, **336**(6086): p. 1275-1280. 2012.

124. Zaheri, A., J.S. Fenner, B.P. Russell, D. Restrepo, M. Daly, D. Wang, C. Hayashi, M.A. Meyers, P.D. Zavattieri, and H.D. Espinosa, *Revealing the Mechanics of Helicoidal Composites through Additive Manufacturing and Beetle Developmental Stage Analysis.* Advanced Functional Materials, **28**(33): p. 1803073. 2018.

125. Carrère, N., E. Martin, and J. Lamon, *The influence of the interphase and associated interfaces on the deflection of matrix cracks in ceramic matrix composites.* Composites Part A: Applied Science and Manufacturing, **31**(11): p. 1179-1190. 2000.

126. Natarajan, B., A. Krishnamurthy, X. Qin, C.D. Emiroglu, A. Forster, E.J. Foster, C. Weder, D.M. Fox, S. Keten, J. Obrzut, and J.W. Gilman, *Binary Cellulose Nanocrystal Blends for Bioinspired Damage Tolerant Photonic Films.* Advanced Functional Materials, **28**(26): p. 1800032. 2018.

127. Chen, S.-M., H.-L. Gao, Y.-B. Zhu, H.-B. Yao, L.-B. Mao, Q.-Y. Song, J. Xia, Z. Pan, Z. He, H.-A. Wu, and S.-H. Yu, *Biomimetic twisted plywood structural materials.* National Science Review, **5**(5): p. 703-714. 2018.

128. Cotterell, B. and J.R. Rice, *Slightly Curved or Kinked Cracks.* International Journal of Fracture, **16**(2): p. 155-169. 1980.

129. Chang, J., J.Q. Xu, and Y. Mutoh, *A general mixed-mode brittle fracture criterion for cracked materials.* Engineering Fracture Mechanics, **73**(9): p. 1249-1263. 2006.

130. Sachs, C., H. Fabritius, and D. Raabe, *Experimental investigation of the elastic–plastic deformation of mineralized lobster cuticle by digital image correlation.* Journal of structural biology, **155**(3): p. 409-425. 2006.

131. Sykes, D., R. Hartwell, R.S. Bradley, T.L. Burnett, B. Hornberger, R.J. Garwood, and P.J. Withers, *Time-lapse three-dimensional imaging of crack propagation in beetle cuticle.* Acta biomaterialia, **86**: p. 109-116. 2019.

132. Quan, H., W. Yang, E. Schaible, R.O. Ritchie, and M.A. Meyers, *Novel defense mechanisms in the armor of the scales of the "living fossil" coelacanth fish.* Advanced Functional Materials, **28**(46): p. 1804237. 2018.

133. Shao, Y., H.P. Zhao, X.Q. Feng, and H.J. Gao, *Discontinuous crack-bridging model for fracture toughness analysis of nacre.* Journal of the Mechanics and Physics of Solids, **60**(8): p. 1400-1419. 2012.

134. Shao, Y., H.P. Zhao, and X.Q. Feng, *Optimal characteristic nanosizes of mineral bridges in mollusk nacre.* Rsc Advances, **4**(61): p. 32451-32456. 2014.

135. Budiansky, B. and J.C. Amazigo, *Toughening by Aligned, Frictionally Constrained Fibers.* Journal of the Mechanics and Physics of Solids, **37**(1): p. 93-109. 1989.

136. Broberg, K.B., *Cracks and fracture*. 1999: Elsevier.

137. Meng, Q., B. Li, T. Li, and X.-Q. Feng, *A multiscale crack-bridging model of cellulose nanopaper.* Journal of the Mechanics and Physics of Solids, **103**: p. 22-39. 2017.

138. Mushi, N.E., *Chitin nanofibers, networks and composites: Preparation, structure and mechanical properties*. 2014, KTH Royal Institute of Technology.

139. Ezekiel Mushi, N., N. Butchosa, Q. Zhou, and L.A. Berglund, *Nanopaper membranes from chitin-protein composite nanofibers-structure and mechanical properties.* Journal of Applied Polymer Science, **131**(7): p. 10421. 2014.

140. Saito, T., R. Kuramae, J. Wohlert, L.A. Berglund, and A. Isogai, *An ultrastrong nanofibrillar biomaterial: the strength of single cellulose nanofibrils revealed via sonication-induced fragmentation.* Biomacromolecules, **14**(1): p. 248-253. 2013.

141. Song, J.W., C.J. Chen, S.Z. Zhu, M.W. Zhu, J.Q. Dai, U. Ray, Y.J. Li, Y.D. Kuang, Y.F. Li, N. Quispe, Y.G. Yao, A. Gong, U.H. Leiste, H.A. Bruck, J.Y. Zhu, A. Vellore, H. Li, M.L. Minus, Z. Jia, A. Martini, T. Li, and L.B. Hu, *Processing bulk natural wood into a high-performance structural material.* Nature, **554**(7691): p. 224-228. 2018.